Ordered Arrays of Nanocrystals: Synthesis, Properties and Applications

by

Sreekar Bhaviripudi

B.Tech., Materials Science and Metallurgical Engineering
Indian Institute of Technology Bombay, 2002

Submitted to the Department of Materials Science and Engineering
in partial fulfillment of the requirements for the degree of

Doctor of Philosophy in Materials Science and Engineering

at the

MASSACHUSETTS INSTITUTE OF TECHNOLOGY

September 2007

Author . . . .
Department of Materials Science and Engineering
August 8, 2007

Certified by . . . .
Angela M. Belcher
Germehaussen Professor of Materials Science and Engineering
and Biological Engineering
Thesis Supervisor

Accepted by . . . .
Samuel M. Allen
POSCO Professor of Physical Metallurgy
Chair, Departmental Committee on Graduate Students

Ordered Arrays of Nanocrystals: Synthesis, Properties and Applications

by

Sreekar Bhaviripudi

Submitted to the Department of Materials Science and Engineering
on August 8, 2007 in Partial Fulfillment of the Requirements for the
Degree of Doctor of Philosophy in Materials Science and Engineering

ABSTRACT

Nanoscale materials, including nanocrystals and carbon nanotubes, exhibit an appealing array of physical properties, and provide an interesting prospect for research both from a fundamental as well as a technological perspective. The current emerging themes in nanoscale research are: controlled synthesis with well defined sizes and geometries; unraveling their fundamental physical properties; and assembly of these nanoscale building blocks into functional devices. Although several approaches for producing the nanoparticles have been reported in the past decade, a general, large scale method for controlled synthesis of well-defined nanoparticles in the 1-5 nm size regimes is yet to be found. A general method that enables both syntheses of nanoparticles and their assembly on substrates is critical towards furthering technological applications.

The work described here involved developing a method that utilized principles of self-assembly in conjunction with inorganic and organic synthetic chemistry for the controlled synthesis of ordered arrays of nanocrystals. A unique attribute of this technique is it combined themes one and three, aforementioned, into a single step. First, uniform arrays of various mono- and hetero-bi-metallic nanoparticles with sizes in the range of 1-5 nm were synthesized on various substrates using PS-P4VP block copolymer (BCP) templates. These arrays of monodisperse nanoparticles were employed as catalysts for the diameter-controlled growth of SWNTs. Comparisons on their catalytic activities provided valuable insight on the catalyst-assisted growth of SWNTs. Alternate ways to improve the catalytic yield of nanotubes employing bi-metallic nanoparticles as well as novel catalysts for nanotube growth are also being reported for the first time. Importantly, a combinatorial approach involving BCPs and gas phase reactions was designed that enabled us in addressing some of the long standing problems associated with the syntheses of semiconductor III-Nitride nanocrystals. Finally, versatility of this synthesis method was further demonstrated by syntheses of ternary nitrides as well as rare earth ions doped GaN. While the investigations on the latter aspects are still in there infancy, initial results show significant promise and pave an exciting prospect for future studies.

Thesis Advisor: Angela M. Belcher

Title: Germehaussen Professor of Materials Science and Engineering and Biological Engineering

Acknowledgements

No words can express my boundless gratitude to my immediate family for their unfaltering support, guidance and enduring love. Without their efforts I would have not been able to pursue my PhD. I dedicate this thesis to my family.

I express my appreciation of the general guidance and advice I received from my undergraduate advisor and mentor, Prof. T. R. S. Prasanna, during my scientific career. Merely watching his mind in action was not only an incredible learning experience but also an inspiring one. Unfortunately, I will regret for the rest of my life for probably disappointing him by opting away from a career in science.

At MIT, I am profoundly grateful to my advisor, Angie Belcher, for providing the intellectual freedom to pursue my research ideas as well as for her kindness. I had all her immense technical wealth and experience to draw upon, and the only limitation was my own capacity to profit from it.

I thank my thesis committee members, Caroline A. Ross and Jing Kong, for assistance with my thesis preparation and defense. A part of this work also involved extensive collaboration with Jing Kong, and I am grateful to her, for her enthusiasm with my work as well as for her guidance.

I have also greatly benefited from my discussions with Evelyn L. Hu (UCSB). Her valuable comments and suggestions on III-nitride related work are greatly appreciated.

I thank both my current and past colleagues in the BioMolecular Materials Group, especially Amy S, Ahmad K, Andrew M, Asher S, Beau P, Chung-Yi C, David G, Debadyuti G, Desiree S, Eric K, Georg F, Julie N, Jennifer H, Kitae N, Katherine R, Michelle B, Roberto B, Saeeda J, Steve K, Youjin L and Dr. Yun, for providing a stimulating working environment filled with fun. Special thanks to Jifa Qi for providing experimental guidance, and, in particular, for his constructively

critical comments on all my manuscripts. *Komawoyo* to Soo-Kwan Lee for his camaraderie as well as for sharing his wisdom. I also owe much to Christine Flynn for reading and commenting on large parts of my thesis draft.

I thank members of the NME lab for providing unrestricted access to their experimental lab resources. *Muchas gracias* to Alfonso Reina for his help with my initial nanotube growth experiments as well as for commenting on parts of my thesis draft. Thanks to members of the Fitzgerald group, including Mayank Bulsara and Bai Yu, for providing access to their TEM sample preparation facility and the resources within.

Though I am thankful to the support staff at CMSE and MTL, I like to mention especially, Mike Frongillo (CMSE), Elizabeth Shaw (CMSE) and Kurt Broderick (MTL) for training and instrumentation support.

Early part of this work was supported by John F. Eliot Fellowship, this funding is gratefully acknowledged. Funding from MARCO-FENA, DARPA and other resources are also greatly appreciated.

I have accumulated personal debts on my way to MIT as well as while pursuing my doctoral degree. I can't thank my long-time friends at MIT and elsewhere enough for their camaraderie and fellowship- a partial list of friends at MIT includes Ajay Deshpande, Amit Deshpande, Ajay Selot, Amit Surana, Anastasios J. Hart, Bhanu Mahanti, Harish Mukandan, Hemant Sahoo, Hemanth Prakash, Jay-kumar Sunadararajan, Phani Ramakrishna, Pranava Goudavan, Rishi Sharma, Sivaram Cheekiralla, Taras Gorishnny, Vikram Sivakumar, Vikrant Agnihotri, Vinay Mahajan and Vijay Shilpiekandula as well as long-time buddies, including Kranthi Kumar Reddy, Lalit Kumar, Prakash Sista, Praveen Durga, Shashibhushan Borade and Vaibhav Shah. I wish them all the very best for their future endeavors.

Contents

ABSTRACT

Acknowledgments

List of Tables

List of Figures

List of Abbreviations and Acronyms

PART ONE
MOTIVATION & INTRODUCTION

Chapter 1 Introduction

Chapter 2 Self-Organization and Block Copolymer Templates

Abstract

PART TWO
ORDERED ARRAYS OF NANOPARTICLES: SYNTHESIS, CHARACTERIZATION & PROPERTIES

Chapter 3 Monodisperse Arrays of Mono- and bi-Metallic Nanocrystals Arrays

Abstract

Chapter 6 Electrochemical Synthesis of Metal Nanocrystals

Abstract

Appendices

List of Tables

List of Figures

List of Abbreviations and Acronyms

[**AFM**]	Atomic Force Microscopy
[**BCC**]	Body-Centered Cubic
[**BCP**]	Block Co-Polymer
[**CNT**]	Carbon Nanotube
[**CVD**]	Chemical Vapor Deposition
[**D-band**]	Disorder induced Raman mode
[**FCC**]	Face-Centered Cubic
[**FFT**]	Fast Fourier Transform
[**FTIR**]	Fourier Transform Infrared Spectroscopy
[**HCP**]	Hexagonal Close Packing
[**MOCVD**]	Metallo-Organic Chemical Vapor Deposition
[**MWNT**]	Multi-wall Nanotube
[**NC**]	Nanocrystals
[**NP**]	Nanoparticle
[**NSOM**]	Near-field Scanning Optical Microscopy
[**PL**]	Photoluminescence
[**PS-P4VP**]	Polystyrene-Poly4vinylpyridine
[**P4VP**]	Poly4vinylpyridine
[**RBM**]	Radial Breathing Mode
[**SEM**]	Scanning Electron Microscopy
[**SNC**]	Semiconductor Nanocrystal
[**SWNT**]	Single-wall Nanotube
[**TEM**]	Transmission Electron Microscopy; P- Plan View; X- Cross-sectional
[**XPS**]	X-ray Photoelectron Spectroscopy
[**XRD**]	X-Ray Diffraction

Chapter 1

Introduction

"…there's plenty of room at the bottom…" *Richard Feynman*

The renaissance in materials science in the past decade has been primarily led by the research in nanoscale materials. Nanomaterials$_{[1]}$ refer to a realm of matter with dimensions in the nanoscale (~1-100 nm), which are intermediate between atoms/molecules and condensed matter. To date, the research in nanoscale materials has been multi-disciplinary, encompassing the traditional fields of materials science, condensed matter physics, chemistry and biology. Size dependency of physical and chemical properties of nanomaterials created an initial interest to unravel and to understand the underlying basic science associated with these nanoscale materials. In addition, an ever demanding need for miniaturization of electronic devices and molecular diagnostics have further spurred the interest in nanoscale materials research.

The important emerging themes in nanoscale materials research are:

---

[1] Nanoscale materials, nanomaterials and nanostructures are used here with the same meaning.

0-D nanoscale materials, nanoparticles, nanocrystals and quantum dots are also used interchangeably with the same meaning. Some nanoparticles may be amorphous, and should be treated differently from nanocrystals, such instances are clearly emphasized where and when applicable.

[1] Controlled synthesis of nanoscale materials with well defined size and geometry;

[2] Unraveling the fundamental material properties (both physical and chemical) of nanoscale materials; and

[3] Assembly and hierarchical integration of these nanoscale building blocks into functional devices in a reproducible manner to serve wide variety of technological applications.

In addition to chemistry, biology is playing an integral role in addressing some of these important themes. The interface between materials science and biology has gained tremendous focus in the recent past. One of the primary reasons is that the nanomaterials and the basic building blocks of biology, such as DNA, RNA, proteins, etc., have similar dimensions. At one end of the interface, using a bottom-up approach by bio-mimicking nature, the biological building blocks are either being used as templates or the biomineralization process is being applied to synthesize inorganic nanoscale materials in a controlled manner, which has otherwise been difficult due to the physical limits imposed by the traditional top-down methods, such as photo- and electron- beam lithography. Research to this end is fast emerging and considerable efforts are being currently focused to address the issue. At the other end of the interface, the remarkable material properties and the high surface area/volume ratio of the nanoscale materials are being exploited to either detect or sense biological units such as DNA, proteins, nucleic acids, etc. Research in this area has been largely fueled by the need for highly selective and highly sensitive detection agents that could overcome the drawbacks of conventional diagnostics. Nanomaterials, including 0-D materials such as metal and semiconductor nanoparticles and 1-D materials such as inorganic semiconducting nanowires as well as carbon nanotubes, are promising candidates for their use in biosensing and delivery agents, in addition to a plethora of other technological applications, including FETs, FEDs, etc.

The Biomolecular Materials Group focuses at the first interface and pioneers in the bioengineered phage display technique and lays emphasis on understanding the molecular nature of organic-inorganic interfaces and the concepts of biomineralization with the ultimate aim of using these principles to fabricate nanoscale opto-electronic devices. Results demonstrating fabrication of components for devices using viral templates (for example - cathode materials for Li-rechargeable batteries[2]) have already been reported and many more interesting ideas are currently being explored as well. As far as the syntheses of nanoscale materials is concerned in this thesis, the work described herein involved working at the second interface and utilized principles of self-assembly in conjunction with inorganic and organic synthetic chemistry for the controlled syntheses of inorganic nanoscale materials. These studies hope to compliment the efforts of the rest of the group towards understanding nanoscale materials and towards furthering technological applications.

1.2 Scope of the thesis

The work described herein addresses the following three themes in nanoscale research with emphasis on 0-D nanoscale materials, including transition metal nanoparticles and III-nitride nanocrystals, as well as 1-D nanoscale materials including SWNTs, MWNTs and Si nanowires:

[1] Controlled syntheses of 0-D and 1-D nanoscale materials;

[2] Examinations on their fundamental physical properties of nanoparticles, such as the bandgap;

[3] Hierarchical integration of these nanostructures for device fabrication. While devices have not been fabricated to date, as will be seen later, a solid foundation for achieving these structures has been set!

One of the highlights in this work involved combining themes one and three into one single step, which otherwise, have traditionally been dealt separately. Motivations for investigating the specific

---

[2] Kitae Nam, MIT Ph.D. Thesis

types of nanoscale materials mentioned above are provided at the beginning of chapters 3-5. The following is the schematic of the contents of this thesis work.

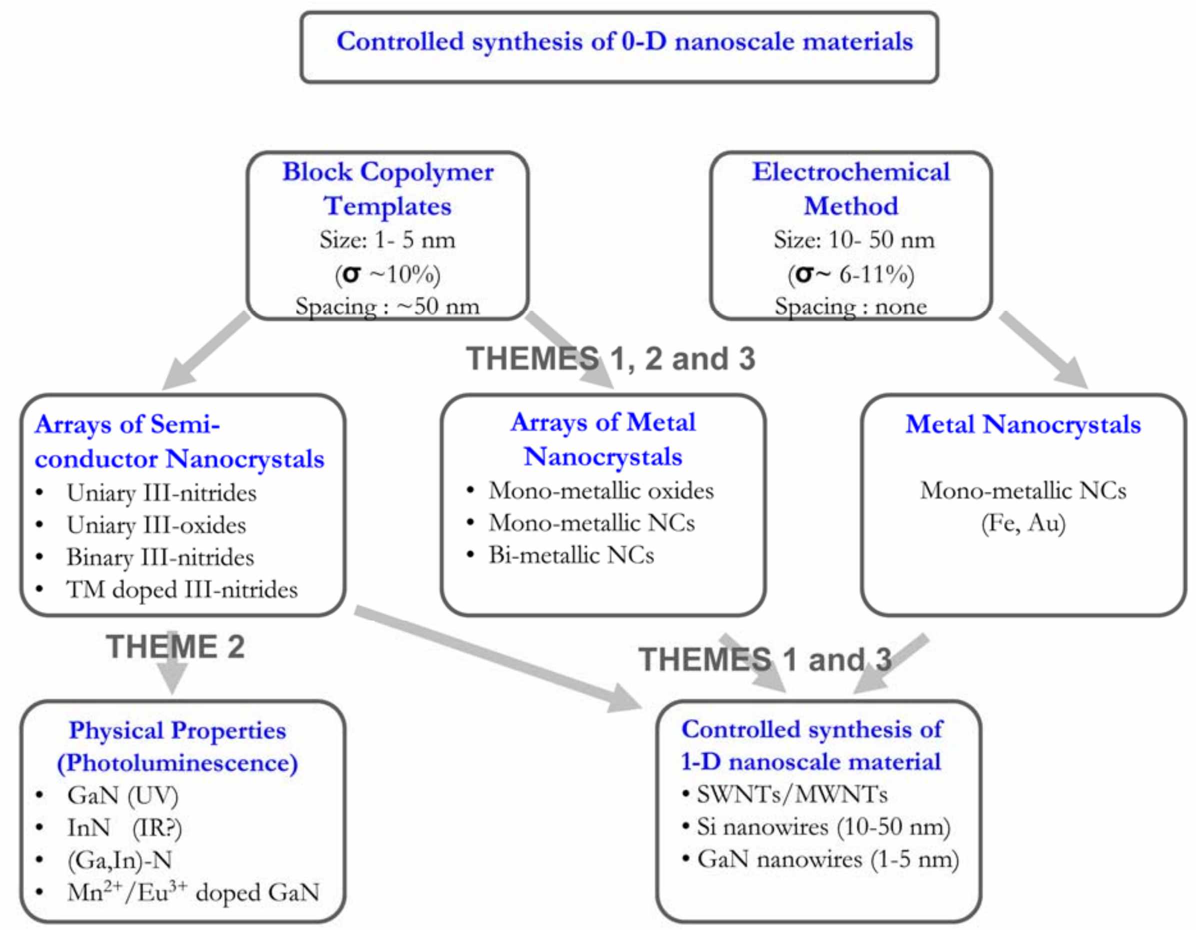

Figure 1.1 Schematic showing the scope of the thesis.

1.3 Organization of the thesis

The thesis is divided into three parts:

[1] Motivation and Introduction (Chapters 1 & 2)

[2] Ordered arrays of nanoparticles: Synthesis, Characterization & Properties (Chapters 3 & 4)

[3] Ordered arrays of nanoparticles: Applications (chapter 5)

Part 1 gives motivation for this work as well as introduces to the basic principles of self-organizing structures. **Part 2** focuses on controlled synthesis of mono- and bi-metallic nanoparticles as well as III-nitride semiconductor nanocrystals utilizing self-organized structures as templates and **part 3** discusses applications of ordered arrays of nanoparticles, in particular, their catalytic properties of metal nanoparticles for the growth of 1-D nanostructures.

Chapter 1 provides brief introduction as well as initial motivation for this work, which is then followed by an outline for the scope and organization of the thesis.

Main thrust of **chapter 2** introduces principles and molecular pre-requisites for self-assembly. It then provides an overview on block copolymers (BCPs) and the various self-organized structures they form, in particular, spherical micelles that form from their dilute solutions. Basic parameters that affect the size of micelles are then discussed. Some of these will be elaborated and will also be examined in more detail in chapters 3 and 4.

Chapter 3 focuses on the syntheses and characterization of uniform arrays of mono- and bi-metallic nanoparticles. Experiments exploring the effect of templating parameters on nanoparticles sizes and periodicity are then illustrated. The results described in this chapter also lay a ground work for most of the experiments that are reported in the subsequent chapters, in particular, for chapter 5. This chapter concludes with suggested directions for future work that include fabrication of linear arrays of nanoparticles as well as novel strategies for single molecule detection based on those arrays.

Chapter 4 introduces III-nitrides nanocrystals, current state of research and present challenges related to their synthesis as well as challenges associated towards understanding their fundamental physical properties. Results demonstrating the versatility of the BCP method that enable syntheses of III-nitride semiconductor nanocrystals, involving a two step approach are then presented. The underlying physics of the photoluminescence (PL) data from nanocrystals along with a brief description of the various factors that affect the PL spectrum are also discussed. Finally, versatility of this synthesis method is further demonstrated by (1) syntheses of binary compounds of (Ga, In) nitrides and (2) doping GaN with Eu^{3+} and Mn^{2+} ions. While the studies on the later two aspects are still in their infancy, initial results show significant promise and pave an exciting prospect for future studies. Note: This chapter has been written in a format that should enable one to read it with referring to the previous chapters.

Chapter 5 introduces current challenges as well as the present state of research with regard to synthesis of SWNTs. A methodology to address these challenges is provided and the logic behind this approach is explained further. Additionally, this chapter further explores the interesting experiments on the catalytic activity of various mono-metallic nanoparticles. Novel methods for improving the catalytic yield of nanotubes, which had significant success, are also discussed. New catalysts for the growth of SWNTs, including Au nanoparticles that might eventually lower the synthesis temperature are also presented. Finally, controlled syntheses of nanotubes in various configurations for device fabrication are discussed.

Chapter 6 describes an alternate, yet simple room temperature method for syntheses of transition metal nanocrystals on low energy substrates, such as Si (100) based on the electrochemical method that addresses some of the issues discussed in earlier chapters with regard to controlled syntheses of nanoscale materials. Examinations and discussions in this chapter focus on Au nanocrystals and catalyst-assisted vapor-liquid-solid growth of Si nanowires. Investigations revealing the equilibrium shapes of Au nanocrystals on Si substrates are then discussed. A theory that was formulated to predict the shapes of the nanocrystals synthesized on low surface energy substrates, and the parameters that influence them are elucidated.

Suggested directions for future work related to metal nanoparticles are presented in **Chapter 7**

Chapter 2

Self-Organization and Block Copolymer Templates

Abstract

Self-organization, as the name suggests, is the autonomous organization of individual motifs into well-defined structures. To-date, self-assembly has played a crucial role in the manipulation as well as the synthesis of nanoscale materials and future prospects in this field are promising due to steady and progressive developments in the associated synthesis and processing techniques. In this chapter, **first**, a brief introduction to self assembly, its principles and molecular pre-requisites are discussed. **Second**, block copolymers that self-organize into well-ordered structures with various geometries are introduced. **Finally**, principles of self-assembly are explained with an example involving dilute solutions of block copolymers in solvents that form spherical micelles and parameters that affect the size of these micelles are then explained.

2.1 Introduction

Research in inorganic nanoscale materials has been rapidly evolving over the past decade and has been motivated primarily both from fundamental as well as technological perspectives. Moreover, it has been spurred by the ever demanding need for miniaturization of electronic devices as well as molecular diagnostics. As mentioned previously, the current three emerging themes in nanoscale research are- controlled synthesis, unraveling their fundamental properties and hierarchical integration of nanoscale building blocks to further technological applications. As far as synthesis is concerned, most traditional top-down approaches, including photo-lithography, e-beam evaporation, etc., have not enabled controlled synthesis of inorganic nanoscale materials (~1-20 nm), in part due to the physical limitations imposed by these techniques. Thus, alternate approaches for controlled syntheses of nanoscale materials entailed and are critical to conduct further research. Bottom-up approaches (assembling atom by atom to synthesize materials in nanoscale dimensions) incorporating the principles of self-organization and self-assembly provide a possible exciting route for the controlled synthesis of inorganic nanoscale materials. To this end, both biomineralization and macromolecules (polymers) with their unique ability to self-organize provide an interesting template for their synthesis.

2.2 Self-Organization/ Self-assembly: Principles and Molecular pre-requisites

As the name suggests, self-organization or self-assembly, is the process in which an organization or the assembly into ordered structures takes place through either physical or chemical processes or is assisted by biomolecules to promote molecular selectivity and specificity. Self-organization is defined differently, albeit slightly, in various scientific disciplines, and yet all these definitions share the fact that in the course of self-organization, a system produces properties that it did not possess before (for instance, order). It is important to briefly mention these definitions (adopted from references [1-3])

Chemistry: Self-organization- well-defined structures that result spontaneously from the components of the system by non-covalent forces (self-assembly), for examples in the case of liquid crystals, micelles, etc.

Biology: Self-organization- a spontaneous build-up of complex structures which takes place under adequate environmental conditions solely on the basis of the respective molecular property, namely, without the effect of external factors. For example, protein folding, formations of lipid double layers.

Physics: Self-Organization- spontaneous formation of three-dimensional and temporal structures in complex systems which results from the cooperative effect of partial systems. For example, ferromagnetism, superconductivity.

Molecular pre-requisites for self-assembly

There are number of pathways that drive self-organization. To build ordered structures it is indispensable that both long range repulsive and short range attractive forces co-exist in the system. Attractive interactions can be covalent bonds, local conservation of charge neutrality (ionic bonds) and repulsive interactions, include hydrophilic interactions, hydrophobic interaction, incompatible polymers. For instance, a pair of forces that drive self-assembly, includes hydrophilic/hydrophobic (long range repulsion) and covalent binding (short range attractive), see schematic in fig 2.1. There are long-range repulsive forces between motifs, A and B. The presence of short range attractive interactions holds the motifs together. With constraints of maximizing pairing between A and B, while minimizing the contacts between A and B leads to a configuration shown in the schematic (fig. 2.1), which illustrates the principle of self-assembly based on attractive-repulsive pairs of forces.

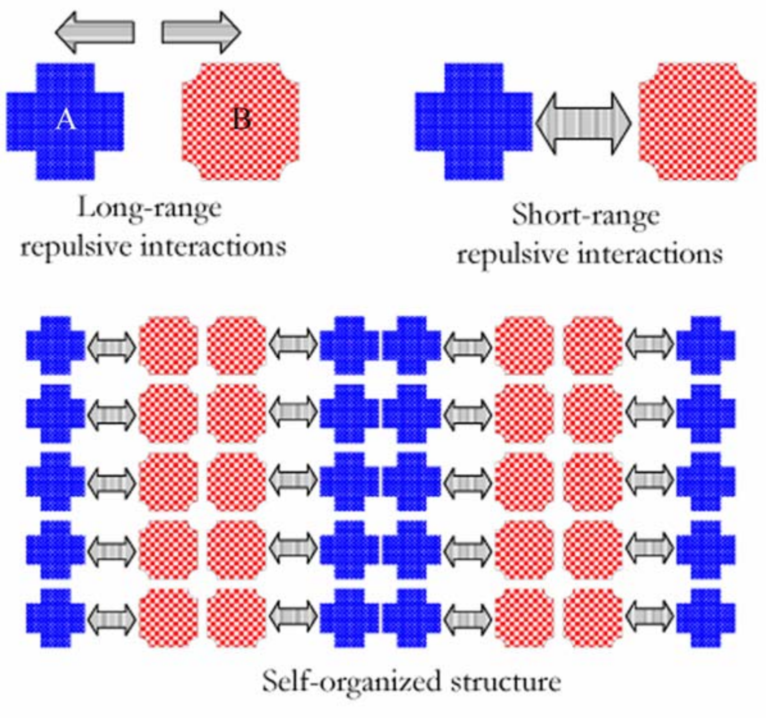

Figure 2.1: Illustration displaying long-range repulsive and short-range attractive forces leading to self-organized structure.

In the following section, self-organization with regard to amphiphilic block copolymers (BCP), in particular, with their dilute solutions that form micelles will be elucidated. Concentrated solutions of BCPs, such as lyotropic phases and bulk phases, also self organize, however, these will not be discussed here in detail.

2.3 Templates: Amphiphilic Block copolymers

Macromolecules are well suited as templates for syntheses of micro- and nanoscale materials as they offer control over the size and topology of the template over a wider length scale (1 nm - 100 μm). The simplest macromolecule that allows performing these functions is a di-block copolymer. In general, a block copolymer consists of a chain of two chemically distinct immiscible monomers, which self-assemble into phase separated nanometer-sized domains.[4-6] Block copolymers can be self-assembled to make structures with various geometries in different length scales. For instance, they self assemble to form spherical micelles, cylindrical micelles, vesicles, face centered cubic and body centered cubic spherical domains (FCC, BCC), hexagonally packed cylinders, various minimal surfaces (gyroid, F surface, P surface), simple lamellae (LAM), as well as modulated and perforated lamellae (MLAM, PLAM).[7] Tremendous progress in the development of methods to synthesize block copolymers has been achieved over the past two decades and it is now possible to synthesize them with controlled sizes in various architectures as well as with different functionalities, see fig. 2.2.[7]

2.3.1 Structures of self-organization based on dilute block copolymer solutions: Spherical Micelles, Cylindrical Micelles and Vesicles

BCP self assemble into micelles with well-defined sizes and shapes in dilution solutions, both in polar media, such as water, as well as in non polar media, including toluene and chloroform. These micelles have well-defined cores of insoluble A block and a shell/corona of the soluble B block. For example, for the polystyrene-polyvinyl pyridine (PS-PVP) di-block copolymer system, non polar toluene is a selective solvent for PS (B block) while PVP is insoluble in it (A block). Upon dissolution of low concentration of PS-PVP in toluene, micelles are formed with polar PVP cores encapsulated in non-polar PS domains. Importantly, the size of the micelle depends on the length of the polymer blocks. Formation of micelles for di-block, tri-block, graft and heteroarm star polymers

$$\mathbf{Z = Z_0 N_A^{\alpha} N_B^{-\beta}} \;\ldots\ldots\ldots\ldots\ldots\ldots(1)$$

is described by equation 1, where Z is the aggregation number (number of block copolymers in a micelle); N_A is the degree of polymerization of the insoluble block; $\alpha = 2$; $\beta = 0.8$ and Z_0 depends mainly on the enthalpy of mixing between insoluble polymer block A and solvent.[8-11] Thus, the aggregation number and the size of the micelle can be controlled by manipulating the degrees of polymerization of the polymer blocks.

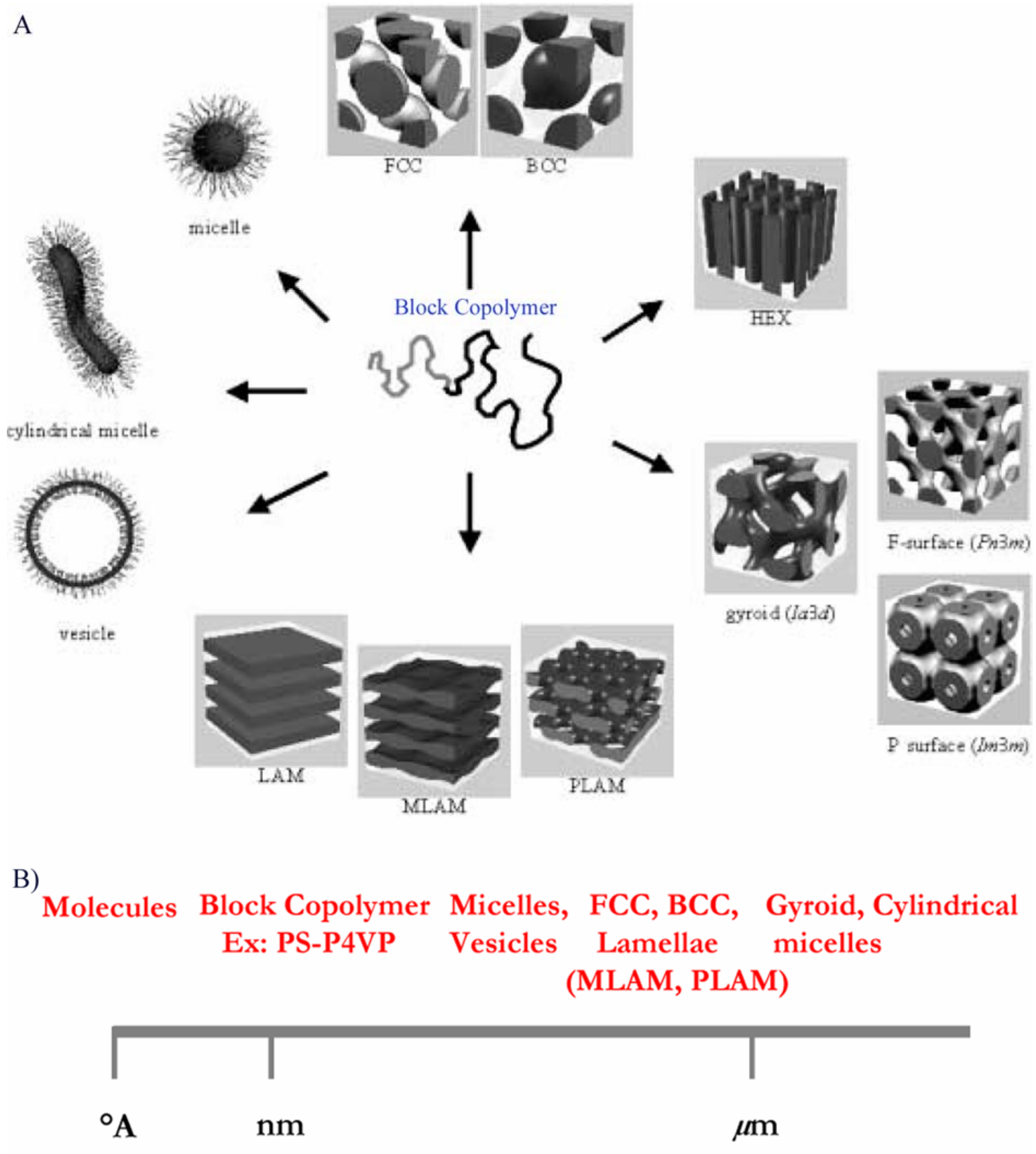

Figure 2.2: (a) Self-assembled structures of BCPs: spherical micelles, cylindrical micelles, vesicles, face centered cubic and body centered cubic spheres (FCC, BCC), hexagonally packed cylinders, various minimal surfaces (gyroid, F surface, P surface), simple lamellae (LAM), as well as modulated and perforated lamellae (MLAM, PLAM) [7] (b) Typical length ranges of various self-assembled structures.

In some cases, the lengths of the blocks also affect the shape of the micelles. Block copolymers with large soluble B blocks, i.e., with smaller radii of curvature, preferably form spherical micelles, whereas, cylindrical micelles as well as vesicles result from smaller soluble blocks with larger radii of curvature.

Block copolymer micelles could be used as nanoreactors for the synthesis of a wide variety of metal and metal oxide nanoparticles. In this method, dissolution of solvent-favorable and solvent-unfavorable polymer blocks in a corresponding solvent, results in the formation of the micelles with favorable domains encapsulating the unfavorable domains, which form the core of the micelle.

2.3.2 Structures of self-organization based on concentrated solutions of block copolymers: Lyotropic and Bulk phases

Higher concentrations of BCPs induce lyotropic liquid crystalline phases and their range of stability could strongly depend on temperature. The super lattices of block copolymers in lyotropic liquid crystalline phases exist in the form of cubic, hexagonal and lamellar structures.

Block copolymers are present in a micro-phase separated state in bulk as well and numerous morphologies, such as lamellae (LAM), arrays of spherical microdomains (FCC, BCC), hexagonally ordered cylinders (HEX), modulated lamellae (MLAM, PLAM), ordered bicontinuous structures, such as the gyroid and inverse structures have been observed.[12-14] The morphology mainly depends on the relative block length and the stability ranges of the various structures are represented in phase diagrams and have been extensively reported.

2.4 Remarks

By using these phase diagrams one can specifically tailor the morphology of these structures primarily through parameters such as block length and the polymer concentration which makes them amenable for templating inorganic nanoscale materials. These self organized structures offer the possibility of restricting the size of particles to a definite diameter and also preclude agglomeration. Moreover, by carefully tailoring the quantity of the inorganic precursor in the nano/micro domain the particle's size can be further controlled. Lastly, utilizing self-organized structures as templates might also enable in simultaneously addressing themes I and III (described in chapter 1) during the syntheses it itself. Syntheses of noble metal nanoparticles as well as few other transition metal nanoparticles, using BCP templates have been previously reported, however, in most of these studies the sizes of nanoparticles were no smaller than 5 nm in diameter.[15-21] In this work, efforts to synthesize wide variety of transition metals as well technologically important semiconductor nanocrystals in the size range of 1-5 nm is attempted.

References

[1] Falbe J, Regitz M Rompp Lexicon Chemie, Thieme, Stuttgart **1996**

[2] Lexicon der Biologie, Spectrum, Heidelberg **2000**

[3] Anderson P W, Stein D L Self-Organizing systems, Plenum Press, New York **1987**

[4] Foster S, Plantenberg T *Angew. Chem. Int. Ed.* **2002** *41* 688

[5] M. Park, C. Harrison, P. M. Chaikin, R. A. Register, D. H. Adamson, *Science*, **1997**, *276*, 1401-1404.

[6] T. Thurn-Albrecht, J. Schotter, G. A. Kastle, N. Emley, T. Shibauchi, L. Krusin-Elbaum, K. Guarini, C. T. Black, M. T. Tuominen, T. P. Russel, *Nature*, **2000**, *15*, 2126-2129.

[7] (a) Jerome R, Tong J D, *Curr. Opin. Solid State Mater. Sci.* **1998** *3*, 573

(b) Hadjichristidis N, Pispas S, Floudas G A *Block Copolymers: Synthetic Strategies, Physical Properties and Applications* Wiley-Interscience **2003**

[8] Forster S, Zisenis M, Wenz E, Antonietti M *J. Chem. Phys.* **1996** *104*, 9956

[9] Qin A; Tian M, RamiReddy C; Webber S E, Munk P, Tuzar Z *Macromolecules* **1994** *27*, 120

[10] Eckert A R, Webber S E *Macromolecules* **1996** *29*, 560

[11] Voulgaris D, Tsitsilianis C, Grayer V, Esselink E, Hadziionnaou *Polymer* **1999** *40*, 5869

[12] Forster S, Berton B, Hentze H P, Kramer E, Antionetti M Lindner P *Macromolecules* **2001** *34*, 4610

[13] Forster S, Khandpur A K, Zhao J, Bates, F S, Hamley I W, Ryan A J, Bras W, *Macromolecules* **1994** *27* 6922

[14] Hentze H P, Kramer E, Berton B, Foster S, Antionetti M, Dreja M *Macromolecules* **1999** *32* 5803

[15] Antonietti, M.; Wenz, E.; Bronstein, L.; Seregina, M. *Adv. Mater.* **1995** 7(12), 1000-1005

[16] Spatz J P, Mossmer S, Hartmann C and Moller M *Langmuir* **2000** *16* 407

[17] Glass R, Moller M and Spatz J P *Nanotechnology* **2003** *14* 1153

[18] Abes J I Cohen R E Ross C A *Chem. Mater.* **2003** *15*, 1125

[19] Lastella S, Jung, Y J, Yang H, Vajtai R, Pulickel A M, Ryu C Y, Rider D A and Manners I *J. Mat. Chem.* **2004** *14* (12), 1791

[20] Benett R D, Miller A C, Kohen N T, Hammond P T, Irvine D J, Cohen R E *Macromolecules* **2005** *38* 10728

[21] Lu J, Yi S S, Kopley T, Qian C, Liu J Gulari E *J. of Phys. Chem. B* **2006** *110* 6655

Chapter 3

Monodisperse Arrays of Mono- and Bi-metallic Nanocrystals

Abstract

Metal nanoparticles exhibit an appealing array of optical, magnetic and electronic properties that are dependent on their size, shape and crystallinity.[1-6] Research on metal nanocrystals has developed tremendously due to their potential applications in many fields, including biology, electronics and information technology. Although several approaches for producing these materials have been reported in the past decade, a general, large scale method for controlled synthesis of well defined nanoparticles is yet to be found. A general method that enables both synthesis of nanoparticles and their assembly on substrates is critical towards furthering technological applications. In this chapter, **first**, block copolymer templating method for the synthesis of wide variety of mono-metallic nanoparticles with diameters in the range of 1-5 nm is discussed. Nature of interactions between the pyridine unit in the polymer template and the transition metals that are at the core of this approach are then explained in rigor. Extensive characterizations of these arrays of

monodisperse nanoparticles are then presented that include structural (AFM, TEM, SEM) and chemical (XPS, EDS) studies. Experiments investigating the affect of templating parameters on nanoparticles sizes and periodicity are then illustrated in detail. **Second**, the versatility of the BCP to synthesize bi-metallic nanoparticles is then demonstrated. Even as of today, similar studies on hetero bi-, tri-metallic nanoparticles have been lacking, primarily due to difficulties associated with their synthesis and the BCP method provides an exciting prospect in this regard. **Third**, comparisons of the BCP with current syntheses techniques are briefly discussed highlighting the implications for future. A blue-print for exciting future studies is set, including syntheses of linear array of metal nanoparticles as well as enabling single molecule detection using linear arrays of metal nanoparticles which are presented in chapter 7.

3.1 Introduction

Nanoscale materials refer to realm of matter with dimensions in the nanoscale that are intermediate between atoms/molecules and bulk solids. Notable among which are zero-dimensional (0-D) materials, such as metal nanoparticles and semiconductor nanocrystals, 1-D nanomaterials, including semiconducting nanowires and carbon nanotubes, and 2-D thin films. In general, many physical phenomena (material properties) have length scales between 1-100 nm (10-10^7 atoms). New physical phenomena develop in nanoscale systems, which are uncharacteristic of either condensed matter or molecular systems, and are primarily dependent on the physical size of the material.[1-6] Furthermore, the material properties can be tuned by controlling the size of the materials which has provided an exciting prospect for detailed investigations for researchers in many fields. Unraveling the size- and shape-dependent materials properties entails synthesis of homologous nanoscale materials with monodispersity in size, shape, internal structure and surface chemistry. Research efforts to explore such nanostructures have transformed many fields such as materials science, biology, chemistry, etc. in many profound ways and the visible impact is more in biomedicine.[4, 7-8]

0-D nanoscale materials possess unique optical, magnetic, electronic and chemical properties that are a result of size quantization effects as well as of the high number of surface atoms and consequent surface states. Based on their material and electronic properties, they can be largely classified into metal nanoparticles (MNPs) and semiconducting nanocrystals. Metal nanoparticles are particularly interesting nanoscale systems because of the relative ease with which they can be synthesized. More importantly, from the standpoint of understanding the effects on their optical, and their electronic properties, MNPs offer substantial advantage over other systems because their optical constants (dielectric constant) resemble those of bulk metals to exceedingly small dimensions (2-5 nm). Initial interest on MNP research has been spurred by the need to understand the fundamental physical phenomena. Over the last decade extensive efforts were laid to investigate the size effect on their physical properties and fundamental understanding of their basic properties has already been well developed.[1-11] Currently, many investigations on MNPs are focused towards furthering technological applications. While the foregoing discussion is not meant to imply that the optical and electronic properties of MNPs are completely understood or that arbitrary control over the geometry and assembly has been achieved. Many challenges still exist with MNPs based research, for instance, physical properties of MNPs with sizes in the range of 1-5 nm have not been extensively reported. Moreover, many investigations to date have been based on a statistically large numbers of nanoparticles or an ensemble of nanoparticles in disordered arrays, thus, entailing investigations on discrete isolated individual nanoparticles. Although several approaches for producing these materials have been reported in the past decade, a general, large scale method for controlled synthesis of well defined nanoparticles is yet to be found. A general method that enables both synthesis of nanoparticles and their assembly on substrates is critical towards furthering technological applications. While studies on the syntheses and physical properties of mono-metallic nanoparticles have been widely investigated, similar studies on bi-metallic nanoparticles[11] have drawn much less attention, primarily due to difficulties associated with their synthesis. Importantly, the characterization of bi-metallic nanoparticles also presents unique challenges, namely those involving determining the composition of individual elements in the nanoparticles, as well as the state in which they are present, for example, if they are present as an alloy or if one of the elements occupies either substitutional or interstitial positions in the host lattice.

Current key research goals in synthesis of MNPs, include:

[1] A general, large scale, rational and reproducible synthesis technique;

[2] Controlled syntheses yielding monodisperse nanoparticles (standard deviation ≤ 15%);

[3] Controlled synthesis with well defined geometry and surface chemistry;

[4] Hetero bi, tri- and higher MNPs of known composition and structure; and

[5] Controlled assembly of MNPs on substrates during their synthesis or otherwise.

In sum, the reasons for pursing investigations on the synthesis of metal nanoparticles in this study are primarily three-fold: first, develop a general, large scale method that enables both syntheses of MNPs with sizes in the rage of 1-5 nm, as well as their controlled assembly with required densities and patterns on substrates; second, controlled synthesis of 1-D nanoscale materials with uniform physical properties using monodisperse metal nanoparticles as catalysts; third, extend the synthesis method to synthesize hetero bi-, tri- and higher-metallic nanoclusters of known composition and structure.

Organization of this Chapter

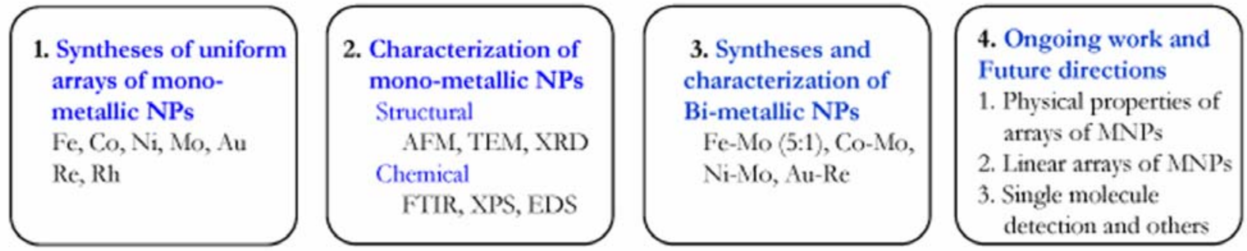

3.2 Experimental Details

Materials

Poly(styrene-b-4-vinyl pyridine) (PS-P4VP) (M_n-PS-b-P4VP: 20000-b-19000; PDI: 1.09) was used as received from Polymer Source, Inc. Iron (III) nitrate [$Fe(NO_3)_3 \cdot 9H_2O$] (Alfa Aesar), Cobalt (II) Nitrate [$Co(NO_3)_2 \cdot 6H_2O$] (Alfa Aesar), Nickel (II) Nitrate [$Ni(NO_3)_2 \cdot 6H_2O$] (Alfa Aesar), Molybdenum(II) acetate dimer [$Mo(OCOCH_3)_2]_2$ (Alfa Aesar), Toluene (Alfa Aesar) were also used as received. 100 nm of silicon di-oxide thermally grown on boron doped p-type Si (100) (Silicon Quest International) were used as the substrates (henceforth, referred to as Si substrates).

Synthesis of mono-metallic nanoparticles: One gram of PS-P4VP di-block copolymer was added to 250 ml Toluene at 70°C and stirred for 4-5 hours. Subsequently, 101 mg (labeled as S1) and 10.1 mg (S5) of $Fe(NO_3)_3 \cdot 9H_2O$, 72 mg (S2) and 7.2 mg (S6) of $Co(NO_3)_2 \cdot 6H_2O$, 72 mg (S3) and 7.2 mg (S7) of $Ni(NO_3)_2 \cdot 6H_2O$, 107 mg (S4) of $[Mo(OCOCH_3)_2]_2$ and, 10.1 mg of $Fe(NO_3)_3 \cdot 9H_2O$, 2 mg of $[Mo(OCOCH_3)_2]_2$ (S8) and 10 mg of Hydrogen tetrachloroauric acid ($HAuCl_4$. $3H_2O$) were each added to 25 ml of the block copolymer solution and stirred for 12 hours at 30°C. The metal precursor loaded micellar solutions were then spin coated on the substrates at 1250 rpm for one minute. Just prior to spin-coating, the substrates were washed in acetone, ethanol and de-ionized water. The micellar films were then treated in oxygen plasma (300-350 mtorr, 5 minutes) (Harrick, Plasma Sterilizer, PDC-32G) to remove the polymer layer.

Synthesis of bi-metallic nanoparticles: Bi-metallic nanoparticles of Fe-Mo {10.1 mg of $Fe(NO_3)_3 \cdot 9H_2O$ and 2 mg of $[Mo(OCOCH_3)_2]_2$}, Co-Mo {7.2 mg of $Co(NO_3)_2 \cdot 6H_2O$ and 2 mg of $[Mo(OCOCH_3)_2]_2)$}, Ni-Mo {7.2 mg of $Ni(NO_3)_2 \cdot 6H_2O$ and 2 mg of $[Mo(OCOCH_3)_2]_2$} and Au-Re were each synthesized in the 5:1 ratio (it should be noted that these ratios correspond to initial loading. The actual amounts of metal precursors that were incorporated could not determined using the existing characterization tools)

Characterization of Nanoparticles

Infrared Spectroscopy: Poly (4-vinylpyridine) (P4VP) monomer (Polymer Source, Inc.) (Mn: 18100; M_w: 20100, M_w/M_n: 1.11) was dissolved in ethanol and Iron (III) nitrate, Co(II) nitrate, Nickel(II) Nitrate, Hydrogen tetrachloroaurate (III), $HAuCl_4.3H_2O$, Rhenium precursors were added to this solution and adjusted to a final concentration of 1mM. A droplet from each solution was then spotted on to 13 mm × 1 mm NaCl polished discs (Wilmad LabGlass) and the samples were subsequently dried in vacuum. The IR spectra were collected on a Nicolet Magna 860 spectrophotometer working at 4000 - 400 cm^{-1} and giving an experimental resolution of 4 cm^{-1}.

AFM studies were carried out using a Nanoscope IV (Digital Instruments) in the tapping mode under ambient conditions using silicon cantilever tips with a radius of curvature ranging between 5-10 nm. An E scanner (which has a higher resolution than a J scanner) with the following scan parameters [Z limit =0.5 μm (maximum=6.3 μm); Amplitude limit = 2 V (maximum = 20V); 512 or 1024 samples/line] was employed in this work.

TEM data was collected using a JEOL 2010, operating at 200 kV. **Plan view** samples for TEM were prepared by mounting the nanocrystals containing side of the Si substrate on a quartz substrate using crystal bond (Aremco), and the other side was mechanically hand-polished until the thickness of the sample reduced to 3-8 μm. Subsequently, the sample was transferred on to a hollow Cu grid (Ted Pella) and was washed in acetone followed by methanol to remove the crystal bond from the front side. The Cu grid containing sample was then ion milled (Dual Ion mill, Gatan Inc) from rear side using an argon ion source with a gun voltage of 6 kV and a gun current of 0.5 mA, until the substrate appeared yellow under white light. **Cross-sectional TEM samples** were prepared by cutting the Si sample with the metal nanocrystals into two halves, which were bonded face on using M-bond adhesive (Ted Pella). Two more Si pieces of similar size were bonded on either side to provide mechanical support. Subsequently, method similar to that of plan view sample preparation was followed.

SEM analysis was performed on a JEOL FEG-SEM 6320 and Phillips XL30 SEM operated at voltages ranging between 1-5 kV.

XPS data were collected on a Kratos Axis 165, using a monochromatic Al K_α with photon energy of 1486.6 eV, giving an experimental resolution of 0.5 eV. Carbon-1s peak was used as an internal reference for the energy calibration of the high resolution spectra.

3.3 Results and Discussion

3.3.1 Polystyrene-poly4vinylpyridine (PS-P4VP) block copolymer templates

The schematic in fig. 3.1 outlines the syntheses details of metal/metal-oxide nanoparticles using PS-P4VP templates. Details for each of the processing steps had been elucidated further in the experimental methods section that follows. Following is a brief summary of the method described in the schematic:

First, reverse micelles of PS-P4VP di-block copolymer were formed in toluene consisting of polar P4VP cores in non-polar PS domains that are capable of self-organizing into ordered structures on substrates.

Second, interaction between the non-bonding electrons on the nitrogen in the pyridine block and the partially filled d- or f-orbital of the transition element results in the formation of coordinate covalent bond that was utilized to sequester metal precursor into the core of the micelles. Appropriate amount of metal precursors were individually loaded in the polymer micelles and stirred for 6-8 hours at 50 °C.

Third, metal precursor loaded polymer micellar solutions were spin-coated on various substrates, which resulted in the formation of a monolayer of micelles along a quasi-hexagonal arrangement on the substrates.

Fourth, oxygen plasma treatment was used to remove the polymeric shell and to reduce the metallic core, resulting in ordered arrays of metal/metal-oxide nanoparticles.

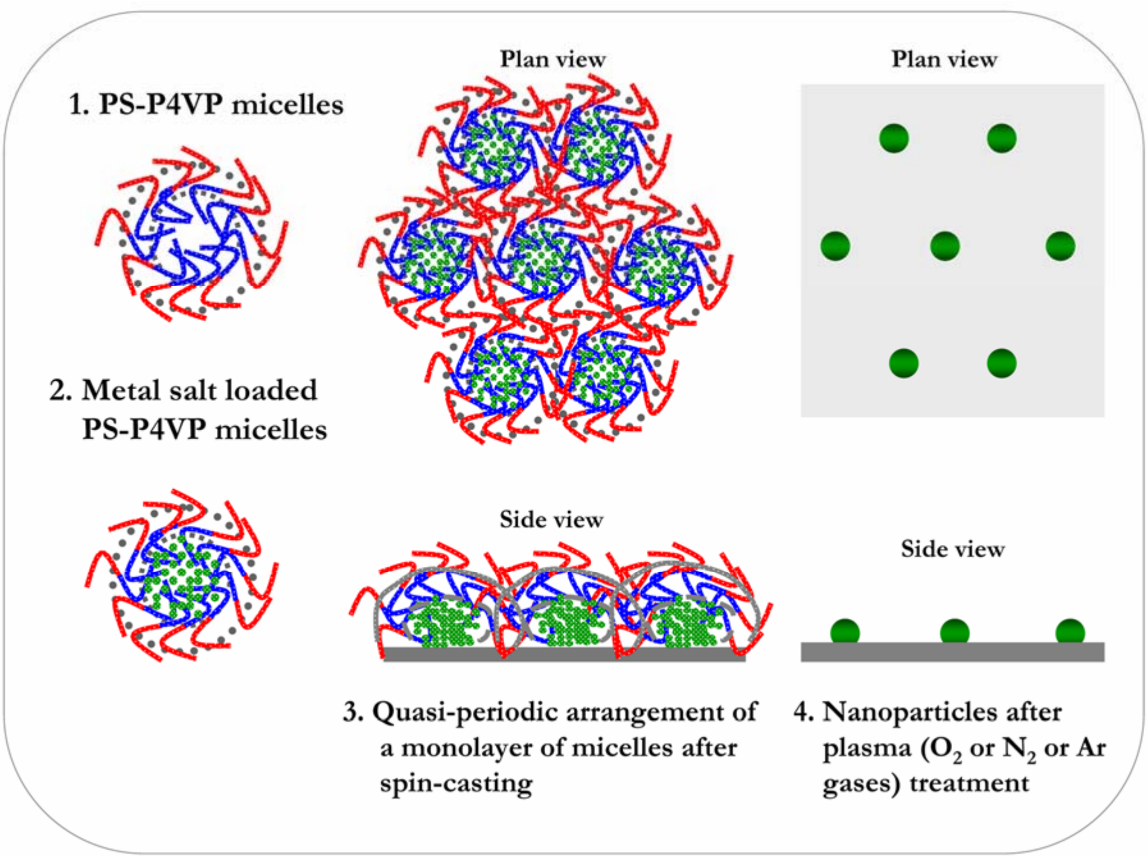

Figure 3.1: Schematic showing the details for synthesis of metal nanoparticles using PS-P4VP di-block copolymer templates. Step 1: Synthesis of PS-P4VP reverse micelles in toluene; Step II, Sequestering metal precursor into the core of the micelle; Step III, Spin coating the metal precursor loaded micellar solution on substrates to form thin films that usually results in the assembly of micelles along a quasi-hexagonal lattice; Step IV, Plasma treatment of thin films to remove the polymeric shell and to form metal/metal oxide nanoparticles.

3.3.2 Synthesis and characterization of mono-metallic nanoparticles

Syntheses of metal nanoparticles (mono-metallic and bi-metallic) using PS-P4VP templates in this study were initially restricted to those metals which could potentially be employed as catalysts for the growth of 1-D nanoscale materials, including carbon nanotubes and semi-conducting nanowires.

Potential ways to utilize micelles as templates or as nanoreactors involved employing chemical interactions between the pyridine units and the metal ions or the metallic compounds. Two such different kinds of interactions are described below

[1] **Weak acid- weak base interactions**: Pyridine is a weak base. A noble metal precursor, such as $HAuCl_4$, is a weak acid. Weak acid-weak base interactions could be employed to segregate metallic compounds into the core of the micelles.

[2] **Metal-ligand coordination**: Coordinate covalent bonds are formed as a result of the interaction between the lone pair of electrons associated with the nitrogen atom in the pyridine group and transition metals with partially filled d- or f- atomic orbitals. These chemical interactions could be utilized to sequester metal ions into the cores of the micelles (nanoreactors). Moreover, the type and stability of the so formed metal-pyridine complex (coordination compound) also depends on the oxidation state of the transition metal atom. In the work described herein, the coordinate compound forming ability of most transitions metals with pyridine has been actuated and, in fact, this is one of the underlying fundamental concepts involved in employing PS-P4VP based templates for the syntheses of mono- and bi-metallic nanoparticles.

Syntheses of noble metal nanoparticles as well as few other transition metal nanoparticles, using BCP templates have been previously reported, however, in most of these studies the sizes of nanoparticles were no smaller than 5 nm in diameter.[chapter2: 15-21] In this work, efforts to synthesize wide variety of transition metals as well technologically important semiconductor nanocrystals in the size range of 1-5 nm is attempted.

Binding between the metal and the pyridine unit in the P4VP block were assessed using infrared (IR) spectroscopic analysis. P4VP exhibits a characteristic signature in the IR spectrum corresponding to the C=N vibrational stretching at 1415 and 1556 cm^{-1}. Upon complexation with metals, a decrease in the intensity of these peaks is observed which is also accompanied with the appearance of a new peak, corresponding to the formation of metal-P4VP coordinate complex. **Figure 3.2** shows the Fourier transform infrared spectra (FTIR) of P4VP with and without the various metal precursors. In most of the cases, a decrease in the intensity of the peaks at 1415 and 1556 cm^{-1} and the appearance of new peaks at 1635 and 1506 cm^{-1}, corresponding to reported transition metals (Co, Ni, Zn, Au)-pyridine complexes indicated a binding between the metal precursor and the pyridine unit. [14a,16]

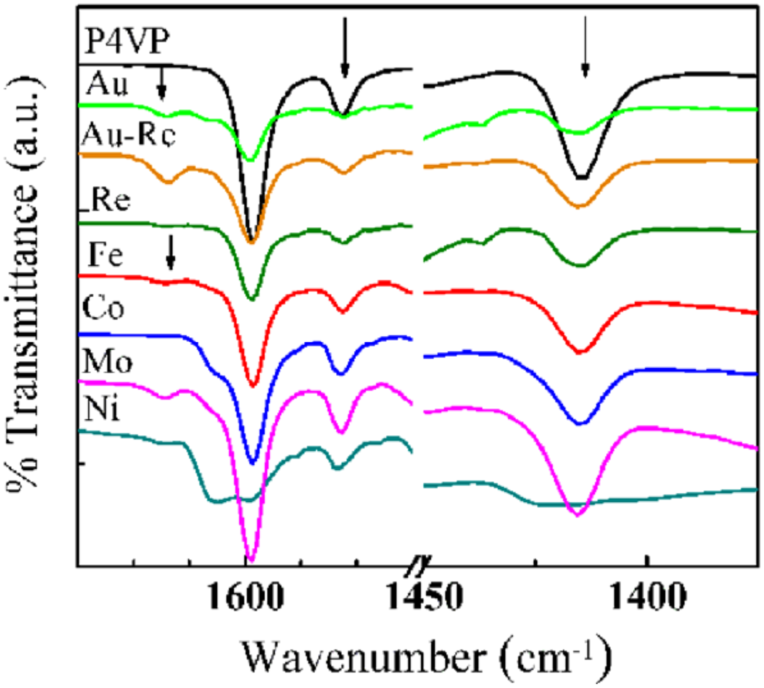

Figure 3.2: Fourier Transform Infrared Spectra of P4VP with and without the addition of various metal precursors. A decrease in the intensity of the peaks at 1415 and 1556 cm^{-1} and the appearance of new peaks at 1635 and 1506 cm^{-1}, corresponding to reported transition metals (Co, Ni, Zn, Au)-pyridine complexes indicated a binding between the metal precursor and the pyridine unit. [14a,16]

The broad peak in the case of Ni-P4VP at 1615 cm^{-1} indicated the formation of a stronger and stable complex. Infrared spectra displayed in **fig. 3.2** led to the inference that the stability of metal-P4VP complexes was in the order Fe(III)-P4VP < Co(II)-PVP < Ni(II)-P4VP, which is also in close agreement with a previous report on the stability of metal-pyridine complexes.[16]

Various transition metal precursors, including Fe, Co, Ni, Mo, etc. were loaded in the di-block copolymer micellar solutions, to form mono-metallic nanoparticles, which were later spin-coated on various cleaned substrates (Si with the native oxide, Si with a 100 nm oxide layer, fused silica and sapphire). Two batches of samples were prepared by controlling the amount of the precursor that was loaded into the micellar templates. Samples S1 through S4 as well as S9 are 10 mM samples, and samples S5 through S8 are 1mM samples (see table 3.1). A representative AFM height image of spin-coated micellar film loaded with iron nitrate precursor as well as the corresponding 3-D image is presented in fig 3.3.

Spin-coating of the metal loaded micellar solutions on substrates resulted in the quasi-hexagonal arrangement of a monolayer of micelles with P4VP cores encapsulated in PS domains. The formation of a monolayer of densely packed polymer micelles on the substrate is governed by Vander Waals interactions, capillary forces acting between the micelles during the evaporation of solvent as well as the surface energy of the substrate. These effects led to the self assembly of PS-P4VP micelles, along a hexagonal lattice with dense packing, since, in a two-dimensional system, hexagonal arrangement of individual motifs conforms to a closest packing. The average height of the micelles and distance between the micelles, as measured from the AFM images, were 25 nm and ~50 nm, respectively. The size (diameter) of the micelles is influenced by: (1) molecular weight of the block copolymer; (2) interactions between the two polymer blocks in the di-block copolymer; and (3) the individual interactions between the polymer blocks and the solvent, which is toluene in this case. The distance between the micelles could be controlled by tuning the molecular weight of the block copolymers.

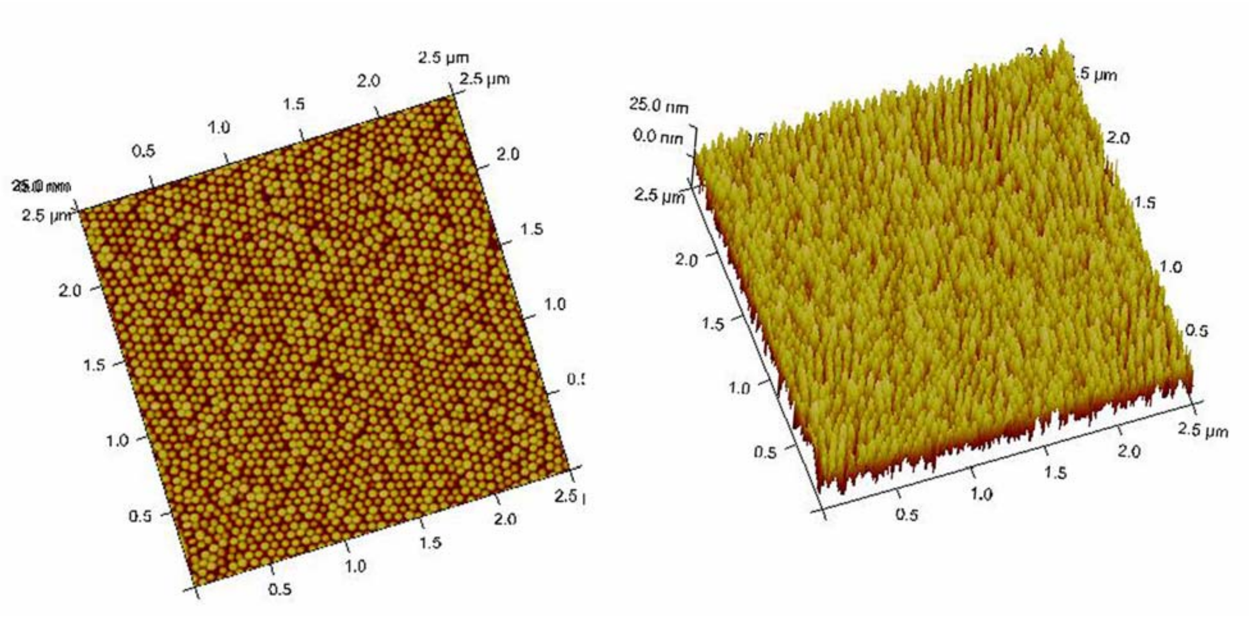

Figure 3.3: Representative AFM images of spin-casted PS-P4VP micelles revealed the monodispersity in their size as well as the ordered arrangement. Short order arrangement of micelles conformed to a quasi-hexagonal lattice. The right image is the corresponding 3-D height image of the illustration shown in the left panel.

Subsequently, the spin-coated micellar film samples were subjected to oxygen plasma treatment to remove the polymer from the micelles as well as to reduce the metallic core to form metal nanoparticles. The representative AFM images with different scan sizes of Mo nanoparticles are displayed in fig. 3.4, and the corresponding 3-dimensional images are also shown in the same figure. The AFM images displaying arrays of different metallic nanoparticles on Si substrate are presented in fig. 3.5. The images in these figures clearly demonstrated the monodispersity in the size of the nanoparticles as well as in their arrangement. Irrespective of whether the micelles were loaded with metal precursors or those that already contained a single nanoparticle in each core, the plasma treatment resulted in the deposition of very fine metal nanoparticles on the bare substrate. The location as well as the arrangement of the nanoparticles was retained after oxygen plasma treatment.

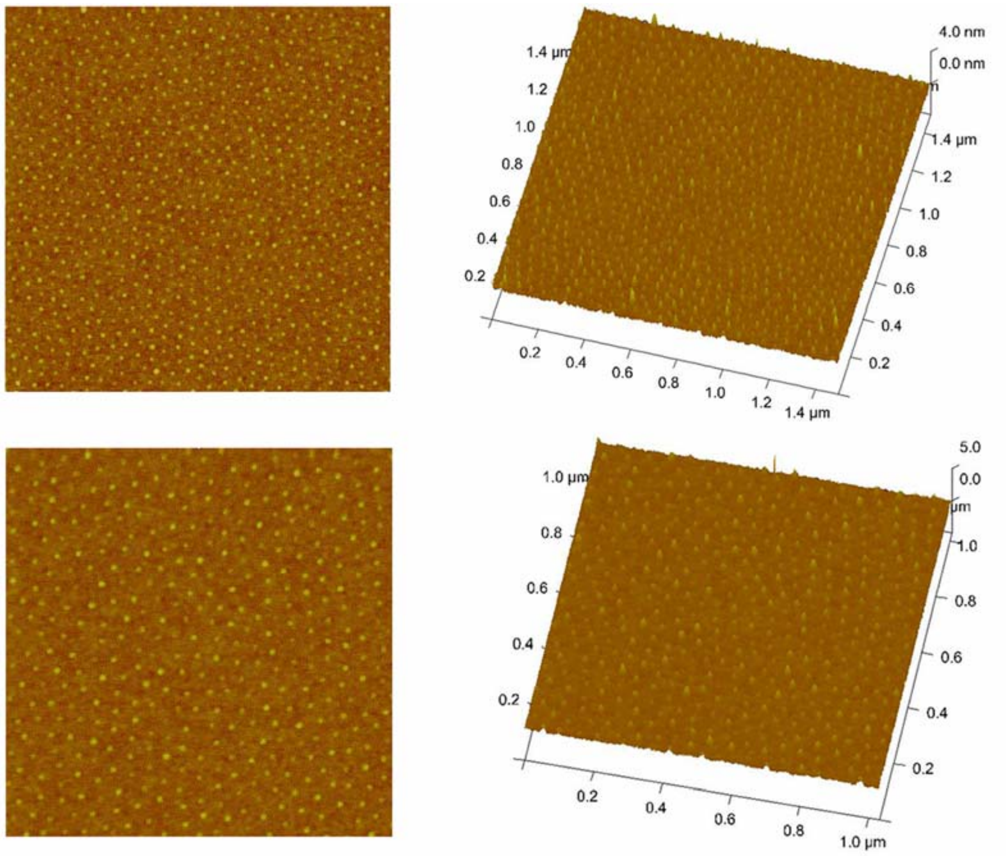

Figure 3.4: Representative AFM height images after oxygen plasma treatment revealed the monodispersity in the size of Molybdenum nanoparticles. The periodicity was retained after plasma treatment. The images shown on the right are the corresponding 3-D height images of the illustrations shown on the left panel.

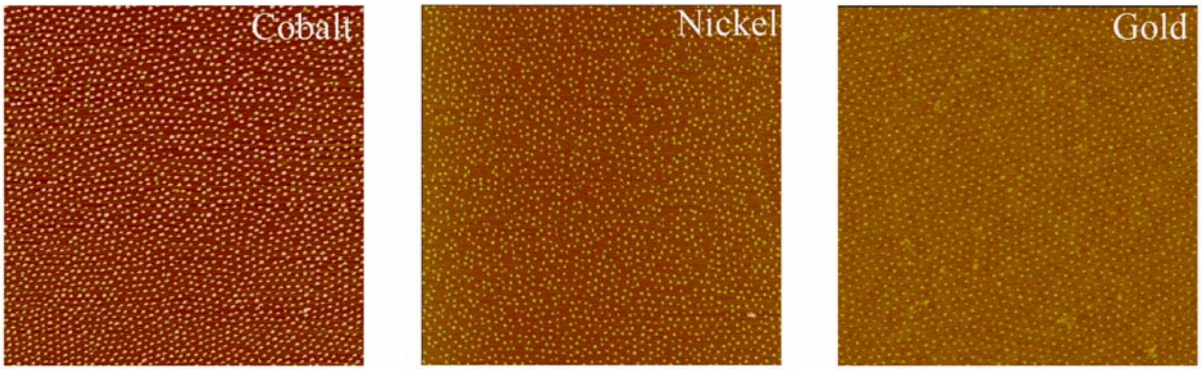

Figure 3.5: AFM height images (2.5 µm × 2.5 µm) of various metal nanoparticles (Co, Ni and Au) on Si substrate.

Table 3.1: Sample details of mono- and bi-metallic nanoparticles.

Sample Details	Chemical State of the metal *	Size ** (nm)	Metal Precursor	Comments
S1	Fe_2O_3	2.5 ± 0.2	Iron (III) nitrate	10 mM samples in PS-P4VP (samples S1-S4)
S2	CoO_x	3.9 ± 0.3	Cobalt (II) nitrate	
S3	NiO_x	3.8 ± 0.3	Nickel (II) nitrate	
S4	MoO_2	-	Molybdenum acetate	
S5	Fe_2O_3	1.1 ± 0.2		1mM samples in PS-P4VP
S6	CoO_x	3.2 ± 0.3	Iron (III) nitrate	
S7	NiO_x	1.9 ± 0.3	Cobalt (II) nitrate	
S8	Fe-Mo (Unknown)	1.3 ± 0.2	Fe (III) nitrate Molybdenum acetate	
S9	AuO_x	3.1 ± 0.4	Gold (IV) Tetrachloroaurate	~1mM sample in PS-P4VP
S10	Co-Mo (Unknown)	-	Cobalt (II) nitrate Molybdenum acetate	(5:1) loading ratio
S11	Ni-Mo (Unknown)	-	Nickel (II) nitrate Molybdenum acetate	
S12	Au-Re (Unknown)	-	Gold (IV) Tetrachloroaurate	
S13	Re (Unknown)	-		

* In this column, the oxidation state of mono-metallic nanoparticles prior to the nanotube growth is indicated.

** Size distribution analysis was performed based on TEM data.

Plasma treatment was employed to remove the polymeric shell as opposed to alternate methods, such as chemical etching, irradiation and heating those samples at elevated temperatures, because of relatively moderate thermal conditions to avoid extensive heating of the samples. Under these experimental conditions, the temperatures during the plasma treatment did not exceed 100 °C. Experiments involving heating the monolayer of micellar samples in air at higher temperatures (~800 °C), to remove the polymeric shell, also yielded good results, though the long range order of the nanoparticles was preserved in this case, the short range ordered was observed to be slightly affected. In either of the cases, the nanoparticles on the bare substrate could not be removed either by ultrasonication or by heating to elevated temperatures as high as 900 °C (see results in chapter 4 and 5), which indicated their stability.

Chemical states of the metal nanoparticles after oxygen plasma treatment were determined based on the XPS analysis. First, the presence of various metals in the different metal nanoparticles samples were confirmed based on the data obtained from the XPS surveys. Then, the chemical states of the metal nanoparticles were determined from high-resolution XPS spectra of their characteristic peaks (for example: Fe-$2p_{3/2}$; Mo-$3d_{5/2}$; Au-$3f_{7/2}$, etc.). Please note that the Al K_a source was employed in these experiments, giving an experimental resolution of 0.5 eV, as compared to an experimental resolution of 1.0 eV, given by Mg K_a source. XPS surveys obtained form various nanoparticles samples, shown in fig 3.6, first confirmed the presence of the various metals. Figure 3.7 displays the high resolution XPS spectra of the characteristic peaks of different metals (Fe-$2p_{3/2}$; Co-$2p_{3/2}$; Ni-$2p_{3/2}$; Mo-$3d_{5/2}$) from samples S1, S2, S3 and S4, after oxygen plasma treatment. Satellite peaks in the high resolution spectra of the Fe, Co and Ni samples are characteristic of most transition metals and are usually known to arise from either multi-electron excitation (electron shakeup) or multiplet splitting.[17,18] The results on the chemical states of the nanoparticles are summarized in Table 3.1.

Table 3.2: Chemical State of metal nanoparticles on Si substrate, after oxygen plasma treatment

Sample Name	High resolution XPS peak position (eV)	Chemical state of metal	Comments
S1 (Fe)	**Fe [$2p_{3/2}$]: 710.9 ± 0.5 ***	**Fe_2O_3**	**-**
S2 (Co)	**Co [$2p_{3/2}$]: 781.0 ± 0.5**	**CoO_x**	**Present as a mixture of oxides**
S3 (Ni)	**Ni [$2p_{3/2}$]: 855.0 ± 0.5**	**NiO_x**	**Present as a mixture of oxides**
S4 (Mo)	**Mo [$3d_{5/2}$]: 229.0 ± 0.5**	**MoO_2**	**-**
S9 (Au; see chapter 5)			

* Experimental resolution of the Kratos XPS instrument is 0.5 eV

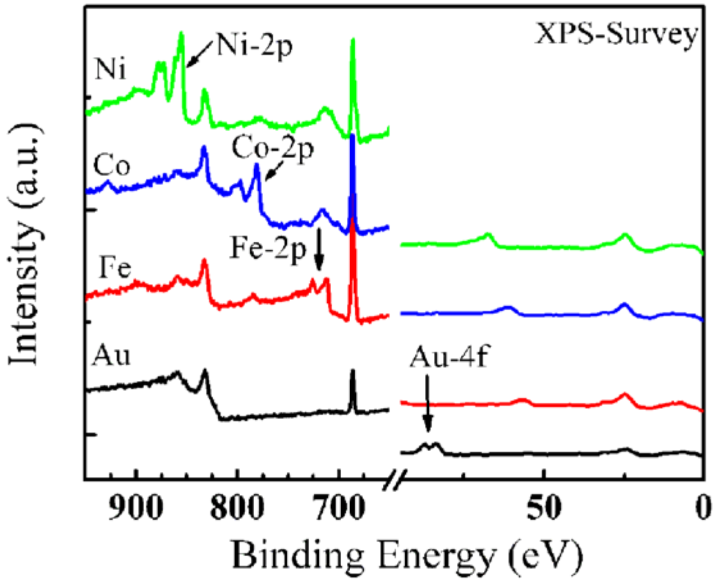

Figure 3.6: XPS surveys of different mono-metallic nanoparticles collected using Al K_α source confirmed their presence.

The presence of Fe-$2p_{3/2}$ peak at 710.9 eV and Mo-$3d_{5/2}$ peak at 229.5 eV indicated that Fe and Mo are present as Fe_2O_3 and MoO_2, respectively.[19] The peaks corresponding to Co-$2p_{3/2}$ and Ni-$2p_{3/2}$ appeared at 781.0 eV and 855.0 eV respectively, suggesting that they are present as a mixture of their oxides.[17,19]

Instead of using oxygen plasma, it is also possible to use hydrogen, nitrogen or argon plasmas to attain the same results. Using plasmas based on neutral gases, such as nitrogen or argon is more advantageous as they reduce the oxidation of metallic elements in the nanoparticles.

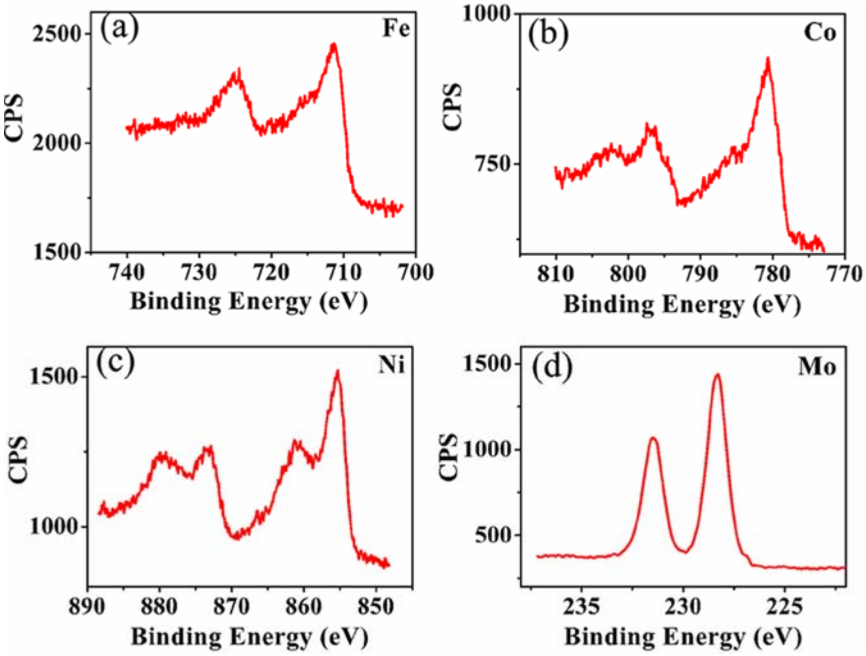

Figure 3.7: High-resolution XPS spectra reveal the chemical states of the nanoparticles after oxygen plasma treatment.

Structural features of the nanoparticles, including their size, their shape and crystallinity were further ascertained using TEM analysis. To determine the actual size and the distance between the nanoparticles, TEM sample preparation of nanoparticles directly on Si substrates was performed. TEM data of metal nanoparticles (S1, S2, S3 and S9) on Si substrate provided accurate measurement regarding the size as well as the distance between the nanoparticles. Figure 3.8 displays the plan (top) view TEM images of various metal nanoparticles on the Si substrate. The observed non-uniformity in the thickness of the underlying silicon substrate seen in these images was a result of ion milling that was performed during the TEM sample preparation. The average size of the nanoparticles for samples Fe (S1), Co (S2) and Ni (S3) were 2.5 ± 0.2 nm, 3.9 ± 0.3 nm and 3.8 ± 0.3 nm, respectively, which demonstrated good control over the nanoparticles' size. The difference in the size of nanoparticles of Fe as compared to the Co and Ni samples is believed to have risen due to (a) use of Fe (III) precursor as compared to Co (II) and Ni (II) precursors for loading in the micelles (the type of coordinate covalent compound formed between the metal and pyridine block depends on the oxidation state of the metal atom[20]) (b) Fe $(NO_3)_3$ is a nonahydrate salt as compared to hexahydrate salts of Co and Ni. As seen in these images, the arrangement of nanoparticles in the form of quasi-hexagonal arrays was retained after oxygen plasma treatment that further corroborated the AFM data. The average distance between the nanoparticles for the Fe, Co and Ni samples was around 45-50 nm, which correlated with the initial distance between the polymer micelles.

The chemical nature of the samples was also confirmed from an EDS, mounted on the JEOL 2010 TEM. A representative EDS spectrum from sample S1 (fig. 3.8) confirmed that the nanoparticles are composed of Fe. The peaks from Si and Cu in this spectrum arose from the substrate and the TEM grid, respectively. Additionally, a 2-D fast Fourier transform (FFT) image (figure 3.8) from an AFM image of Ni nanoparticles (fig. 3.5) showed the arrangement of Ni nanoparticles along a hexagonal lattice that indicated ordered arrangement of the nanoparticles. These results confirmed that the arrangement of polymer micelles played a dominant role in defining the distance between the nanoparticles as well their arrangement on the substrate. Typical lattice-resolved images from samples S2 and S9 revealed the lattice fringes from the nanoparticles and are presented in fig. 3.8. The FFT image of the Au nanocrystals is shown as an inset in this image that revealed that the lattice planes in the nanocrystals corresponded to (111).

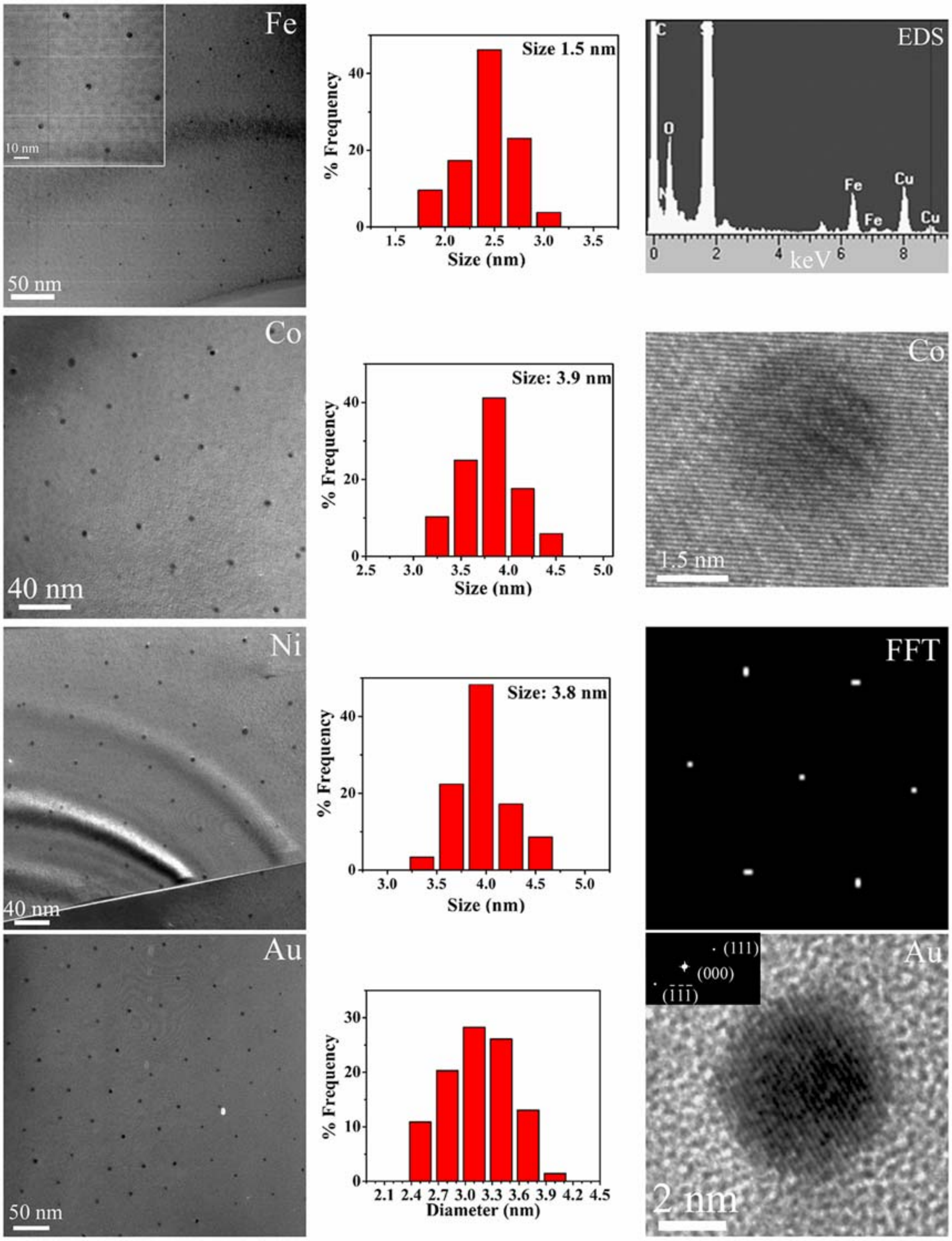

Figure 3.8: Structural characterization of metal nanoparticles. Images in the left row are TEM micrographs of Fe, Co, Ni and Au nanoparticles, respectively (top to bottom). Histograms revealing their sizes are shown in the middle row. Images in the right row showing the EDS spectra, lattice resolved images and the Fourier transform.

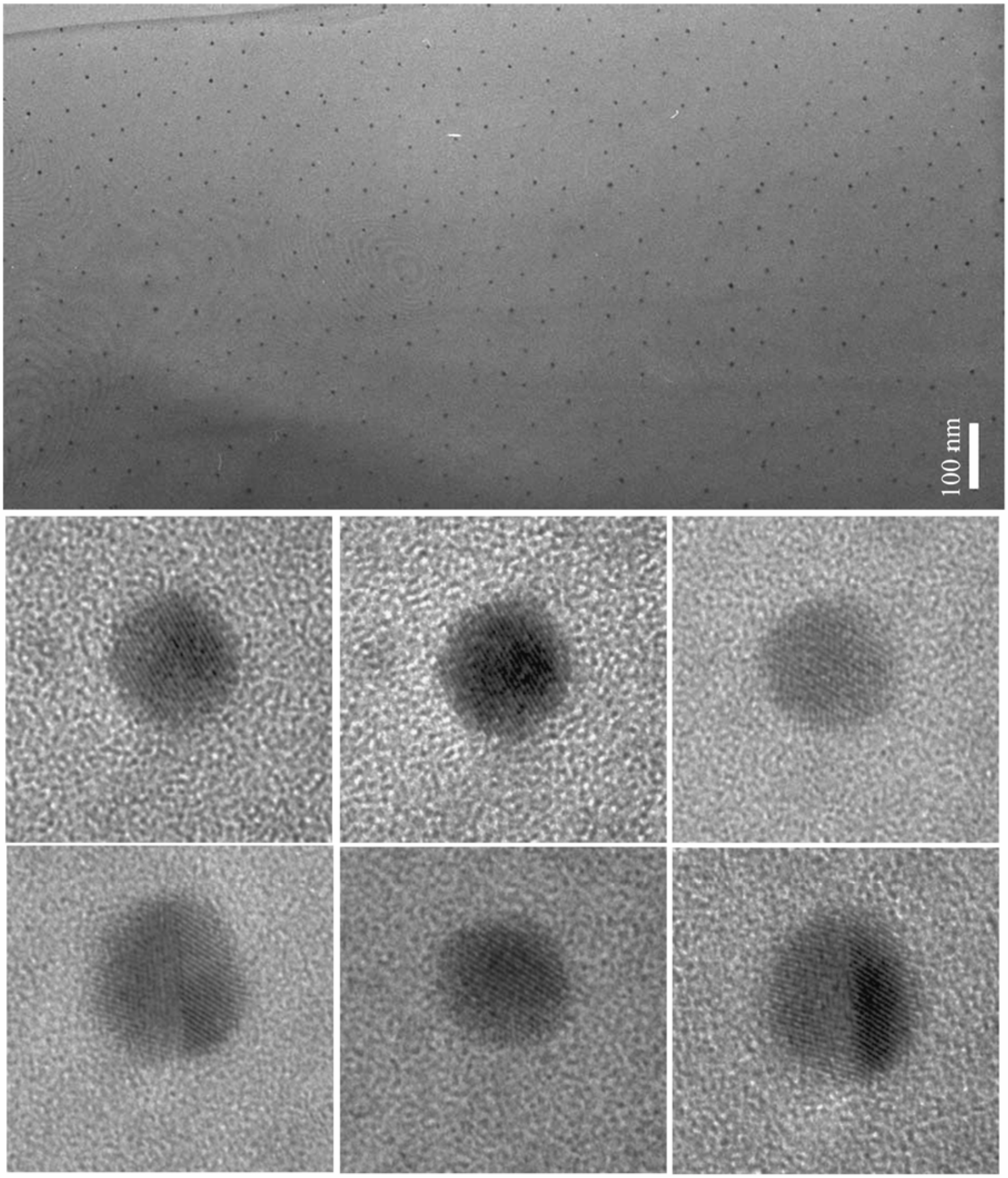

Figure 3.9: High resolution TEM data of metal nanocrystals on Si. A low magnification TEM image of NiO$_x$ revealed the monodispersity in the size and the periodicity of nanoparticles over a large region (above). Lattice resolved images of NiO$_x$ nanoparticles on Si substrate revealed their crystalline nature (below). Most of the nanoparticles were single-crystalline though few of them had grain boundaries.

Additional TEM images revealing the monodispersity as well as the crystallinity of metal nanoparticles are shown in fig. 3.9. In summary, TEM data not only substantiated the AFM data, but also provided additional insight on the structural features of the nanoparticles.

The size of the metal nanoparticle is predominantly influenced by the amount of metal precursor that is loaded in the micelles. To demonstrate the effect of the amount of metal precursor, on the size of the metal nanoparticles, lower amounts of metal precursors were loaded (corresponding to 1 mM concentration) in the polymer micelles : S5 (Fe); S6 (Co); and S7 (Ni). The AFM images displaying arrays of different metallic nanoparticles on Si substrate are presented in fig 3.5. Average height of the nanoparticles, as measured from AFM height images, for samples S5, S6 and S7, were around 1.1 ± 0.2 nm, 3.2 ± 0.3 nm and 1.9 ± 0.3 nm, respectively. The sizes of the Fe (S5), Co (S6) and Ni (S7) nanoparticles reduced in size in comparison to Fe (S1), Co (S2) and Ni (S3), respectively. However, the decrease in the size of nanoparticles from sample S6 was lower compared to those from samples S5 and S7. This result indicated that it is possible to manipulate the size of the nanoparticles to by carefully tuning the amount of metal precursor that is being loaded in the polymer micelle. It is also emphasized that the core size in most PS-P4VP copolymer systems is usually no smaller than 5 nm in diameter. Any efforts to synthesize nanoparticles with smaller sizes should involve precise control over the amount of metal precursor that is loaded in the micelle cores.

Before moving ahead with the discussion, adverse effects related to some of the process parameters as well as imaging techniques on the arrangement of micelles and nanoparticles is emphasized through fig. 3.10. Practical experience has underlined the need for additional caution and care at some of these intermediate processing steps. Interactions between the unpassivated metal nanoparticles and the AFM tip, probably due to surface charges often presented technical

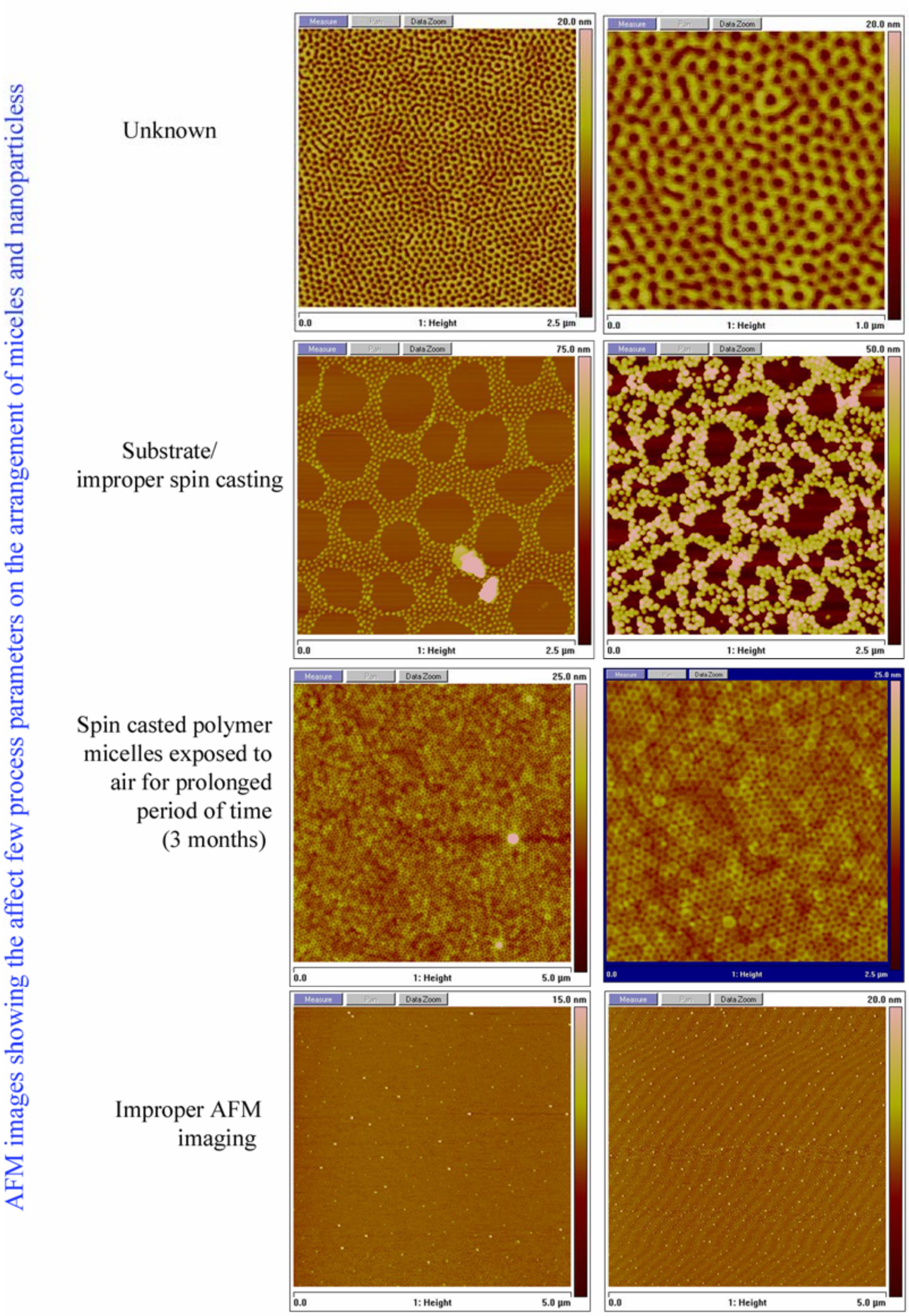

Figure 3.10: When something goes wrong with the experiments. AFM images showing some adverse affects related to the process parameters and imaging techniques on the arrangement of polymer micelles and nanoparticles on the substrate.

challenges and complicated the AFM measurements. This effect was eliminated by using an external source of alpha-radiation to screen the electrostatic charges that were present near and on the sample as well as the AFM tip.

Edge effects — non-uniformity in the thickness of the polymer film was observed after spin-coating, where in the polymer layer was thicker at the edges as compared to the center of the substrate. The non-uniformities were also dependent on the size and the shape of the substrates. Edge affects are harmful, in particular, for catalytic growth of 1-D nanostructures, with higher densities of nanoparticles at the edges than at the center, as they deplete the gas source at the edges rendering the nanoparticles at the center of the substrate inactive for catalysis. The edge effect was eliminated by first spin-casting the substrates on large substrates and then trimming down the edges.

Long standing of thin micellar coated films upon exposure to air for prolonged periods of time resulted in swelling of the micelles, probably due to absorption of oxygen within the micellar cores. This was eliminated by performing plasma treatment soon after spin-casting the micellar solutions on the substrate.

3.3.3 Synthesis and Characterization of Bi-Metallic Nanoparticles:

While studies on the syntheses and physical properties of mono-metallic nanoparticles have been widely investigated, similar studies on bi-metallic nanoparticles have drawn much less attention, primarily due to difficulties associated with their synthesis. In these studies, bi-metallic nanoparticles were synthesized for two reasons; first, to evaluate if the BCP templating method could be extended for their controlled synthesis with different elements in definite amounts; and second, to evaluate if bi-metallic nanoparticle catalysts enhance the yield of single-walled nanotubes (discussed in detail in chapter 5, section 5.5). Molybdenum has been traditionally used as a catalyst support material for the synthesis of nanotubes in a chemical vapor deposition process. It is also well known that Mo is used as a catalyst for the conversion of methane to benzene as it helps in the decomposition of hydrocarbon molecules.[21, 22] Therefore, the presence of Mo as a co-catalyst may enhance the nanotube yield, and hence, the investigations in this report were initially restricted to the synthesis of Fe-Mo, Co-Mo and Ni-Mo nanoparticles.

The bi-metallic nanoparticles, including Fe-Mo (S8), Co-Mo (S10), Ni-Mo (S11) were prepared by simultaneously loading the corresponding metal precursors in the block copolymer micellar solution in a 5:1 ratio. Figure 3.10a displays a representative AFM image from sample S8 after oxygen plasma treatment. The average size of the Fe-Mo nanoparticles as measured from AFM height image is 1.3 ± 0.2 nm. XPS spectra from the bi-metallic samples are presented in (fig. 3.10b, c) in which the characteristic peaks corresponding to different elements are marked. The peaks marked by an asterisk and double-asterisks in fig 3.10b arose from carbon and the silicon substrate respectively. The XPS survey data, confirmed the presence of both the elements in these samples, which is based on the information collected from an ensemble of nanoparticles. However, it did not reveal if each of the nanoparticles composed of both the elements or not. Characterization of bi-metallic nanoparticles presents unique challenges, namely those involving determining the composition of individual elements in the nanoparticles, as well we the state in which they are present, as an alloy or occupy substitutional/interstitial positions in the host lattice. Though traditional characterization techniques, such as TEM, XPS give a fair amount of information, they do not completely provide all the necessary information. It might be possible to determine the composition of the bi-metallic nanoparticles using scanning-TEM-EDS (S-TEM-EDS), which is a rather laborious technique. In this work, an alternate, yet more comprehensive experiment was performed to determine the presence of both Mo and Fe in the same sample. The experiment involved testing a chemical property of the secondary element in the bi-metallic nanoparticles. Fe nanoparticles are known to catalyze single-wall nanotube (SWNTs) growth in a CVD process, but the catalytic yield is usually low. In this experiment, the catalytic yields of Fe, Fe-Mo and Mo nanoparticles for growth of SWNT were compared using ethanol CVD, while Mo nanoparticles by themselves did not catalyze nanotube growth, the catalytic efficiency of Fe-Mo nanoparticles was at least an order of magnitude higher than those observed from Fe nanoparticles, clearly indicating the role as well as the presence of Mo in the nanoparticles. These results are discussed in detail in chapter 5, section 5.5. Alternate ways to detect as well as determining the composition of nanoparticles involve characterizing the physical properties, for example magnetic properties, in the case of transition elements. These experiments though interesting did not constitute towards the goal of this thesis and hence were beyond the scope this work. Future directions for research based on these investigations are listed in the next section. Syntheses of bi-metallic nanoparticles, including Au-Re and Fe-Ru were also pursued for investigating their catalytic effect for nanotube growth.

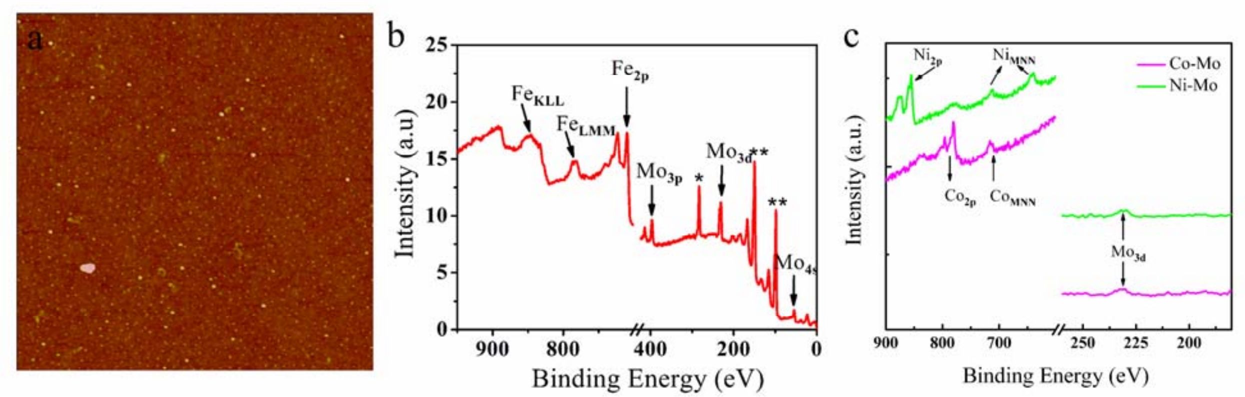

Figure 3.11: Bi-metallic nanoparticles. A representative AFM image (3.0 *μ*m × 3.0 *μ*m) showing Fe-Mo bi-metallic nanoparticles on a Si substrate. XPS surveys for (a) Fe-Mo (sample S8) (b) Co- Mo (sample S10) and Ni-Mo (sample S11) confirmed the presence of both the elements in the samples.

Applications involving the use of monodisperse arrays of mono- and bi-metallic nanoparticles for nanotube growth are discussed in chapter 5.

3.5 Summary

Syntheses of metal nanoparticles and investigations on their physical properties, including electronic, optical and magnetic properties have been extensively reported in the past two decades.[1-11] In spite of many significant advances that were achieved through sustained efforts by many researchers- there are problems which still exist that include controlled synthesis of metal nanoparticles narrow size distribution in the 1-5 nm regime. Although several approaches for producing the nanoparticles have been reported, a general method for the controlled synthesis of nanoparticles in the 1-5 nm size regimes is yet to be found. The reasons for pursing investigations on the syntheses of metal nanoparticles in this study are primarily three-fold: first, develop a general method that enables both syntheses of MNPs with sizes in the rage of 1-5 nm, as well as their controlled assembly with required densities and patterns on substrates; second, controlled synthesis of 1-D nanoscale materials with uniform physical properties using monodisperse metal nanoparticles as catalysts; and third, explore if the technique could be extended for the syntheses of hetero bi-, tri- and higher-metallic nanoclusters of known composition and structure.

Syntheses of ordered arrays of various mono-metallic nanocrystals with controlled average sizes in the range of 1-5 nm (standard deviations~ 10%) utilizing self-assembling properties of dilute solutions of PS-P4VP block copolymer solutions were demonstrated. The unique advantage of this method to synthesize nanocrystals of different metals at room temperature without the need to considerably alter the synthesis conditions is an appealing aspect of this technique. Syntheses of noble metal nanoparticles as well as few other transition metal nanoparticles, using BCP templates have been previously reported, however, in most of these studies the sizes of nanoparticles were in the range of 5-10 nm in diameter, if not more. [chap2:15-21] Herein, the versatility of this technique was further demonstrated by the syntheses of hetero bi-metallic nanoparticles that were reported for the first time. The characterization of bi-metallic nanoparticles presented unique challenges, in particular, determining if both the constituents were present in each nanoparticle, which was confirmed based on the chemical properties of the constituent elements. A combinatorial approach involving BCP technique and gas phase reactions were utilized to synthesize III-nitride semiconductor nanocrystals that further demonstrated the utility of this method, these results are discussed in the next chapter. In chapter 5, size-controlled mono- and bi-metallic nanoparticles that were afore mentioned were employed as catalysts for the diameter-controlled growth of SWNTs. New interesting results on their catalytic activities for nanotube growth are also presented.

Creating complex arrays of nanocrystals assemblies for fabrication of devices is crucial for furthering device applications and this manufacturing issue is by far, one of the most significant impediments to using devices based on nanocrystals. Importantly, the BCP method enables simultaneous control over the size and periodicity of nanocrystals in uniform arrays on virtually any substrate. The first and second order intensity spots in the Fourier transforms of the AFM images revealed the perfect short range ordering of the nanoparticles arrays, however, their long range order was not free with out the defects, though these could be over come by additional steps that have been reported in the block copolymer literature (drying the micellar thin films in the solvent, etc.). Importantly, the BCP technique also allows integration with other combinatorial techniques, in particular, soft-lithography and micro-contact printing, allowing nanoscale molecular assemblies to sub-micrometer and micrometer regimes.

References

[1] Kreibig U, Vollmer M Springer series in Materials Science *25*; Berlin: Springer **1995**

[2] Feldheim D L, Foss C A Marcel Dekker, Inc, New York **2002**

[3] Mirkin C A, Lestinger R L, Mucic R C, Storhoff J J *Nature* **1996** *382*, 607

[4] Pileni, Marie-Paule Syntheses and Properties; Surfactant Science Series **2000** *92* (Fine Particles), 497 (+ references within)

[5] Lue, J.-T. *Journal of Physics and Chemistry of Solids* **2001** 62 (9-10), 1599 (+ references within)

[6] Simon, Ulrich *Nanoparticles* **2004** 329 (+ references within)

[7] Schmid, Guenter; Chi, Li Feng F. *Advanced Materials* **1998** *10* (7), 515

[8] El-Shall, M. Samy; Li, Shoutian. *Advances in Metal and Semiconductor Clusters* **1998** 4 (Cluster Materials), 115

[9] Lisiecki, Isabelle. *Journal of Physical Chemistry B* **2005** *109* (25), 12231

[10] Platonova O A, Bronstein L M, Solodovnikov S P, Yanovskaya I M, Obolonkova E S, Valetsky P M, Wenz E, Antonietti M Colloid Polym Sci **1997** *275* 426

[11] (a) Abes J I, Cohen R E Ross C A *Chem. Mater.* **2003** *15*, 1125; (b) Cheng J, Jung W, Ross C A *Phys. Rev. B* **2004** *70* 064417 1-9

[12] (a) Ng Cheong, Chan Y, Schrock R R, Cohen R E Chem. Mater. **1992** *4* 24; (b) Clay R T, Cohen R E Supramol Sci **1995** *2* 183

[13] (a) Spatz J P, Roescher A, Möller M Adv Mater **1996** *8* 337; (b) Roescher A, Hempenius M, Möller M Acta Polym **1996** *47* 481

[14] (a) Antonietti M, Wenz E, Bronstein L, Seregina M *Adv. Mater.* **1995** 7(12), 1000-1005; (b) Förster S, Antonietti M Adv Mater **1998** *10* 195

[15] Bronstein L, Chernyshov D, Valetsky P, Tkachenko N, Lemmetyinen H, Hartmann J, Förster S Langmuir **1999** *15* 83

[16] Stability constants of metal-ion complexes, 2nd ed., Imprint, Permagon Press: Oxford, New York 1979-1982, Suppl. 2

[17] Kim K S 1975 *Phys. Rev. B* **11** (6) 2177

[18] Briggs D and Seah M P 1995 *Practical Surface analysis by Auger and X-ray Photoelectron Spectroscopy* (John Wiley and Sons: New York)

[19] Moulder J F, Stickle W F, Sobol P E and Bomben K D 1995 *Handbook of X-ray Photoelectron Spectroscopy*, Perkin-Elmer Corporation (Physical Electronics, Inc.: Minnesota)

[20] Cotton F A and Wilkinson G 1998 *Advanced Inorganic Chemistry* (John Wiley and Sons: New York)

[21] Wang L, Tao L, Xie M, Xu G, Huang J and Xu Y *Catal. Lett.* **2003**, *21* 35

[22] Liu S, Wang L, Ohnishi R and Ichikawa M *J. Catal.* **1999,** *181* 175

[23] Brongersma M, Hartman J H, Atwater H A *Phys. Rev. B* **2000** Vol *62* No. 24, R16356-R16359.

[24] Maier S A, Kik P G, Atwater H A *Phys. Rev. B* **2003** *67*, 205402

[25] Sweatlock L A, Maier S A, Atwater H A *Phys. Rev. B* **2005** *71* 235408

[26] Rechberger W, Hohenau A, Leitner A, Krenn J R, Lamprecht B, Aussenegg F R *Opt. Comm.* **2003** *220*, 137 (two Au particles Austria paper)

27] Kelly K L, Coronado E, Zhao L L, Schatz G C *J. Phys. Chem. B* **2003** *107*, 668

[28] El-Sayed M *Accts. Chem. Res.* **2001** *34* No. 4, 257

[29] DeVries G A, Brunnbauer M, Hu Y, Jackson A M, Long B, Neltner B T, Uzun O, Wunsch B H, Stellacci F *Science* **2007** *315,* 358

[30] Moerner W E, Fromm D P, *Rev. of Sci. Instr.* **2003** *74* (8) 3597

[31] Daisuke T, Yoshikazu H, Hiroki H, Satoru S, Yoshihiro K *Nanolett.* **2006** *6*(12), 2642

[32] Chapter 2 references [15-21]

Chapter 4

III-Nitride Nanocrystals Arrays: Controlled Synthesis, Characterization and Optical Properties

Abstract

III-nitrides deserve a special place among semiconductor nanocrystals both from fundamental as well as technological perspectives. III-nitride nanocrystals possess an appealing array of optical properties with great potential for opto-electronic device applications, including laser diodes, photo detectors and UV lasers. To envision devices based on III-nitride nanostructures, not only is it important to achieve their controlled synthesis with uniform size, and hence uniform physical properties, but also the integration of these building units into devices. For example, in spite of significant progress in the synthesis of GaN nanostructures using different methods, it is still a challenge to control their size in the 1-5 nm range. Moreover, to date, there is no efficient way to integrate these nanostructures into functional devices. On the other hand, synthesis of InN

nanoparticles is an interesting prospect for a number of reasons. For example, even as of today, the actual band gap of bulk InN is still a subject of debate. In this chapter, the first demonstration of uniform arrays of monodisperse III-Nitride nanocrystals in the size range of 1-5 nm (standard deviation ~ 10%), on a variety of substrates, using PS-P4VP di-block copolymer template, is presented. **First**, complexation between the pyridine unit in the P4VP block and the p-block elements (Al, Ga and In) were evaluated. **Second**, syntheses of monodisperse arrays of III-nitrides NCs, including GaN and InN, with sizes 1-10 nm are discussed. **Third**, photoluminescence (PL) properties of these nanocrystals are presented. A blue-shift in the photon emission in the PL spectrum of GaN NCs indicated that the NCs were in the quantum confined regime. The underlying physics of the PL data from nanocrystals along with a brief description of the various factors that affect the PL spectrum, which include, size related quantum confinement effects, defects in nanocrystals, piezoelectric effects associated with the wurtzite crystal structure and surface states are also briefly discussed. **Finally**, versatility of this synthesis method is further demonstrated by (1) syntheses of binary compounds of (Ga, In) nitrides, and (2) doping GaN with Eu^{3+} and Mn^{2+} ions. While the studies on the later two aspects are still in their infancy, initial results show significant promise and pave an exciting prospect for future studies.

4.1 Introduction

Semiconductor nanocrystals have been actively investigated in the past few decades. An initial interest in these nanostructures arose primarily from a fundamental physics perspective (to understand size related quantum confinement effects), which had been further driven largely by the potential device applications, particularly for opto-electronic applications, such as laser diodes, photo detectors, UV lasers, etc. Semiconductor nanocrystals (NCs) are based on either element semiconductors, such as Si/Ge[1] or compound semiconductors that include, but are not restricted to, II-VI (CdS, ZnS, CdSe, ZnSe, etc),[2-3] III-V (GaAs, InP, III-nitrides, etc)[4-9] and IV-VI (PbS, PbTe, etc).[10] Wide band gap materials such as III-nitrides deserve a special place in this list for the following reasons:

(1) Unlike many other compound semiconductor NCs (GaAs, ZnS, CdS), the fundamental electronic structure of some of the III-nitrides has not yet been investigated in detail. For example, even as of today, the actual band gap of InN is still a subject of intense debate;

(2) While most III-V compounds have a cubic (Zinc blende) structure, III-nitrides and related nitride alloys also exhibit wurtzite structure, which gives rise to strong piezoelectric effects due to built-in electric fields. As a consequence, these nanocrystals usually exhibit a red-shift in the photoluminescence spectra leading to interesting effects on their optical properties;

(3) III-nitrides exhibit attractive physical properties with potential opto-electronic applications. For example, it is well known that GaN exhibits a PL emission in the ultra-violet (UV) region and InN is theoretically known to have a PL response in the infrared (IR) region. Thus, binary compounds of Ga and In nitride are theoretically predicted to have emission in the intermediate visible and the near-IR ranges, indicating that these materials

could be potentially used to map opto-electronic applications that span the entire optical spectrum in the UV-IR regime;

(4) The electronic properties of III-nitrides could be combined with either the optical or the magnetic properties of transition metals (TM) giving rise to appealing new effects. For example, doping rare-earth ions, such as Eu^{3+} in GaN nanocrystals could be employed to enhance the emissions from Eu^{3+} ions in the visible region, with promising applications for red LEDS. In a similar vein, by doping TMs, including Eu and Mn ions, their magnetic properties could be combined with the electronic properties of GaN to result in spintronic effects.

III-Nitride nanocrystals: Current state of research and present challenges

III-Nitrides have received immense attention over the past decade as potential materials with successful opto-electronic applications, including blue light-emitting diodes, lasers, field effect transistors and ultra-violet photodiodes.[10-13] For example, GaN nanostructures, including nanocrystals and nanowires with size less than 10 nm (Bohr-exciton radius 2-10 nm)[14-15] exhibit attractive optical properties largely due to quantum confinement effects. Current efforts are focused on the synthesis as well as on understanding the physical properties of crystalline GaN nanoparticles. Investigations on the synthesis of GaN nanoparticles, including colloidal methods,[14] solvo-thermal methods,[16-17] detonation of gallium azide and cyclotrigallazanes,[18-21] metallo-organic chemical vapor deposition (MOCVD)[22] and molecular beam epitaxial methods[23] have been previously reported. However, in spite of significant progress in the synthesis of GaN nanoparticles using different methods, it is still a challenge to synthesize nanoparticles with controlled size and shape uniformity in the *1-5 nm* size range. Moreover, in many cases the nanoparticles tend to agglomerate, making it difficult to study the optical properties from individual isolated nanoparticles.

Though MOCVD and MBE methods offer good control over the size of the nanoparticles, these methods are limited by the need for lattice match substrates and are relatively more expensive processes.

On the other hand, synthesis of InN nanoparticles is an interesting prospect for a number of reasons. For example, currently, the actual band gap of bulk InN is still a subject of debate- recent reports on the band gap of InN (0.7 -1.1 eV) are in sharp contrast to earlier cited reports (1.8-2.0 eV).[24-25] In addition, it has rather been difficult to synthesize pure InN for several reasons: (i) a need for higher equilibrium vapor pressure of nitrogen as compared to that of other nitrides; (ii) need for lattice matched substrates; and (iii) lower decomposition temperature of InN (~500 -700 C).[16]

Although concerted efforts have been laid on III-nitride synthesis, the results to date are modest. Moreover, as described above, syntheses of III-nitrides still pose considerable challenges. In summary, controlled syntheses of nitride nanocrystals is entailed not only for further understanding their fundamental physical properties, but also for furthering opto-electronic device fabrication.

Organization of this chapter

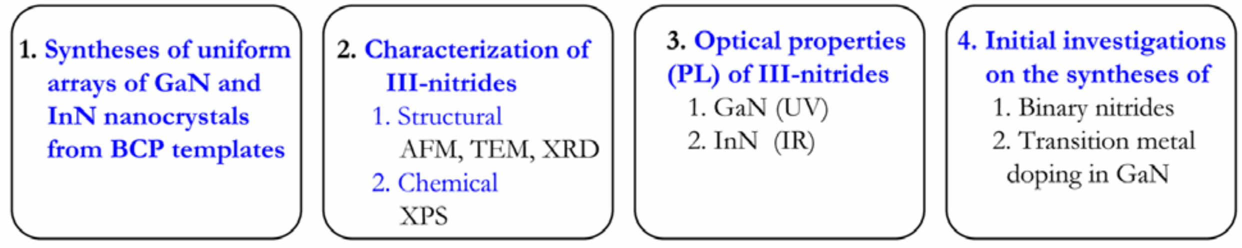

1. Syntheses of uniform arrays of GaN and InN nanocrystals from BCP templates

2. Characterization of III-nitrides
1. Structural
   AFM, TEM, XRD
2. Chemical
   XPS

3. Optical properties (PL) of III-nitrides
1. GaN (UV)
2. InN (IR)

4. Initial investigations on the syntheses of
1. Binary nitrides
2. Transition metal doping in GaN

4.2 Syntheses of III-nitrides using PS-P4VP Templates

Summary of the technique

The schematic in fig. 4.1 outlines the syntheses details of nitride nanocrystals using the combinatorial approach involving block copolymer templates and gas phase reactions. Details for each of the processing steps had been elucidated further in the experimental methods section that follows. Following is a brief summary of the method described in the schematic

First, reverse micelles of PS-P4VP di-block copolymer were formed in toluene consisting of polar P4VP cores in non-polar PS domains that are capable of self-organizing into ordered structures on substrates.

Second, Interaction between the non-bonding electrons on the nitrogen in the pyridine block and the partially filled p-orbitals of these metallic p-block elements results in the formation of coordinate covalent bond that was used to seclude metal ions into the core of the micelles. Ga and In precursors were loaded in the polymer micelles and spin coated on various substrates, which resulted in a monolayer of micelles in a quasi-hexagonal arrangement on the substrates.

Third, oxygen plasma treatment was used to remove the polymeric shell and to reduce the metallic core, resulting in ordered arrays of metal oxide nanoparticles.

Finally, these arrays of nanoparticles were treated with ammonia in a chemical vapor deposition (CVD) reactor at temperatures in the range 500-750 °C at atmospheric pressure to grow crystalline nitride nanocrystals suing two slightly different methods.

In an alternate experiment, instead of oxygen plasma, first, N_2 plasma was used to remove the polymeric shell resulting directly in the formation of GaN nanoparticles. The N_2 plasma treatment resulted in a mixture of amorphous and crystalline nanoparticles, requiring an annealing treatment at higher temperatures to improve the crystallinity of nitride nanoparticles.

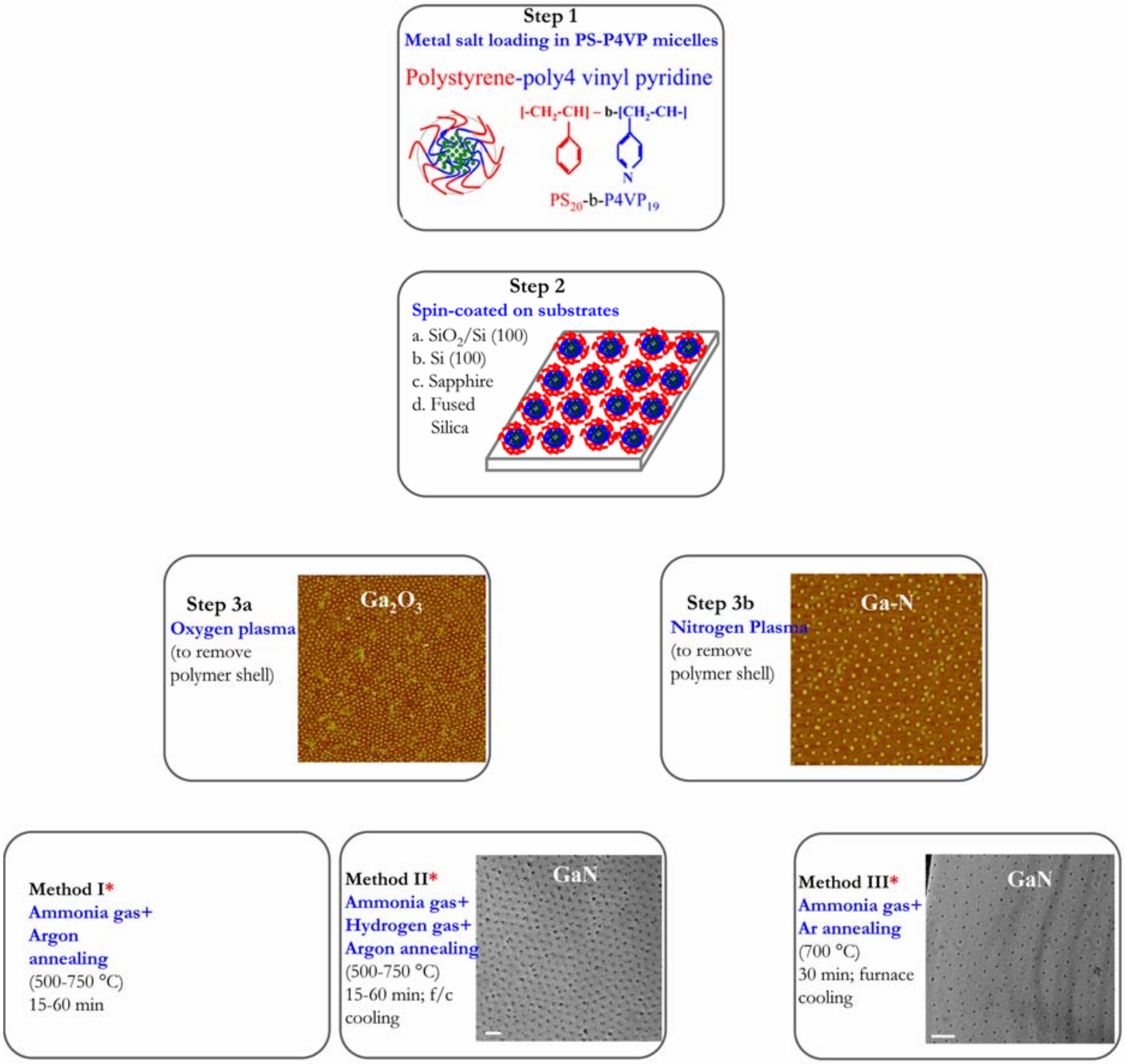

Figure 4.1: Flowchart for synthesis of III-nitrides using PS-P4VP template.

*Note: temperatures and anealing times indicated for methods 1-3 are applicable for GaN syntheses alone. These vary for InN and other binary compounds.

4.3 Experimental Methods and Materials

Synthesis of arrays of metal loaded polymer micelles: Polystyrene- poly4vinyl pyridine (PS-P4VP) micellar solution was prepared by adding 0.2 g of PS-P4VP (Polymer Source, Inc.,) (Mn-PS-b-P4VP: 20000-b-19000; PDI: 1.09) to 50 ml of toluene (Alfa Aesar) and stirred at 70 °C for 4 hours. Gallium Nitrate [$Ga(NO_3)_3.xH_2O$, 99.999%] (Sigma Aldrich) (6 mg) and gallium (III) acetylacetonoate [$(C_5H_8O_2)_3Ga$, 99.99 %] (Aldrich) (9 mg) (henceforth referred to as GaAc) precursors were each added to 25 ml of the polymer micellar solution and stirred for 12 hours at room temperature. These solutions were then spin-coated on three different substrates: sapphire, 100 nm of silicon di-oxide thermally grown on boron doped p-type Si (100) (henceforth, referred to as Si substrates, Silicon Quest International, Inc.) and fused silica glass substrates. The samples were spin coasted at 1250 RPM for one minute. Spin coating resulted in the formation of quasi-periodic arrangement of a monolayer of Ga loaded polymer micelles. The polymeric layer was removed using oxygen plasma treatment (300-400 mtorr, 5 minutes) (Harrick, Plasma Sterilizer, PDC-32G).

Synthesis of arrays of GaN NCs: Gallium oxide nanoparticles obtained by O_2 plasma treatment were treated with ammonia using two different methods in a thermal CVD. Both methods were performed at ambient pressure, with temperature ranges of 600-800 °C, in a 2.5 cm diameter quartz tube with a 37.5 cm heating zone. In the first method (Method 1; fig. 4.1), substrates with gallium oxide nanoparticles (obtained from GaAc precursor loaded polymer micelles) were heated from room temperature to the growth temperature in a flow of argon gas (600 sccm). Subsequently, nitride growth was initiated by adding ammonia (60-100 sccm) to the argon gas flow and continued for 15 minutes. The growth was terminated by switching off the ammonia flow and the samples were cooled in an argon gas flow. In the second method (Method 2; fig. 4.1), all the steps were similar except the first step, where the nanoparticles coated substrates were heated to final growth temperatures in a gas mixture of argon (600 sccm) and hydrogen (100 sccm). Hydrogen gas was used to reduce the oxide nanoparticles to the metallic state and to further enhance the nitride reaction. In another experiment (Method 3; fig. 4.1), N_2 plasma (300-400 mtorr, 5 minutes) (Harrick, Plasma Sterilizer, PDC-32G) was used to remove the polymer and the samples were subsequently annealed in a flow of ammonia gas (NH_3/Ar: 60/600 sccm) in a CVD reactor at temperatures above 700 °C to form crystalline GaN nanoparticles.

Synthesis of arrays of InN NCs: Indium acetyl acetonoate (10.3 mg in 25 ml of PS-P4VP solution) precursor loaded polymer micelles were spin-casted on Si substrate and subsequently, the polymer shell was removed using N_2 plasma (350-400 mtorr, 5 minutes) (Harrick, Plasma Sterilizer, PDC-32G). Finally, the samples were annealed in ammonia gas (NH_3/Ar: 60/600 sccm) in a CVD reactor at temperatures around 550-600 °C to form crystalline InN nanoparticles.

Infrared Spectroscopy: Poly (4-vinylpyridine) (P4VP) monomer (Polymer Source, Inc.) (Mn: 18100; M_w: 20100, M_w/M_n: 1.11) was dissolved in ethanol. Aluminum (III) nitrate [$Al(NO_3)_3.9H_2O$] (Alfa Aesar), Gallium(III) nitrate [$Ga(NO_3)_3.xH_2O$] and Gallium(III) acetylacetonate [$(C_5H_8O_2)_3Ga$] and Indium nitrate [$In(NO_3)_3.xH_2O$, 99.999%] (Sigma-Aldrich) precursors were added to this solution and adjusted to a final concentration of 1mM. A droplet from each solution was then spotted on to 13 mm × 1 mm NaCl polished discs (Wilmad LabGlass) and the samples were subsequently dried in vacuum. The IR spectra were collected on a Nicolet Magna 860 spectrophotometer working at 4000 - 400 cm^{-1} and giving an experimental resolution of 4 cm^{-1}.

XRD spectra were collected on a Rigaku X-ray powder diffractometer operating at 50 kV and with a current of 200 mA with a Cu-Kα radiation. GaN-XRD samples were prepared by vacuum-drying a droplet of the micellar solution on fused silica glass substrates for few hours prior to oxygen plasma treatment. Subsequently, ammonia treatment was employed to synthesize GaN nanoparticles at the same conditions as previously described. InN-XRD samples were prepared by vacuum-drying a droplet of the micellar solution on fused silica glass substrates for few hours prior to nitrogen plasma treatment and ammonia treatment.

PL spectra of GaN nanocrystals on Si substrates were collected at room temperature, using excitation energy of 260 nm (4.77 eV) obtained from a Xenon lamp using Horiba Jobin Yvon spectrophotometer (Nanolog). The total power of the lamp was 500 W (across the entire optical spectrum). The integration times varied based on the type of the nanoparticles as well as the underlying substrate.

4.4 Results and Discussion

4.4.1 Infrared spectroscopic analysis

To date, many investigations on the syntheses of metal nanoparticles using the BCP templates have been confined to transition metals alone. To determine whether these templates could be used for the syntheses of nanocrystals based on metallic elements in p-block, it was first imperative to determine whether complexation between pyridine and these elements is feasible or not. It should be noted that the discussion in this chapter is restricted only to metallic elements present in group 13.

Binding between the metal (Al, Ga and In) precursors and the pyridine unit in the P4VP block were assessed using infrared (IR) spectroscopic analysis. Figure 4.2 shows the Fourier transform infrared spectra (FTIR) of P4VP with and without the various metal precursors. In the case of Ga and Al nitrate precursors, a decrease in the intensity of the peaks at 1415 and 1556 cm^{-1} (characteristic peaks corresponding C=N stretching vibrations in pyridine units)[33] and the appearance of new peaks at 1635 and 1506 cm^{-1}, corresponding to reported transition metal (Co, Ni, Zn, Au)-pyridine complexes,[29, 33] indicated a binding between the Al/Ga and the pyridine unit. In the case of indium nitrate precursor, the appearance of a new peak in the spectra at 1616 cm^{-1}, a result of protonated pyridine,[30] indicated an interaction between the In and the pyridine unit.

In addition, the interaction between metallo-organic salts, such as GaAC and P4VP were also investigated. The overlapping vibrational absorptions from the individual constituents in the GaAc-P4VP spectra in the 1600-1380 cm^{-1} frequency range complicated the ability to unambiguously detect the peaks that arose from the Ga-pyridine complex. However, the appearance of a new peak in the spectra at 1616 cm^{-1} indicated an interaction between the Ga (from GaAc precursor) and the pyridine units. This result indicated that the complexation between the metallic elements in group 13 with pyridines was feasible, and hence, PS-P4VP block copolymer micelles could be potentially used as nanoreactors for the synthesis of oxide and nitride nanoparticles, including Al, Ga and In as well as their ternary elements.

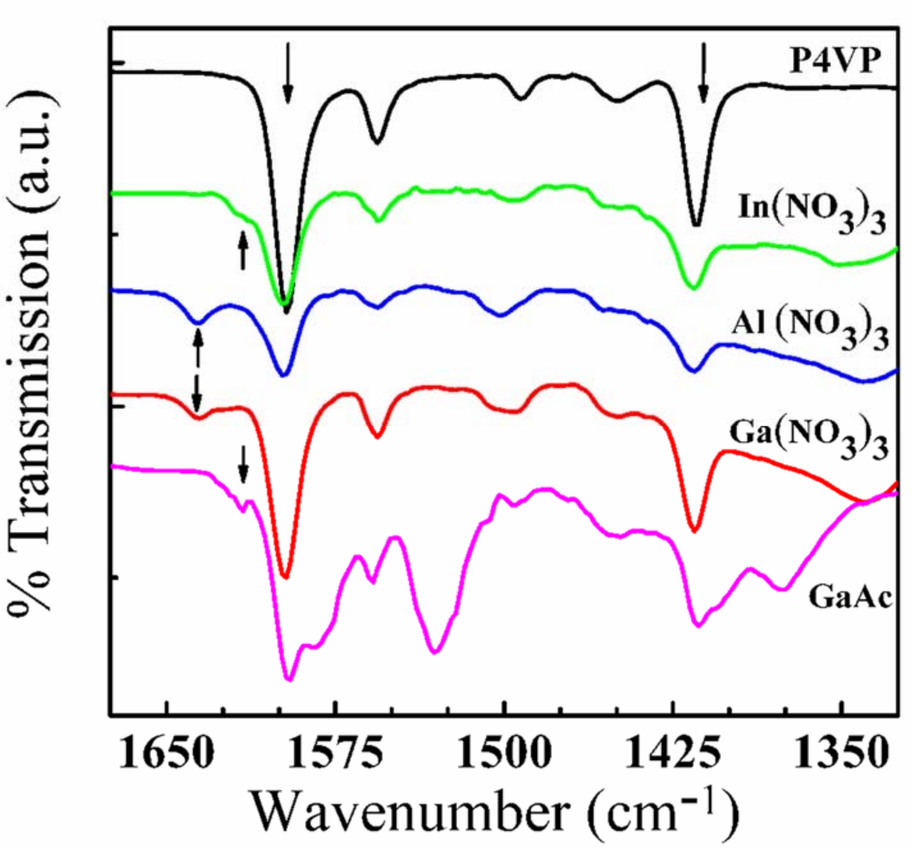

Figure 4.2: FTIR spectra of P4VP with and without various group XIII metal precursors.

4.4.2 Structural Characterization of GaN NCs: Microscopy Analysis

The size and the periodicity of the nanoparticles that were obtained after oxygen and nitrogen plasma treatments (step IIIa, fig. 4.1) were determined using AFM studies. Representative AFM height images (2.5 μm × 2.5 μm) of Ga based nanoparticles that were formed after O_2 and N_2 plasma treatments are shown in fig. 4.3a and fig. 4.3b, respectively. It should be noted that convolution of AFM tip (with radius of curvature in the range 5-10 nm) with features in the size range of 1-5 nm is likely to overestimate the width of the nanoparticles, and only the height measurements of the features are reliable to measure their size. Hence, all the size analysis reported herein, are based on the AFM height measurements. As measured from the AFM height images, the average height of the Ga_2O_3 nanoparticles obtained from O_2 plasma was 4.2 ± 0.4 nm and the corresponding value for GaN nanoparticles obtained from N_2 plasma was 4.4 ± 0.4 nm. The average distance between the nanoparticles was around 45-50 nm. Moreover, there was no noticeable difference in the nanoparticles that formed on different substrates (Si, sapphire, fused silica glass). The 2-dimensional fast Fourier transform (FFT) image (inset in fig. 4.3), revealed an ordered arrangement of nanoparticles along a hexagonal lattice, and the appearance of the second order intensity peaks in the FFT spectrum indicated highly ordered arrangement of the nanoparticles.

Before moving on to discuss TEM analyses, different syntheses methods that were employed are further elucidated in this section. The uniform arrays of gallium oxide nanoparticles (chemical state of nanoparticles was confirmed using XPS and this result is discussed later) obtained by O_2 plasma treatment were then treated with ammonia using two different methods (step 3a, fig. 4.1).

(1) *In the first method*, gallium oxide nanoparticles were directly treated with ammonia gas at reaction temperatures to form GaN nanocrystals.

(2) *In the second method*, gallium oxide nanoparticles were first reduced using H_2 gas to form Ga (liquid), which was then treated with ammonia to form GaN. Syntheses of bulk GaN from bulk samples of Ga_2O_3 as well from as from liquid Ga, using ammonia gas have been previously reported.[34-35]

The two different syntheses methods involve different sets of reactions for the formation of GaN and are believed to occur as per the following reactions:

$$\text{Method 1: } Ga_2O_3 + 2NH_3 \rightarrow 2GaN + 3H_2O \qquad (1)$$

$$\text{Method 2: } Ga_2O_3 + 3H_2 \rightarrow 2Ga + 3H_2O \qquad (2\text{-i})$$

$$2Ga + 2NH_3 \rightarrow 2GaN + 3H_2 \qquad (2\text{-ii})$$

(3) *In another experiment (Method 3)* (step 3b, fig. 4.1), N_2 plasma was first used to remove the polymeric shell and the samples were then subsequently annealed in a flow of ammonia gas at temperatures above 700 °C to form crystalline GaN nanoparticles.

Detailed structural characterization of nanostructures was completed using TEM analysis. Here, extensive and rigorous TEM analysis was performed to determine the size and the crystallinity of GaN nanocrystals. Importantly, all the TEM data was collected from nanoparticles on Si substrates that involved a meticulous sample preparation. The TEM sample preparation details are provided in the appendix and this methodology was adopted from Prof. Fitzgerald Group, MIT.

A representative TEM image of GaN nanocrystals after ammonia treatment of nanoparticles obtained from oxygen plasma treatment, using method 2, is shown in fig. 4.3c. A TEM image of GaN nanocrystals after ammonia treatment of nanoparticles obtained from nitrogen plasma treatment, using method 3, is shown in fig. 4.3d. The quasi-periodic arrangement of nanocrystals was unaffected by ammonia treatments, suggesting that the nanoparticles were stable at these high temperatures. Representative lattice-resolved images of the GaN nanoparticles corresponding to samples described above are shown in fig. 4.3e and fig. 4.3f, respectively, which revealed the crystallinity. A set of additional TEM images from various regions from the same sample are displayed in 4.3B that reveal the monodispersity in the size and periodicity on the sample.

Using nitrogen plasma as compared to oxygen plasma to remove the polymeric shell would be advantageous: first, absence of oxygen in the precursor material would result in the synthesis of pure GaN nanoparticles; second, the crystallinity of GaN nanoparticles is likely to be better than in the latter case due to the absence of a significant change in volume associated with the different types of chemical bonds (Ga-O vs Ga-N). The latter is evident in the TEM observations of the nanoparticles.

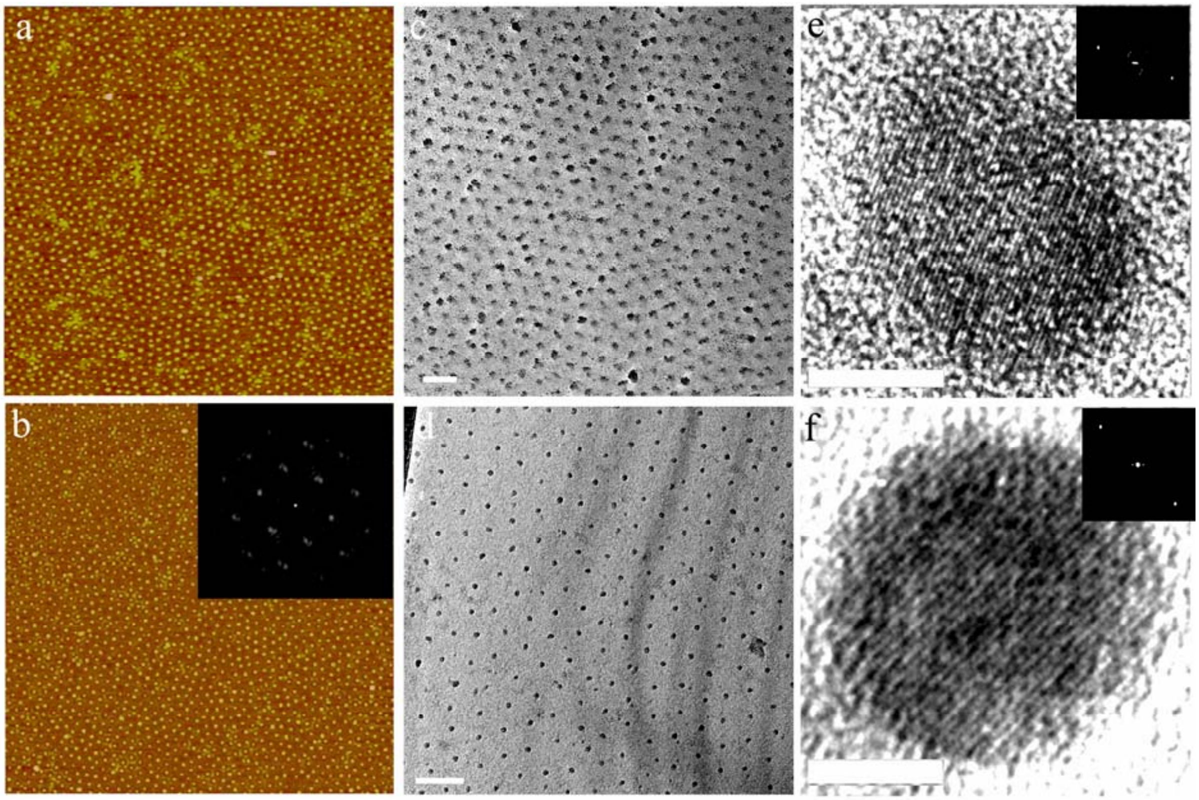

Figure 4.3: Structural Characterization of Ga_2O_3 and GaN nanocrystals. a AFM height image (2.5 × 2.5 μm^2) of Ga_2O_3 nanoparticles on Si substrate obtained after O_2 plasma treatment. b, AFM height image (2.5 × 2.5 μm^2) of GaN nanoparticles on Si substrate obtained after N_2 plasma treatment. Inset is a Fourier transform showing ordered arrangement of nanoparticles along a hexagonal lattice. TEM images of GaN nanoparticles on Si substrate (c) obtained by ammonia treatment of Ga_2O_3 nanoparticles at 650 ºC (scale bar 150 nm) (d) obtained by N_2 plasma treatment followed by annealing in ammonia gas at 700 ºC (scale bar 100 nm). High resolution TEM images of corresponding GaN nanoparticles synthesized are shown in e, and d, respectively (e-scale bar 3 nm; f scale bar-2 nm).

Thus, the TEM data not only revealed the crystalline nature of nitride nanoparticles, but also indicated that the periodicity and the arrangement of nanocrystals are unaffected at higher growth temperatures. Synthesis of amorphous GaN by thermal decomposition of cyclotrigallazane directly within the polymer matrices had been previously reported.[12] In those reports, decomposition temperatures of cyclotrigallazane were limited to low temperature (180°C), as the entire synthesis was performed in the polymer matrices, which only resulted in the formation of amorphous GaN.[21] Here, the removal of polymeric template after initial processing steps enabled us to employ higher reaction temperatures with ammonia resulting in crystalline GaN nanoparticles.

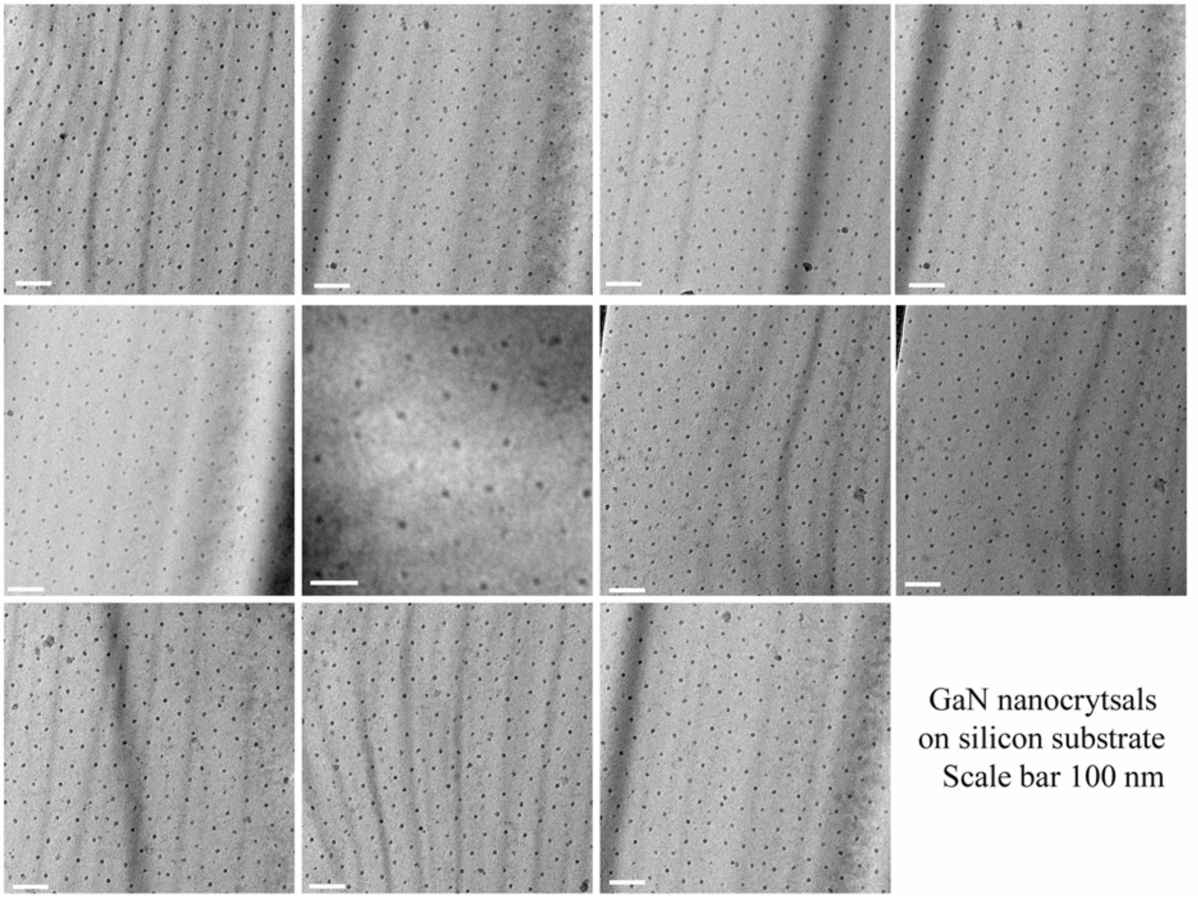

Figure 4.3B: Additional TEM images of GaN nanocrystals on Si substrate from a sample prepared using method III, obtained from different areas in the same sample confirmed monodispersity in their size and the periodicity, all scale bars are 100 nm in length.

4.4.3 X-Ray Diffraction (XRD) analysis of GaN NCs

The crystal structure of GaN nanocrystals synthesized using methods described above was ascertained using XRD analysis. Figure 4.4 shows the XRD patterns measured in the 2θ range of 20°-80° from multi-layered GaN samples synthesized in the temperature range of 600-800 °C. The fractional area occupied by GaN nanoparticles on the substrates was low (fractional area was ~ 4×10^{-4} % for a particle density of $\sim10^{11}/\ \mathrm{cm}^2$ on the substrate and with an average diameter of 5 nm) and, hence, a high background signal from the substrate was observed in the diffraction patterns. Broad diffraction peaks are a characteristic in the spectra obtained from crystalline nanomaterials; however, here the diffraction peaks in the XRD patterns obtained form different nanocrystals samples are sharp as they were collected from samples with a multilayer of nanoparticles. The diffraction peak at 44.5° in all the samples might have risen from the impurities in the metal and polymer precursors. A spectrum from the blank substrate is also shown in the same figure for comparison. XRD patterns collected from GaN samples synthesized at temperatures in the range of 600 °C to 750 °C exhibited evolution of spectra from broad to fine peaks with increasing temperature, suggesting improvement in the crystallinity. The XRD peaks of sample synthesized at 750 °C are in agreement with the diffraction peaks from wurtzite bulk GaN (JCPDS card number: 50-0792), indicating a wurtzite crystal structure for a majority of these GaN nanoparticles. Diffraction peaks corresponding to bulk GaN with wurtzite structure also provided in fig 4.4.

Interestingly, the crystal structure of GaN nanoparticles found in these investigations, particularly those prepared at higher temperatures (> 700 °C), was different from a majority of earlier reports based on the colloidal synthesis at low temperatures (below 500 °C), wherein a zinc blende crystal structure was reported.[24] Here, the origin of the wurtzite crystal structure for GaN NPs synthesized at temperatures exceeding 700 °C could be attributed to: (1) high temperature annealing treatments in ammonia flow that resulted in the formation of wurtzite crystal structure; and (2) effect of underlying lattice mismatched Si (100) substrate may also have influenced the final crystal structure of the NPs-this argument is based on the minimization of the total energy associated with the system that includes surface energies of GaN nanocrystals and Si substrate as well as the energy associated with Ga-Si interface. Regardless of its origin, wurtzite crystal structure has interesting consequences on the optical properties of III-nitrides due to built-in electric fields. This effect is discussed further in section 4.4.9.

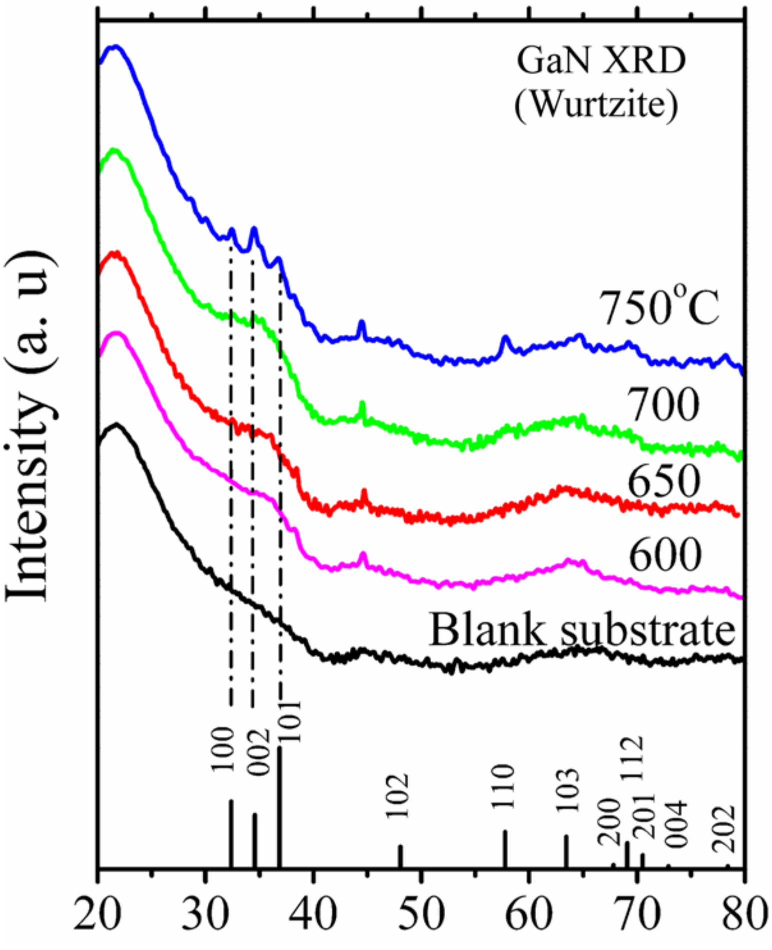

Figure 4.4: XRD spectra from multi-layered GaN nanoparticles on quartz substrates synthesized by ammonia CVD of Ga_2O_3 nanoparticles at different temperatures indicated wurtzite crystal structure, vertical dash lines demonstrate the peaks from the sample match the diffraction peaks from (100), (002) and (101) planes of wurtzite crystal structure. The diffraction peaks corresponding to bulk GaN (JCPDS card number: 50-0792) are also provided for reference.

4.4.4 Chemical Characterization: X-ray photoelectron spectroscopy (XPS)

The chemical states of the nanoparticles prior to and after the nitride growth of gallium oxide nanoparticles were determined using XPS analysis. Figure 4.5 displays high resolution spectra of Ga-2p$_{3/2}$ and Ga-3d$_{5/2}$ peaks, respectively, from the sample before and after nitride growth at 650 °C, using method 1. The presence of Ga-2p and Ga-3d peaks at 1119.5 eV and 20.8 eV, respectively, for the sample after oxygen plasma treatment, indicated that Ga was present in the form of Ga_2O_3.[36-37] Following ammonia treatment, the corresponding Ga peaks are present at 1118.2 eV and 19.6 eV, indicating the formation of nitride.[38-39] The lowering of binding energy for the Ga-2p and Ga-3d peaks, in the case of Ga-N type bonding as compared to the Ga-O bonding, were consistent with the lower electronegativity of nitrogen compared to that of oxygen. Ga-2p and Ga-3d peak shifts from Ga-O to Ga-N type bonding were 1.3 eV and 1.2 eV, respectively, and these shifts in the binding energy are also in close agreement with a previous report.[40]

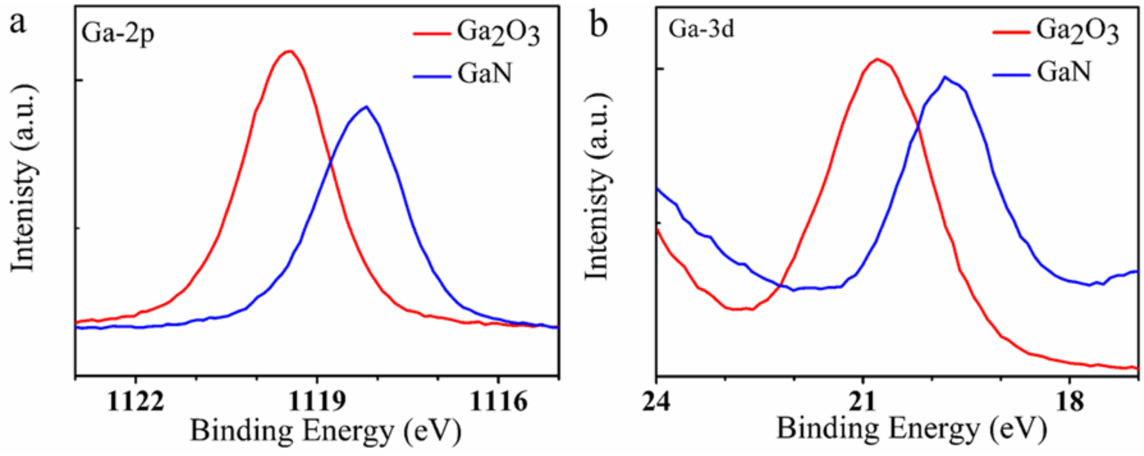

Figure 4.5: XPS data revealed the chemical state of nanoparticles, prior to, and after nitride growth of Ga_2O_3 nanoparticles.

4.4.5 GaN nanowires

Interestingly, ammonia treatment of Ga_2O_3 nanoparticles at temperatures exceeding 750 °C resulted in the formation of nanowires along with a decrease in the density of nanoparticles (fig.4.6a), suggesting that Ga_2O_3 nanoparticles acted as self-catalysts for the growth of GaN nanowires. This hypothesis was further confirmed by growing the nitride nanowires from Ga_2O_3 nanoparticles in the presence of an additional source of Ga (GaAc precursor on a Si substrate, which was placed upstream at a distance of 20 cm away from the Ga_2O_3 nanoparticles containing substrate). Usage of an additional Ga source resulted in the observation of a higher density of nanowires (fig.4.6b). It is likely that the nanowire growth in this experiment occurs via a vapor-liquid-solid method (VLS) that is the dominant mechanism in the case of catalytic- assisted nanowire growth in a CVD setup. At high reaction temperatures, under reducing atmosphere (H_2 gas), the Ga_2O_3 nanoparticles are reduced and are likely to be present in their liquid state as tiny droplets, which adhere on to the substrate surface due to surface tension. Decomposition of ammonia takes place on these liquid droplets and as the amount of nitrogen supersedes the supersaturation limit, GaN precipitates in the form of a nanowire. In the absence of additional source of Ga precursor, gallium is presumably provided by the nanoparticles that are present on the surface and hence a decrease in the density of nanoparticles was observed, while in the other case, presence of extra Ga source enabled growth of more nanowires, and hence a higher density of nanowire growth was observed.

This result in conjunction with the previous results indicated that treatment of Ga_2O_3 nanoparticles with ammonia could be tailored to achieve either GaN nanocrystals in the temperature range 600-750 °C or GaN nanowires in the presence of an additional source of Ga at temperatures exceeding 750 °C.

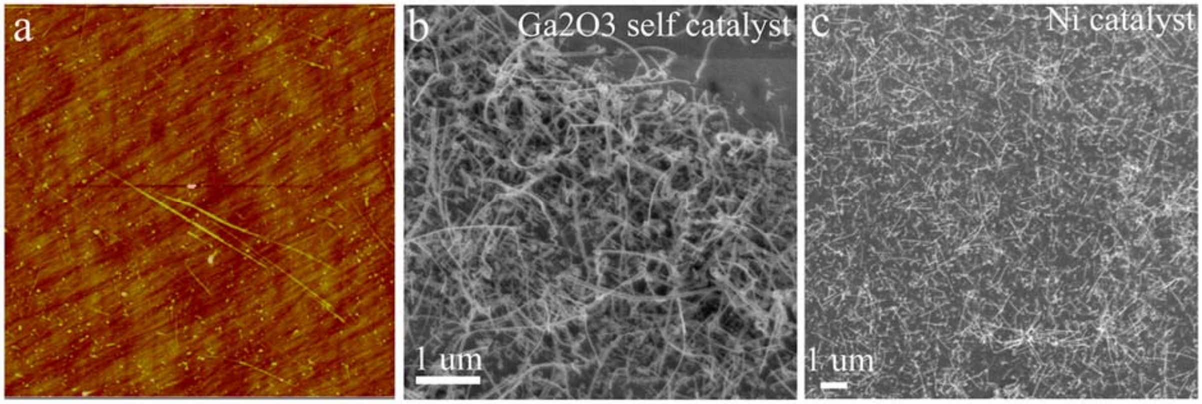

Figure 4.6: AFM and SEM data revealed self-catalyzing role of Ga_2O_3 nanoparticles for the growth of GaN nanowires using ammonia CVD. (b) GaN nanowires with uniform diameters grown from Ni catalysts in CVD process.

Thin films of Ni with thicknesses around 5 nm, have been traditionally used to catalyze GaN nanowires growth, in a MOCVD or a ammonia-CVD setup. In these investigations, thin films were heated to high temperatures to form clusters that were used to catalyze nanowire growth in the presence of relevant precursors at reaction temperatures.[3a] Since, the heated thin films usually yielded catalysts with a wide size distribution, hence, the nanowires that were grown from them also had a wide diameter distribution. Nonetheless, these studies provided nanoscale GaN material that was previously unavailable for investigating their optical properties. Herein, monodisperse arrays of Ni nanoparticles with an average size of 1.9 ± 0.3 nm (described in Chapter 3) were used to catalyze GaN nanowires growth using ammonia CVD. SEM analysis indicated high catalytic activity of Ni nanoparticles for GaN nanowire growth and these are first reports on synthesis of very small diameter GaN nanowires. The photoluminescence properties of these nanowires are discussed in next section. While investigations on these small diameter nanowires were not pursued further in this study, they nonetheless offer an exciting prospect. Interestingly, heterostructures of GaN nanowires can be grown by controlling their growth of these nanowires to result in confinement in both radial and longitudinal directions.

4.4.6 InN nanocrystals: Brief introduction, Synthesis and Characterization

Unlike most other III-nitrides, InN has rather unique attributes that merits further introduction to this interesting material. In comparison to the rest of the III-nitrides, InN has the highest mobility and the highest saturation velocity making it a potential candidate for high speed and high frequency electronic applications.[8] On the other hand, unlike GaN and $In_xGa_{1-x}N$, InN has been observed to be a poor emitter.[41] Earlier investigations on the optical absorption of InN thin films were interpreted to be in consistent with the fundamental band gap of around 1.8-2.1 eV. This value for band gap had been widely accepted and had rather been used (read misused) for theoretically determining the band gap of $In_xGa_{1-x}N$ ternary compounds. Moreover, it is emphasized that despite extensive efforts, no light emission with a band gap of 2 eV had ever been reported in those early investigations. Recently, for InN grown on Si substrates, weak PL peaks corresponding with energies in the range of 1.8-2.1 eV have been observed.[9] Although InN possesses attractive properties, it had not received significant attention primarily due to difficulties associated with synthesizing high quality crystalline material. With recent progress in MOCVD, thin films of InN were synthesized which revealed strong PL emission with energies in the range 0.7-1.1 eV in the near IR region,[42] contrary to previous theoretical observations. The origin of these observed values in the PL data may also arise as a result of emission from deep level impurities (similar to yellow emission from GaN thin films) which had further complicated the evidence for narrow band gap in InN. The disparity in the values reported for the band gap of InN had augmented a debate that is yet to be resolved.

So much for the synthesis of bulk InN, synthesis of InN nanostructures presents even more technical challenges. A handful of investigations on the synthesis of InN nanostructures have been recently reported with little or no control over the size of nanoparticles. Synthesis of monodisperse InN nanoparticles is paramount to unravel their fundamental physical properties. To this end, concerted efforts had been directed in this work to first synthesize uniform arrays of InN nanocrystals using the BCP template based approach, described previously for GaN NCs.

In short, Indium acetyl acetonoate precursor was loaded in the polymer micelles and the micellar solution was spin coated on silicon substrates. Subsequently, nitrogen plasma was used to remove the polymer shell that also resulted in the formation of InN nanoparticles. Finally, the nitride nanoparticles containing substrates were annealed in ammonia gas in the temperature range of 500-750 °C to further improve their crystallinity and it was observed that the temperatures below 600 °C yielded good results.

A representative AFM image of In-N nanocrystals after N_2 plasma treatment is shown in fig. 4.7a. Subsequently, XRD patterns were collected from all these samples to ascertain the chemical nature as well their crystal structure. It was observed that annealing in the temperature range of 500-600 °C yielded InN nanocrystals with wurtzite structure (fig. 4.8). Surprisingly, at temperatures exceeding 600 °C, a mixture of In_2O_3 and InN nanoparticles were observed. The contamination of oxygen in these samples might have risen from the In precursor loading in the polymer micelles. Oxygen may have been absorbed in the micelles in trace amounts that resulted in the formation of In_2O_3 at higher annealing temperatures. Oxygen diffusion from air into PTFE tubes that were used to carry gases into the furnace may also have been a source. Finally, oxygen from the quartz tubes as well as the underlying SiO_2/Si substrates that were employed in all these experiments may have contributed to In_2O_3 a formation. It should be noted that In_2O_3 is more stable than InN at temperatures exceeding 600 °C[26] and subject to the presence of trace amounts of oxygen in the system; it is likely to result in the formation of oxide. In the syntheses experiments that followed, trace amounts of oxygen were removed by flowing a reducing gas, such as H_2, while the heating the samples to the appropriate reaction temperatures, as well as while cooling the samples after annealing treatment. A TEM image of InN nanocrystals on a silicon substrate, annealed at 550 °C for 30 minutes, after nitrogen plasma treatment, is shown in fig 4.7b. TEM data, in conjunction with the XRD results, confirmed the synthesis of InN nanocrystals.

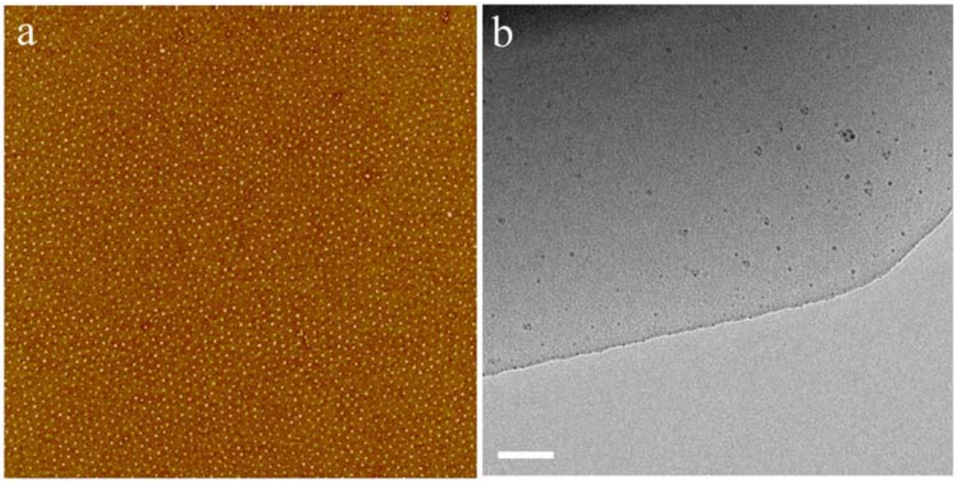

Figure 4.7: (a) An AFM image of In-N nanocrystals after nitrogen plasma treatment. (b) TEM image of annealed InN nanocrystals on Si substrate, scale bar- 50 nm.

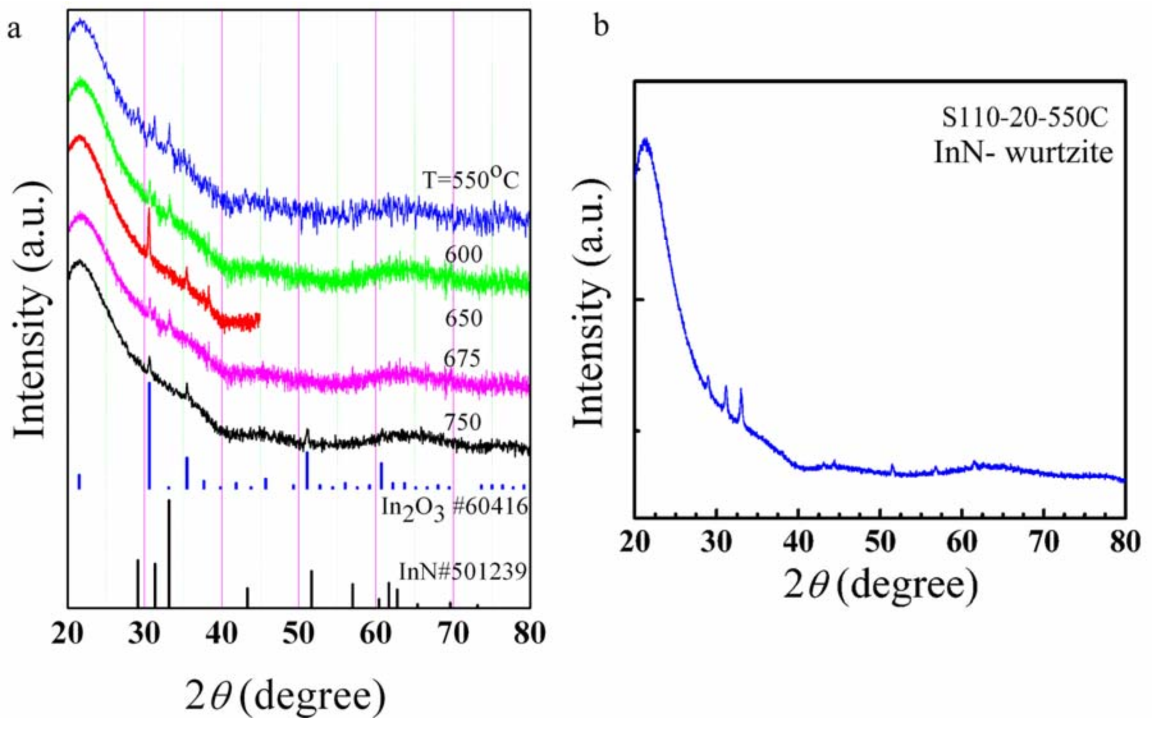

Figure 4.8: (a) XRD spectra from multi layer of nanoparticles that were annealed at different temperatures after nitrogen plasma treatment. Diffraction peaks corresponding to bulk InN and In_2O_3 are also shown below. (b) XRD spectra from a multi-layer of InN nanocrystals on a quartz substrate indicated wurtzite crystal structure for InN nanocrystals (annealed at 550 °C).

4.4.8 **Optical Characterization: Photoluminescence (PL) investigations**

A brief introduction to the characterization of optical properties of semiconductor nanocrystals as well as the rationale for conducting PL measurements in this work is described in this paragraph. Readers conversant with these fundamentals can skip and proceed to the next subsection.

Optical properties of semiconductor nanocrystals span a wide range of phenomenon, and also aid in understanding their basic fundamental physical properties. The optical properties can be divided into electronic and lattice properties- the former is concerned with processes involving the electronic states in the NC, while the latter deals with vibration of the lattice, involving creation and absorption of phonons. Though the latter property is more prominently observed in bulk crystalline materials, it could be present in NCs as well. Here, experiments were restricted to optical-electrical properties alone. A number of distinct optical electronic processes take place independently in the system that, include absorption and luminescence (photo-luminescence and electro-luminescence). The phenomenon related to fundamental absorption (see fig. 4.9) in a one step process involves the transition of electron from the valence band to the conduction band, upon absorption of an incident photon. This is usually the case with direct band gap materials, including III-nitrides, wherein the maximum and the minimum of the valence and conduction bands lie at the same value of the wave vector (k=0). Thus, experiments involving absorption studies of III-nitrides provide the band gap of the nanoscale material. On the other hand, luminescence refers to the exactly opposite process, wherein an electron that is present in the excited state decays into lower energy state by emitting a photon in the process, if the excitation is accomplished by electric current- it is referred to as electroluminescence and if it is accomplished by optical absorption- it is referred to as photoluminescence. Many physical processes are related to photoluminescence; however process related to transition from conduction band edge to valence band edge is more prominent, which also provides information on the band gap of the nanocrystal. In essence, both absorption and photoluminescence provide information on the band gap of the NC, however, the intensity that is obtained in the measurements is likely to be different and depends on the materials, substrates and the physical processes that are involved, and hence it might be easier to measure one better than the other.

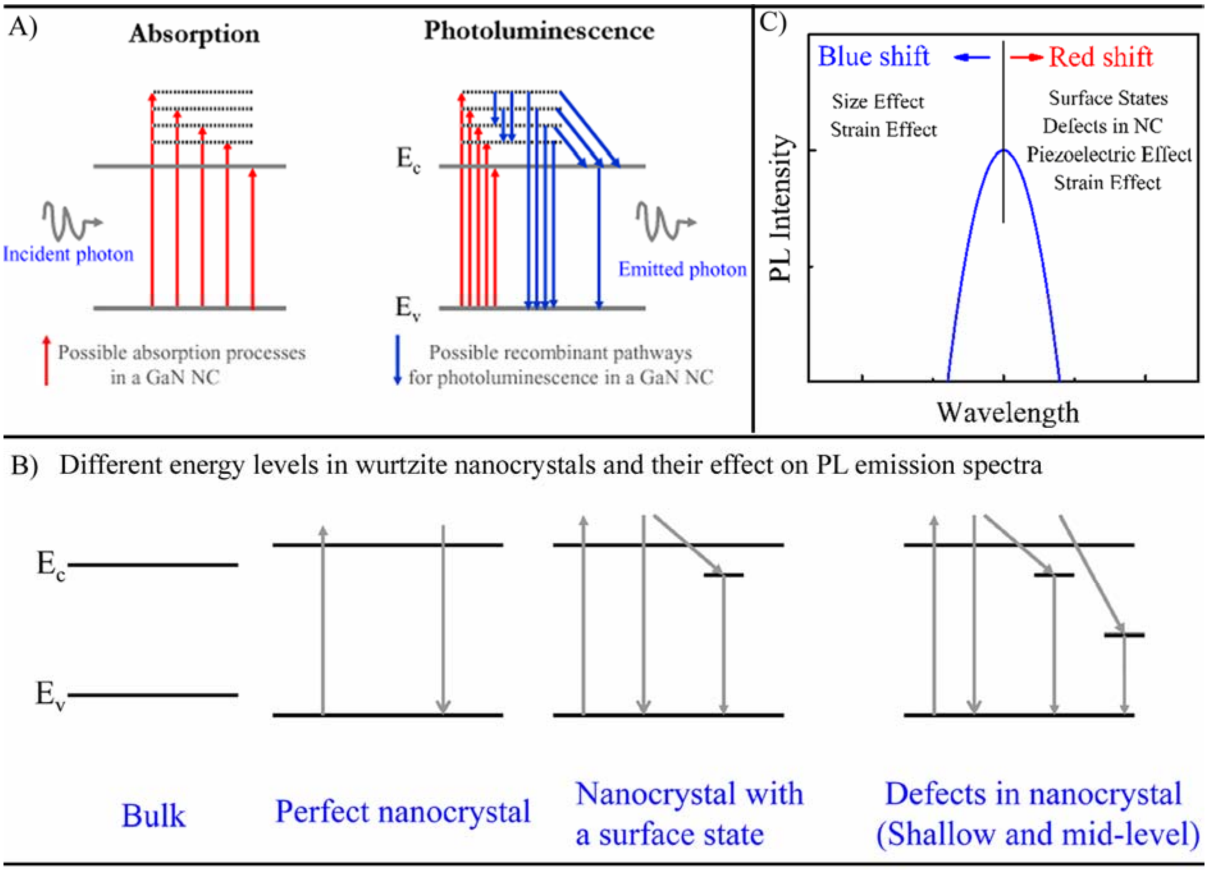

Figure 4.9: Schematic showing the various factors that affect the PL spectra of III-nitride nanocrystals. (a) Energy levels in the NCs that arise as a result of surface states and defects in the NCs and possible pathways for emission (b) schematic summarizing the affect of parameters that could either lead to red or blue shift in their PL spectra.

Absorption spectra from a single layer of nanocrystals on substrates is very low, and with a typical fractional area occupancy of 5%, the results in typical absorptions are ~1 × 10^{-4}, which are experimentally difficult to measure and such measurements require highly stable optical system and integration times of few hours, if not more. On the other hand PL and EL are standard characterization techniques that allow the emission energy of the dots to be determined. With low power densities, only emission from the lowest energy transition is observed, but by increasing the incident power, the ground state (degeneracy two) becomes fully occupied and the higher excited states also are partially or completely occupied from which recombination may occur.

4.4.7.1 PL data of GaN nanocrystals and nanowires

Photoluminescence spectral data of GaN nanoparticles on Si substrates were collected at room temperature, excited by a monochromatic source, with an excitation energy of 4.77 eV (260 nm) obtained from a Xenon lamp using Horiba Jobin Yvon spectrophotometer (Nanolog). The PL spectrum (fig. 4.10) from GaN NCs synthesized using method 2 at 750 °C exhibited a broad peak centered at 370 nm (3.35 eV) and a small, narrow peak at 330 nm (3.75 eV). The small peak at 330 nm (3.75 eV), with a full width at half maximum (FWHM) about 330 meV, demonstrated a blue-shift in the emission photon energy of nanoparticles compared to the band gap of bulk GaN (Wurtzite: 3.4 eV; Zinc Blende: 3.2-3.3 eV),[14] indicating that the emission peak resulted from the quantum confined states in GaN nanoparticles. Quantum confinement occurs when the radius of the nanocrystal, r, becomes comparable to the bulk exciton radius, $r_B = (h/2\pi)^2 \epsilon/\mu e^2$, where μ is the exciton reduced mass and ϵ is the dielectric constant of GaN. The simplest model for the electronic structure of nanocrystal involves a particle in a sphere model where the carriers are confined to a potential that becomes infinite at the interface. This set of boundary conditions for the nanocrystal leads to discrete instead continuous molecular orbitals. The quantization in electron and hole wavelengths translates to quantized energy levels with the energy of the first excited state of the electron or hole shifted by

$$\mathbf{E = h^2/8m_{eff}r^2}$$

from their bulk counterparts; m_{eff} is the effective mass of electron or hole and r is the radius of the nanocrystal. The corresponding energy shifts and the nanocrystal band gap increase with decrease size, as $1/r^2$, and constitute the origin of blue-shift in their PL emission spectra. Optical properties, including photo absorption and PL, of GaN nanocrystals strongly depend on the ratio of the nanocrystal radius to the Bohr-excition radius. Here, the GaN nanocrystal radii (1.5-5 nm) were comparable to the Bohr-excition radius (2-10 nm)[14-15] and hence the confinement was expected to be in the intermediate regime. It should be noted that the model discussed above is a simplistic one, and does not take into account the Coulombic interaction between the photo-generated electron and hole which are present in the same volume. This interaction also influences the PL spectra[3] of the GaN nanocrystals. The Coulombic interaction energy between the hole and the electron is of the order $e^2/\epsilon r$. Since the quantization energy scales as $1/r^2$, and the Coulombic energy scales as $1/r$, the latter contributes only a small correction to the quantized energies of electrons and holes for GaN nanocrystals with smaller sizes (< 10 nm), and hence, its affect on the system described here is relatively small and could presumably be neglected. However, for bigger GaN nanocrystals, the coulomb interaction energy becomes more important and it should be accounted for in these calculations. Also, the total power of the Xenon lamp was around ~500 W, which translates to low power densities in the energy region of interest and, hence, lower energy transitions could alone be expected. While quantum confined effects play a crucial role, the PL spectra of GaN nanocrystals here are affected by other factors, including surface states and strain effects.

---

[3] All reported PL spectra and pertinent discussions in this chapter correspond to PL emission

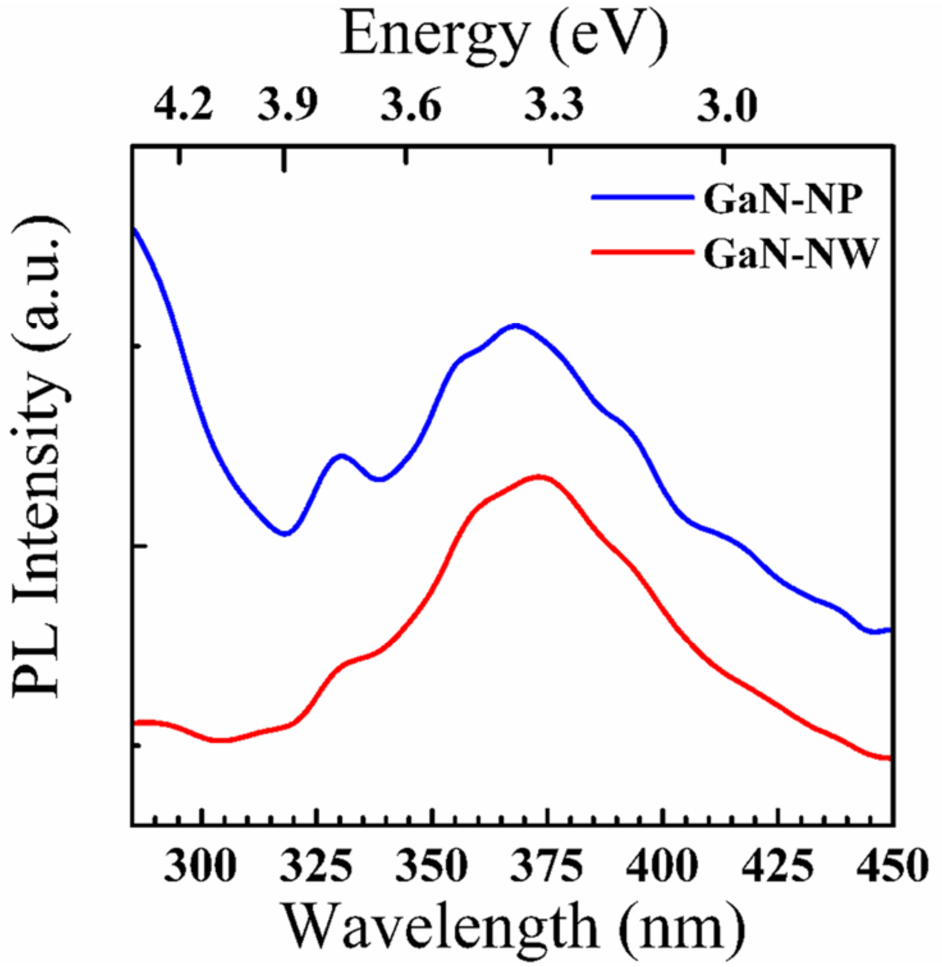

Figure 4.10: (a) Room temperature PL spectrum of GaN nanocrytsals on Si substrate synthesized using method 2 at 650 ºC (b) Room temperature PL spectrum of GaN nanowires on Si substrate synthesized at 750 ºC using Ga_2O_3 nanoparticles as self catalysts.

Similarly, a weak blue-shifted emission peak at 329 nm (3.769 eV) was observed in a PL spectrum of GaN nanowires (fig. 4. 10), again a result of the quantum confinement effects. The emission peak from quantum confined states in the NCs is weak, as the PL measurements were conducted at room temperature and repeating these experiments at a lower temperature (say, 5 K) could significantly enhance the signal.

The origin of the broad spectral peak at 370 nm in the spectrum obtained from GaN crystals (fig. 4. 10) could be attributed to a combination of the factors, including (1) surface states; (2)

defects in the NCs; (3) piezoelectric effects associated with the wurtzite crystal structure and (4) strain affects associated at the interface between GaN NCs and the Si substrate (see the schematic in fig. 4.9 b). Incidentally, most of these factors usually lead to red-shift in the PL spectra except for strain effects that could give consequently lead to either a red-shift or a blue-shift in the PL emission spectra (see the schematic in fig. 4.9 c).

(1) **Surface states**: Intermediate energy levels are observed in the band gap of the material as result of surface states, which are a consequence of unsatisfied bonds (dangling bonds) at the surface of the material. For nanocrystals, 90% of the atoms are at the surface and hence, affects associated with surface states are quite pronounced in nanostructures and, at times, they could supersede the quantum confinement effects. The presence of surface states provides additional pathways for recombination, consequently giving rise to a red-shift in their PL spectrum.

(2) **Defects in NCs**: Presence of defects in the GaN nanocrystals, result in the appearance of energy levels in the band gap of GaN, as a consequence, the presence of these energy states can result in red-shift in their PL spectra by providing additional recombination sites, similar to effects observed with surface states. For example, it is well known that presence of carbon based defects in GaN results in yellow emission.[43] Similarly, oxygen based defects are also prominently observed in GaN that have been observed to have deleterious affects on the PL data, which include broadening of peaks and red-shift in their emission spectrum.

(3) **Piezoelectric effect**: Wurtzite structure is a non centrosymmetric, and, as a consequence, materials which possess this structure could theoretically exhibit piezoelectric effect. Under the influence of an external electric field, GaN with wurtzite crystal structure gives rise to a strain, consequently giving rise to a built-in electric field that eventually results in either a red-shift or a blue-shift in the PL spectra. Most investigations-to-date have reported a red

shift. A blue shift is observed only at higher excitation power densities.[5] Interestingly, a wurtzite crystal structure was observed for a majority of GaN nanocrystals reported in this work, unlike those reported earlier, wherein a cubic zinc blende structure was observed. The contribution from this factor is likely to be higher compared to previous reports.

(4) **Strain effects**: The system described herein, wherein the GaN NCs are present on a Si substrate, is unlike most other reports on the synthesis of colloidal nanoparticles. After annealing nanocrystals samples in ammonia at high temperatures, strain associated with a difference in the lattice parameters of wurtzite GaN NC (wurtzite bulk GaN: a= 3.189 °A; c= 3.548 °A; see appendix I for more details) and the Si substrate (a=5.430 °A) could also give rise to a built-in electric field, again, a consequence of piezoelectric effect.

The total polarization in the system (GaN NCs and Si substrate) as a result of the latter two affects described above, is governed by the Maxwell equation,

$$\boldsymbol{\nabla \bullet} [\boldsymbol{\varepsilon_r E + P}] = \boldsymbol{\nabla \bullet} [\boldsymbol{\varepsilon_r\ E + (P_{spontaneous} + P_{strain})}] = \mathbf{0};$$

where $\boldsymbol{\varepsilon_r}$ is the dielectric constant of the material, $\mathbf{E}$ is the applied electric field, $\mathbf{P_{spontaneous}}$ is the spontaneous polarization and $\mathbf{P_{strain}}$ is the combined polarization that arises as a result of affects described in (3) and (4) above.

In essence, interplay between the size, the piezoelectric and the strain effects define the PL emission spectra of nitrides with wurtzite crystal structure. In wurtzite based GaN system on a substrate that is affected by all the above factors it should be emphasized that the relative contribution is more significant in predicting the final PL spectrum. It is believed that the broad spectral in the PL spectra of GaN NCs peak, shown in fig 4.11, arose due to the absence of surface passivation of the nanocrystals (this effect stronger for smaller nanoparticles), otherwise, if oxygen or carbon based defects are present in significant proportion, yellow emission at around 500-550 nm would have been observed (see appendix 2).

As mentioned earlier, PL spectral data of GaN NCs with radii exceeding 5 nm had been previously reported. Although these investigations have resulted in progress towards further understanding the fundamental optical properties of GaN NCs, many of these studies were performed on samples with non-uniform crystallite size. In addition, the nanoparticles in many of these examinations were present as agglomerates making it difficult to interpret their optical properties. The PL studies performed in this study are different from these reports and also constitute towards a significant progress in GaN research. Here, PL spectra were collected from uniform arrays of discrete GaN nanocrystals on Si substrates (most of the earlier reports were collected from colloidal solutions, see references 14 and 17) with sizes in the range of 3-10 nm. Second, the nanocrystals here were not surface passivated that affected their PL spectra. However, this could be over come by depositing a very thin layer of higher band gap materials relative to GaN, such as Al_2O_3 or AlN, using either e-beam or RF sputtering, to passivate the surface of NCs.

In summary, GaN NCs with sizes in the range of 3-10 nm, synthesized by the PS-P4VP templates exhibited a blue-shift in their PL emission spectra, indicating that the emission resulted from the quantum confined states, though not without the complications introduced by surface states.

4.4.7.2 **Photoluminescence data of InN nanocrystals**

Photoluminescence spectra of InN nanocrystals were collected using two different excitation sources: Xenon lamp with an excitation wavelength ranging between 600-800 nm and a laser diode with an excitation wavelength of 650 nm and with a power of 2-4 mW. Room temperature PL spectra of wurtzite InN nanocrystals on fused silica and Si substrates under varying conditions are shown in fig. 4.11. All the spectra revealed a PL emission corresponding to ~1150 nm (1.08 eV).

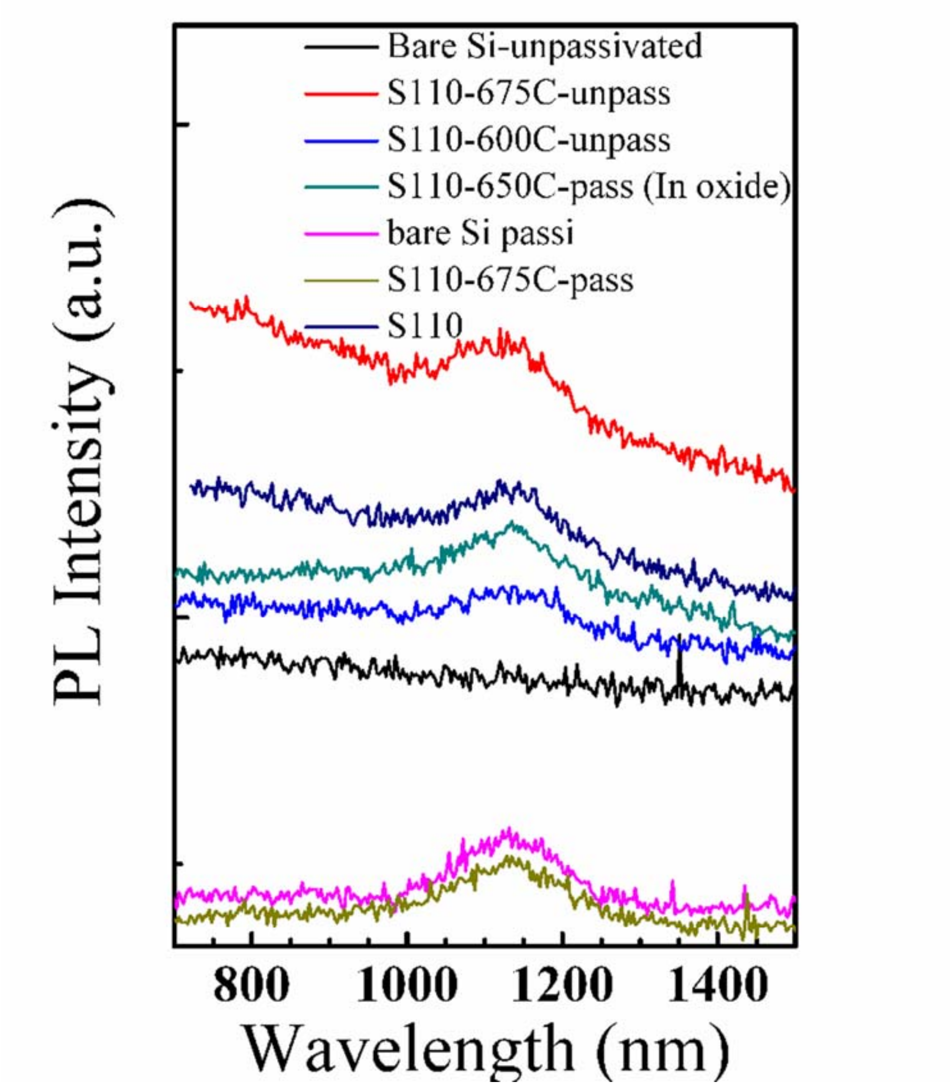

Figure 4.11 Room temperature PL spectra of InN nanocrystals on various substrates.

The emissions in these spectra might have resulted from (1) band-edge luminescence in InN nanocrystals (2) mid-level defects in InN (similar to yellow emission from defect levels in GaN) and (3) underlying substrate. The band gap of bulk wurtzite InN thin films on sapphire substrates has been previously reported to lie between 0.7-0.8 eV. The quantum confinement effects in InN nanostructures lead to a blue-shift in the photon emission energy and could consequently lead to a higher band gap (~ 1.1 eV), suggesting that the data reported herein corresponds to the band gap of InN. However, further investigations on the PL emission need to be performed to understand the role of defect levels in InN as well as the role of the underlying substrate to conclude on the actual value of band gap. Efforts are currently directed towards this end.

4.5 On-going research efforts and future directions: Ternary III-nitrides and transition metal doping in GaN

The di-block copolymer templating method not only enabled syntheses of monodisperse arrays of III-nitride nanocrystals, but also created a foundation for further exploring fundamental investigations on the syntheses and optical properties of ternary nitrides as well as transition metal doping in binary nitrides. While investigations to this end are still in their infancy, nonetheless, initial results are promising, and hold an exciting prospect for further studies. Herein, only results from initial experiments are discussed.

Exploring syntheses of ternary nitrides [for example: (Ga, In)-N] as well doping in GaN nanocrystals with transition metals is an interesting prospect for the following reasons:

(1) It is well known that GaN exhibits a PL emission in the UV region and InN is theoretically known to have a PL response in the IR region. Therefore, ternary compounds of Ga and In nitrides are theoretically predicted to have emission in the intermediate visible and near IR ranges, indicating that these materials could be potentially used to map opto-electronic applications that span the entire optical spectrum in the UV-IR regime;

(2) Doping transition metallic elements in binary nitrides, including rare earth elements, is indeed very appealing both from a fundamental physics perspective as well from a technological perspective:

(i) For example, GaN based materials have already been proven successful for the fabrication of blue and green light emitting devices (LEDs). Realization of red-LEDS has encountered difficulties associated primarily with their syntheses. While ternary compounds of Ga and In nitrides may provide one route for synthesis of materials with emission in the red region, an alternate exciting possibility is offered by rare earth dopants in GaN. Rare earth ions, including Eu and Gd, have unique optical properties, which exhibit sharp emission in the entire visible range (the emissions arise as result of intra shell transitions in these ions). Interestingly as well as importantly, these emissions are almost insensitive to host materials and temperature, which is in sharp contrast to inorganic nanostructures, including, quantum wells and quantum dots. By matching the energy levels in GaN nanocrystals with the energy levels in dopant ions, it may be possible to improve the energy transfer, consequently giving rise to stronger emission from the dopant ions.[46] Thus, by combining the electronic properties of GaN and optical properties of rare-earth ions it may be possible to envision new physical properties as well nanotechnology applications;

(ii) In a similar way, combining the magnetic properties of transition metal dopants and the electronic properties of GaN offers promise for spintronics.

Few investigations exploring the above ideas in GaN thin films/micro-structures have already been reported.[44-46] Similar studies in nanostructures, including nanocrystals, are currently, a fast emerging field.

4.5.1 Ternary Nitrides: Initial results and discussion

Ternary compounds of Ga-In-N were prepared as outlined in fig. 4.12. Synthesis of ternary compounds is intricate due to the fact that simultaneous loading of multiple metal ions into the core of the micelles could result in either micelles being loaded with only one type of metal ions or inhomogeneous loading of metal ions in different micelles, consequently giving rise to erroneous results. Therefore, to avoid discrepancies, different metal precursors were sequentially loaded into the polymer micelles one after the other. Usually, the time period between the additions of various precursors was around 6-8 hours. Although, the metal loads were loaded sequentially, we are still unsure if that would result in uniform loading of micelles with the same composition. This is one of the current biggest challenges associated with the synthesis of both binary compounds as well as doping in binary nitrides using the BCP method. Moreover, it was rather difficult to determine the composition of nanoparticles using either chemical or structural characterization techniques. Structural characterizations of these nanoparticles were conducted using AFM and TEM. Figure 4.13 shows representative AFM images of binary nitrides of Ga and In (sample S108: Ga: In = 0.85:0.15; sample S109: Ga:In = 0.15: 0.85; note that these compositional values correspond to the amount of precursors that were initially loaded in the micelles).

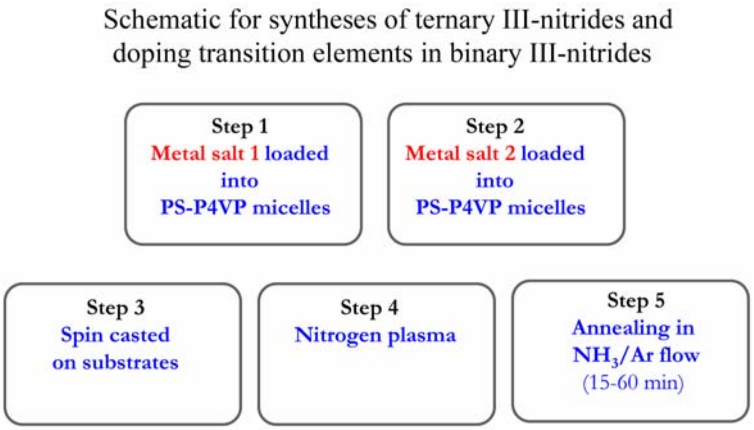

Figure 4.12: Schematic outlining the processing steps for synthesis of ternary nitrides as well as transition metals doping in binary nitrides.

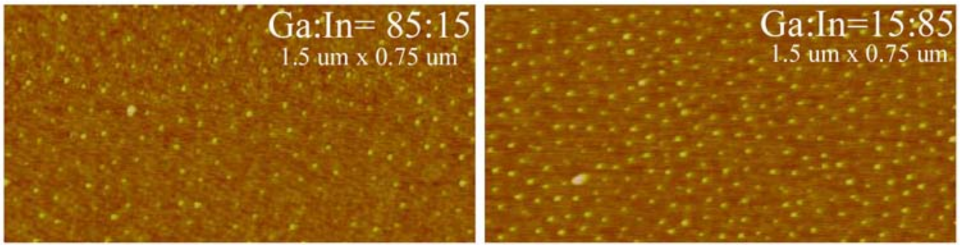

Figure 4.13: AFM images of ternary compounds of Ga and In nitrides with the following initial compositions (a) sample S108: Ga: In = 0.85:0.15 (b) sample S109: Ga:In = 0.15: 0.85

Although these techniques provided important data on the size and crystallinity of the nanoparticles, neither of these techniques could be used to reveal the composition of the nanoparticles. Chemical characterization using XPS was employed to determine if both the elements were present or not in these nanoparticles. The XPS survey results shown in fig 4.14 indicated that both the Ga and In were present on the sample, however, these results did not indicate that individual nanoparticles comprised of both these elements. It is emphasized that XPS is a surface characterization technique that gives results based on data collected from an ensemble of nanoparticles. An alternate way to determine the composition is by investigating a physical property of one of the elements that is affected in the presence of the other element. For example, pure GaN emits in the UV region and in the presence of In, a red-shift in the PL spectra is theoretically expected. Again, it is emphasized that the PL spectrum obtained from the sample is based on information collected from an ensemble of nanoparticles.

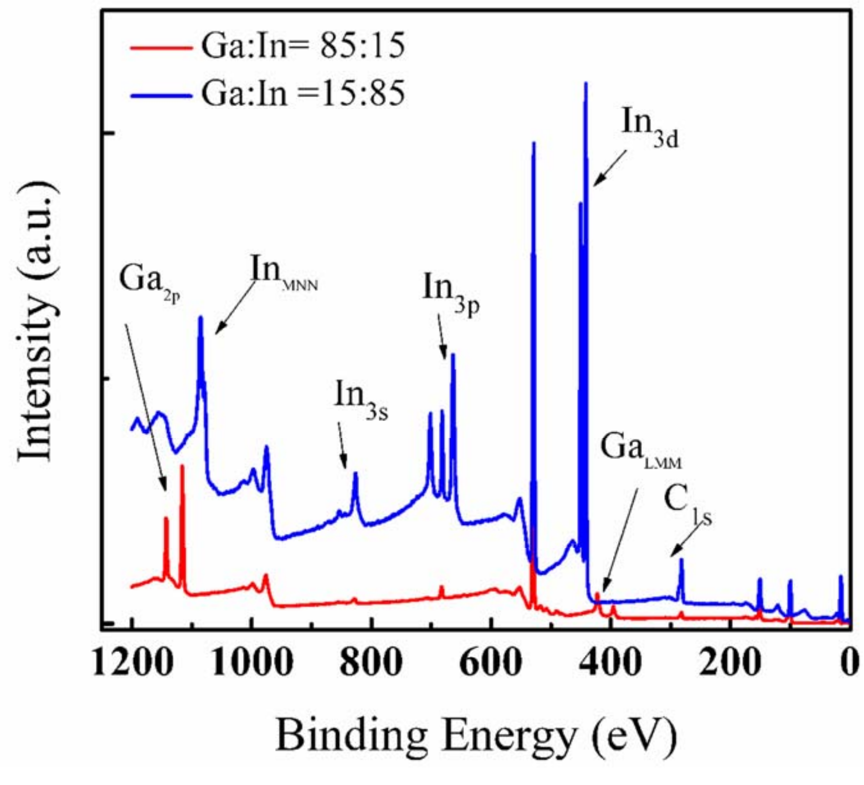

Figure 4.14 XPS surveys of Ga-In-N nanoparticles on Si substrate.

4.5.2 Doping transition metal ions in GaN nanocrystals

Manganese and Europium doped GaN samples (1% dopant level) were prepared by first sequentially loading the corresponding metal precursors into the PS-P4VP micelles. The polymeric solutions were spin-casted on substrates and subsequently nitrogen plasma treated to remove the polymeric shell and further annealed in ammonia to improve the crystallinity. Initial results, including chemical and the structural characterizations of GaN nanocrystals (sample S125), Mn nanocrystals (chemical state was not determined; sample S127) and transition metals doped GaN nanocrystals (S126) are displayed in figures 4.14 and 4.15.

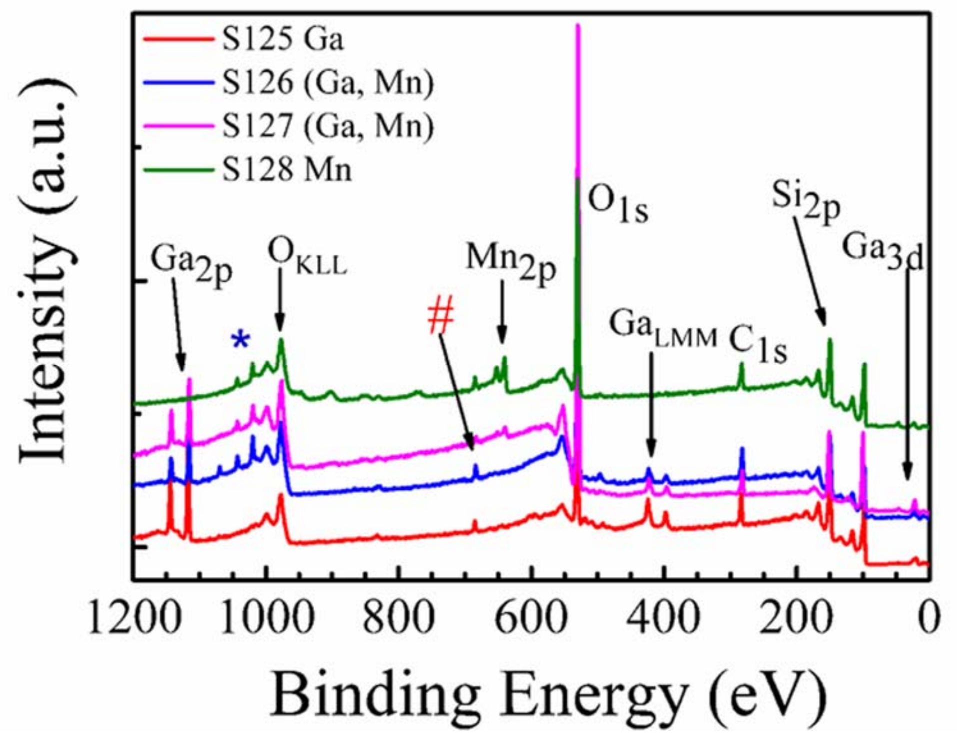

Figure 4.14: XPS surveys from different binary nanocrystals (S125-Ga; S128-Mn) and Mn doped GaN nanocrystals (S126 and S127) after nitrogen plasma treatment.

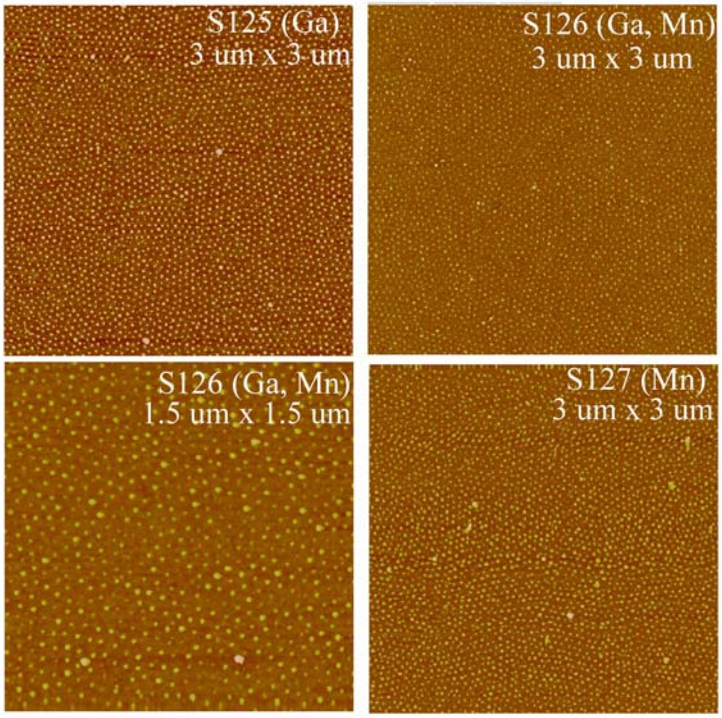

Figure 4.15: AFM images of (a) GaN (b and c) Mn doped GaN and (d) Mn nanocrystals. Note: The oxidation state of Mn was not determined in sample S127.

4.5 Summary

Synthesis of III-nitrides nanostructures

III-Nitrides, including those based on AlN, GaN and InN have received immense attention over the past decade as potential materials with successful opto-electronic applications. Current efforts are focused on synthesis and on understanding the physical properties of their nanostructures. Amongst III-nitrides, GaN has been the one that had been widely investigated and similar studies on AlN and InN have been lacking, primarily due to difficulties associated with their syntheses. Investigations on the synthesis of GaN nanoparticles, including colloidal methods,[14] solvo-thermal methods,[16-17] detonation of gallium azide and cyclotrigallazanes,[18-21] metallo-organic chemical vapor deposition (MOCVD)[22] and molecular beam epitaxial methods[23] have been previously reported. However, in spite of significant progress in the synthesis of GaN nanoparticles using different methods, it is still a challenge to synthesize nanoparticles with controlled size and shape uniformity in the 1-5 nm size range. Moreover, in many syntheses methods the nanoparticles tend to agglomerate in the solutions, making it difficult to unambiguously study the optical properties from individual nanoparticles. Though techniques such as MOCVD and MBE offer good control over the size of the nanoparticles, these methods are limited by the need for lattice match substrates and are relatively more expensive processes. Moreover, to the best of our knowledge, we are unaware of investigations reporting synthesis of nanocrystals in the 1-5 nm regime based on either of the latter two methods.

A new combinatorial approach involving self-assembling block copolymer micellar templates and gas phase reactions to synthesize ordered arrays of III-nitrides nanocrystals, including those of GaN and InN, in the size range of 1-10 nm with controlled spacings between the nanoparticles was demonstrated. The standard deviations in the average sizes of nanocrystals were in the range of 9-

12%. Using the combinatorial approach, long standing problems associated with the syntheses of III-nitrides, in particular, distributions in the size of nanocrystals have been successfully overcome in these studies. In addition, syntheses of ternary compounds of Ga-In-N and doping of rare-earth ions such as Eu^{3+} and Mn^{2+} in GaN nanocrystals, with average sizes of 5 nm were also successfully conducted. While examinations on rare earth doping in GaN thin films have been previously reported, similar studies in nanostructures, including nanoparticles and nanowires are currently a fast emerging field. The combinatorial approach afore mentioned serves as a general method for syntheses of III-nitrides nanostructures.

Optical Properties of III-nitrides nanostructures

Quantum confinements of GaN nanocrystals (radii exceeding 5 nm) based on their PL emission spectra have been previously reported. Although these investigations have resulted in progress towards further understanding the fundamental optical properties of GaN NCs, many of these studies were performed on samples with non-uniform crystallite size. In addition, the nanoparticles in many of these examinations were present as agglomerates making it difficult to interpret their optical properties. The optical properties of III-nitrides, while an asset in their practical use, presented unique challenges in the scientific experiments. The PL studies performed in this study are different from these reports and also constitute towards a significant progress in GaN research. Here, PL spectra were collected from uniform arrays of discrete isolated GaN nanocrystals on Si substrates (most of the earlier reports were collected from colloidal solutions, see references 14 and 17) with sizes in the range of 1-10 nm**.** Unlike most other III-V compounds that exhibit Zinc blende structure, III-nitrides also exhibit wurtzite crystal structure that consequently leads to interesting optical properties. Most investigations to-date on GaN nanocrystals have reported structures that are either predominantly Zinc blende or a mixture of Zinc blende and wurtzite crystal structures. Here, as confirmed by the XRD patterns, both GaN and InN nanoparticles, predominantly exhibited a wurtzite crystal structure. The examinations on the optical properties of GaN clearly revealed a blue-shift in the photon emission energy that indicated that emissions arose from the quantum confined states in the nanocrystals. While experiments investigating the optical properties of InN nanocrystals suggested a band gap of ~1.1 eV, these results need to validated further. The emission might have arisen from the quantum confined states in InN or probably from the mid-level defects in InN (similar to yellow emission in GaN). Although ternary III-nitrides based on Ga and In as well as rare earth doped GaN nanocrystals were synthesized, examinations on their optical properties were not conducted. Initial results on their syntheses are promising and pave an exciting prospect for future studies on their physical properties (both optical and magnetic).

The discrete and isolated nanocrystals of various III-nitrides (GaN, InN, ternary nitrides, doped nitrides) synthesized in this work might enable single nanocrystal luminescence measurements (for example, blinking effects) that have so far eluded many researchers. Future examinations on the optical properties of these various III-nitride nanocrystals should include passivation of the nanocrystal's surface, as well as conducting the PL emission measurements at low temperatures (say 5-100 K).

References

[1] D. J. Eagleshman and M. Cerullo, Phys. Rev. Lett., **1990**, *64*, 1990, 1943.

[2] C. Murray, C. Kagan, M. Bawendi, Annu. Rev. Of Mater. Sci **2000**, *30*, 545-610.

[3] S. Lee, I. Daruka, C. S. Kim, A. L. Barabasi, J. L. Merz, J. K. Furdyna, *Phys. Rev. Lett.* **1998**, *81*, 3479.

[4] N. N. Ledentsov, V. M. Ustinov, V. A. Shchukin, P. S. Kopev, Z. I. Alferov, D. Bimberg, *Semiconductors* **1998**, *32*, 343.

[5] F. Widmann, J. Simon, B. Daudin, G. Feuillet, J. L. Rouviere, N. T. Pelekanos, Phys. Rev. B, 1998-II, 58 (24), R15989-92).

[6] K.Tachibana, T.Someya, Y. Arakawa, *Appl. Phys. Lett.* **1999**, *74*, 383.

[7] A.Petersson, A. Gustafsson, L. Samuelson, S. Tanaka, Y. Aoyagi, *Appl. Phys. Lett.* **1999**, *74*, 3513. GaN

[8] A. G. Bhuiyan, A. Hashimoto, A, Yamamoto, J. Appl. Phys., **2003**, *94*, 2779.

[9] T.Yodo, H. Yona, H. Ando, D. Nosei, Y. Harada, Appl. Phys. Lett., **2002**, *80*, 968.

[10] M. Pinczolits, G. Springholz, and G. Bauer, Appl. Phys. Lett., **1998**, *73*, 250

[11] F. A. Ponce, D. P. Bour, *Nature*, **1997**, *386*, 351-359.

[12] S. Nakamura, *Annu. Rev. Mater. Sci.*, **1998**, *28*, 125-152.

[13] (a) J. C. Johnson, H. C. Choi, K. P. Knutsen, R. D. Schaller, P. Yang, R. J. Saykally, *Nat. Mat.*, **2002**, *1*, 106-110. (b) Y. Hwang, X. Duan, Y. Cui, L. J. Lauhon, K. H. Kim, C. L. Lieber, *Science*, **2001**, *294*, 1313-1317.

[14] O. I. Micic, S. P. Ahrenkiel, D. Bertram, A. J. Nojik, *Appl. Phys. Lett.*, **1999**, *75* (4), 478-480.

[15] N. A. Preschilla, S. Major, N. Kumar, I. Samajdar, R. S. Srinivasa, *Appl. Phys. Lett.*, **2000**, *77* (12), 1861-1863.

[16] Y. Xie, Y. Qian, Y, W. Wang, S. Zhang, Y. Zhang, *Science*, **1996**, *272*, 1926-1927.

[17] (a) K. Sardar, C. N. Rao, *Adv. Mat.*, **2004**,*16*, 425-429.
(b) K. Sardar, M. Dan, B. Schwenzer and C.N.R. Rao, *J. Mater. Chem.*, **2005**, *15*, 2175.

[18] J. Hwang, J. P. Campbell, J. Kozubowski, S. A. Hanson, J. F. Evans, W. L. Gladfelter, *Chem. Mater.*, **1995**, *5*, 517-525.

[19] A. C. Frank, F. Stowasser, H. Sussek, H. Pritzkow, C. R. Miskys, O. Ambacher, M. Giersig, R. A. Fischer, *J. Am. Chem. Soc.*, **1998**, *120* (12), 3512-3513.

[20] (a) J. F. Janik, R. L. Wells, *Inorg. Chem.*, **1997**, *36*, 4135-4137.
(b) J. A. Jegier, S. McKernan, A. P. Purdy, W. L. Gladfelter, *Chem. Mater.*, **2000**, *12*, 1003-1010.

[21] V. J. Leppert, A. K. Murali, S. H. Risbud, M. Stender, P. P. Power, C. Nelson, P. Banerjee, A. M. Mayes, *Phil. Mag. B*, **2002**, *82*, 1047-1054.

[22] Y. Azuma, M. Shimada, K. Okuyama, *Chem. Vap. Depos.*, **2004**, *10*, No.1, 11-13.

[23] B. Daudin, F. Widmann, G. Feuillet, C. Adelmann, Y. Samson, M. Arlery, J. L. Rouviere, *Mater. Sci. and*

Engg. B: Sol. St. Mat. for Adv. Tech. , **1997**, *B 50* (1-3), 8-11.

[24] T. L. Tansley, C. P. Foley, *J. Appl. Phys.*, **1986**, *59* (9), 3241-3244.

[25] J. Wu, W. Walukiewicz, K. M. Yu, J. W. Ager III, E. E. Haller, H. Lu, W. J. Schaff, Y. Saito, Y. Nanishi, *Appl. Phys. Lett.*, **2002**, *80* (21), 3967-3969.

[26] B. Schwenzer, L. Loeffler, R. Seshaddri, S. Keller, F. F. Lange, S. P, DenBaars, U. K. Mishra, *J. Mat. Chem.*, **2004**, *14*, 637-641.

[27] M. Park, C. Harrison, P. M. Chaikin, R. A. Register, D. H. Adamson, *Science*, **1997**, *276*, 1401-1404.

[28] T. Thurn-Albrecht, J. Schotter, G. A. Kastle, N. Emley, T. Shibauchi, L. Krusin-Elbaum, K. Guarini, C. T. Black, M. T. Tuominen, T. P. Russel, *Nature*, **2000**, *15*, 2126-2129.

[29] M. Antonietti, E. Wenz, L. Bronstein, M. Seregina, *Adv. Mater.*, **1995**, *7* (12), 1000-1005.

[30] J. P. Spatz, S. Mossmer, C. Hartmann, M. Moller, *Langmuir*, **2000**, *16*, 407-415.

[31] R. Glass, M. Moller, J. P. Spatz, *Nanotechnology*, **2003**, *14*, 1153-1160.

[32] S. Bhaviripudi, A. Reina, J. Qi, J. Kong, A. M. Belcher, *Nanotechnology*, **2006**, *20*, 5080-5086.

[33] L. A. Belfiore, A. T. N. Pires, Y. Wang, H. Graham, E. Ueda, *Macromolecules*, **1992**, *25*, 1411-1419.

[34] W. C. Johnson, J. B. Parsons, M. C. Crew, *J. Phys. Chem.*, **1932**, 36, 2651-2654.

[35] R. C. Schoonmaker, C. E. Burton, *Inorg. Synth.*, **1963**, *7*, 16-18.

[36] J. F. Moulder, W. F. Stickle, P. E. Sobol, K. D. Bomben, K. D. *Handbook of X-ray Photoelectron Spectroscopy* (Perkin- Elmer, Minnesota, **1995**).

[37] R. Carli, C. L. Bianchi, *App. Surf. Sci.*, **1994**, *74*, 99-102.

[38] J. Hedman, N. Martensson, *Physica Scripta*, **1980**, *22*, 176-178.

[39] R. Carin, J. P. Deville, J. Werckman, *Surf. & Inter. Anal.*, **1990**, *16*, 65-69.

[40] S. D. Wolter, B. P. Luther, D. L. Waltemyer, C. Onneby, R. J. Molnar, *Appl. Phys. Lett.*, **1997**, *70* (16), 2156-2158.

[41] S. Nakamura, G. Fasol, Blue Laser diode, Springer, Berlin, **1997**.

[42] K. Xu, A. Yoshikawa, Appl. Phys. Lett., **2003**, *83*, 251.

[43] R. Singh, R. J. Molnar, M. S. Unlu and T. D. Moustakas, *Appl. Phys. Lett.* 1994, *64* (3), 336-339.

[44] K. Biswas; K. Sardar, C. N. R. Rao, Appl. Phys. Lett., **2006**, *89*, 132503 1- 3.

[45] A. Podhorodecki, M. Nyk, R. Kudrawiec, J. Misiewicz, W. Strek, Electrochemical and Solid-State Lett., **2007**, *10* (3), H88-H89.

[46] R. Kudrawiec, M. Nyk, A. Podhorodecki, J. Misiewicz, W. Strek, M. Wolcyrz, Appl. Phys. Lett., **2006**, *88*, 061916 1-3.

Chapter 5

Arrays of Mono- and Bi-metallic Nanoparticles as Catalysts for Controlled Growth of SWNTs

Abstract

One-dimensional nanoscale materials such as carbon nanotubes (CNTs)[1] offer great promise as components for next generation computing devices,[2,3] interconnect materials [4,5] and for field emission displays,[6,7] due to their excellent physical properties, which are primarily dependent on their diameter and their chirality.[8,9] Furthermore, the diameter of the nanotube largely depends on the size of the metal catalyst nanoparticle, from which it is grown in a CVD process.[10] Thus, to achieve uniform physical properties for CNTs it is critical to have a narrow size distribution of the catalyst nanoparticles. Efforts in this thesis have been aimed to address these current challenges in the field of nanotubes and the block copolymer method discussed earlier was a result of all the efforts laid towards the development of a method for synthesis of metal nanoparticles with uniform

size in the range of 1-5 nm. In this chapter, **first**, results pertaining to the diameter-controlled growth of single-walled nanotubes (SWNTs) from size-controlled mono-metallic catalysts (Fe, Co and Ni) using CVD are presented. As confirmed from the AFM and Raman analyses, the diameter distributions of SWNTs were in close agreement with the initial size distributions of the catalyst nanoparticles. **Second**, direct comparisons on the catalytic activities of metal nanoparticles for nanotube growth are discussed. These comparison studies provided valuable insight on the catalytic behavior of metal nanoparticles for nanotube growth, and, importantly, such investigations are being reported for the first time. **Third**, alternate ways to improve the yield of nanotubes, including those employing Fe-Mo bi-metallic catalysts are also being reported for the first time as well. **Fourth**, new catalyst materials for nanotube growth were explored. By far, the majority of work reporting CVD synthesis of carbon nanotubes in the literature has focused on thin films and nanoparticles catalysts based on Fe, Co, and Ni. Herein, the versatility of the BCP method enabled synthesis of various transition elements whose catalytic properties were evaluated for nanotube growth. While these studies are currently underway, first demonstration of SWNT growth by thermal CVD employing Au nanoparticles is presented. Eventually, this result might have important implication leading to low temperature synthesis of SWNTs. **Finally**, controlled growth of nanotubes in two different (horizontal and vertical) configurations to enable device integration is presented.

5.1 Introduction

An ever increasing demand for improving the performance of processor chips and memory devices has resulted in the miniaturization of transistors with channel lengths as low as 100 nm. Critical technological barriers and fundamental physical limitations associated with further size reduction of transistors have fueled a need for alternate materials and synthesis routes that could address these challenges. 1-D nanoscale materials such as carbon nanotubes and semiconducting nanowires offer great promise as components for the next generation computing devices and as interconnect materials due to their excellent electronic properties.

Single-walled carbon nanotubes (SWNTs) possess an appealing array of physical properties, which give them great potential for a growing number of technological applications (A brief introduction to SWNTs is provided in appendix IIIa). Importantly, the physical properties of SWNTs are dictated by their diameter and their chirality. Many techniques for the synthesis of nanotubes have been identified, including laser ablation, arc discharge method, catalyst-assisted chemical vapor deposition (CVD) method. To date, the most versatile techniques for synthesizing SWNTs have been those based on catalyst-assisted chemical vapor deposition. In a typical CVD experiment, hydrocarbon sources are reacted in the presence of metal nanoparticles (Fe, Co, Ni, etc) in a reaction tube typically at temperatures in the range of 800-1100 °C to synthesize nanotubes. In these techniques, metal-based nanoparticles serve as catalysts in both assisting carbon feedstock cracking/decomposition and facilitating the nucleation of nanotubes. Importantly, the size of the catalyst nanoparticle primarily defines the nanotube diameter. Thus, achieving uniform physical properties for CNTs at least entails using a narrow size distribution of catalyst particles grown on substrates. Understanding how to control the synthesis of SWNTs is also vital in order to deterministically integrate such nanostructures into various technologies. In every variation of the

CVD method used for synthesizing SWNTs, the composition and morphology of the catalyst nanoparticles are critical in determining the structure, length, and yield of nanotubes which will result.

Current Challenges and Present State of Research

Major challenges in the syntheses of SWNTs have been the problems at hand for many researchers, which include,

[1] Most nanotube synthesis techniques yield a (i) mixture of metallic and semiconducting nanotubes with a wide distribution in the diameters of nanotubes (ii) the nanotubes are present in the form of bundles;

[2] Controlled synthesis of SWNTs with uniform diameter and uniform physical properties;

[3] Controlled growth of nanotubes from pre-defined locations to enable device fabrication.

Methodology: Two approaches to address these issues discussed above are:

[1] Synthesize nanotubes which yield a mixture of tubes but later separate them into metallic and semiconducting fractions and further separate the fractions based on their diameter;

[2] in-situ control of the structural features (read 'diameter of tube') of nanotubes during the CVD process and hence control over their physical properties.

Further analysis of the origins of these problems might help in evaluating as well in choosing the best approach. All the carbon atoms in the nanotube are present in the sp^2 hybridized state, which essentially means the presence of lone of pair of electrons associated with each individual carbon atom. This lone pair of electrons is delocalized and they form an electron cloud along the length of the tube, consequently giving rise to strong Vander Waals interaction between the nanotubes. Vander Waals interaction between two tubes is around 30 keV/um[4] and the C-C single bond energy is ~ 3 eV, which means that the Vander Waals interaction between two tubes over a length of one

---

[4] This value is based on a discussion with Prof. Francesco Stellacci, MIT.

micron is equivalent to 10,000 C-C bonds!! These secondary interactions (Vander Waals forces), which are a result of delocalization of electrons in the nanotube are much stronger than the primary bonds! Any separation of nanotube bundles into individual tubes entails an application of force which is at least as strong as 30 keV or more. This indicates that in-situ control of structural features of nanotubes is likely a better option. One way to achieve the same is to use size-controlled nanocrystals as catalysts in a CVD process for the diameter-controlled growth of nanotubes. In addition, by using nanocrystals with the same orientation and shape may enable control over the chirality of the tubes as well.

Current catalyst preparation methods for CVD synthesis of SWNTs: Commonly used methods for catalyst preparation, include:

[1] Depositing a thin metal film of 1-100 nm using physical vapor deposition, followed by heating these thin films to form clusters which are capable of catalyzing nanotube growth; [11, 12]

[2] Spray coating and or spin coating of soluble metal precursor solutions such as nitrates or acetates on substrates; [13]

[3] Mixing catalyst salt solutions with high surface area catalyst supports such as Al_2O_3 or SiO_2 followed by drying-up process to generate nanoparticles on the supports; [14]

[4] Thermal decomposition of organo-metallic compounds such as iron pentacarbonyl, metallocenes; [15, 16]

[5] Metal nanoparticles synthesized using colloidal methods.[17]

A good synthesis technique for preparing discrete nanoparticles as catalysts for CVD synthesis of SWNTs should provide:

[1] Uniform diameter distribution of nanoparticles in the range of 1-5 nm, preferable smaller than 3 nm;

[2] Controlled spacing between the nanoparticles on the substrate for controlled growth of NTs from intricate complex arrays of catalysts;

[3] Ability to synthesize a wide variety of metal nanoparticles at room temperature without the need to considerably alter the synthesis conditions;

[4] Commensurate with current fabrication techniques, including contact printing, lithography and other micro-fabrication techniques to enable device fabrication based on NTs;

[5] Enable rational design and fabrication of new catalysts to further explore NT growth.

Although the first four methods previously listed, are relatively simple, they neither offer any control over the size nor the spacing between the nanoparticles. Until recently, thin metal films have been predominantly employed to catalyze NT growth using a CVD process. Usage of discrete nanoparticles as catalysts for growth of NTs is still in its infancy, though rapidly evolving. In spite of a significant progress in the synthesis of metal nanoparticles with uniform size distribution using colloidal methods, it is still a challenge to synthesize nanoparticles with narrow size distribution in the 1-5 nm size regimes. Additionally, at present colloidal syntheses methods for only few metals/metal oxides are known. Moreover, these methods vary from one metal to another and also involve relatively higher reaction temperatures (100-300°C). As will be demonstrated, the versatility of the BCP templating method to synthesize nanocrystals of different metals at room temperature without the need to considerably alter the synthesis conditions is a unique advantage of this method. Additionally, synthesis of transition metal nanoparticles, such as rhenium and ruthenium which have other wise been difficult to synthesize using traditional approaches provided an opportunity to investigate alternate new catalysts for nanotube growth. Comparing the catalytic efficacy of various metal nanoparticles for nanotube growth entails, first, identical size distributions of the nanoparticles, second, identical densities of particles on the substrate, and third, quantifiable densities of nanoparticles. To date, this has not been achieved through any of the catalyst methods listed above. The BCP method enabled synthesis of various nanoparticles with similar size distributions and identical particle densities enabling studies comparing the catalytic efficacy of various mono-metallic transition metal nanoparticles for the CVD growth of SWNTs. Most importantly, the catalytic yield was further improved while employing bi-metallic nanoparticles. The BCP method provided a facile route for the synthesis of wide-variety of bi-metallic nanoparticles, such as Fe-Mo, Co-Mi and Ni-Mo. Therefore, there still remains significant room for rational design and fabrication of discrete catalysts for NT growth.

Organization of this chapter

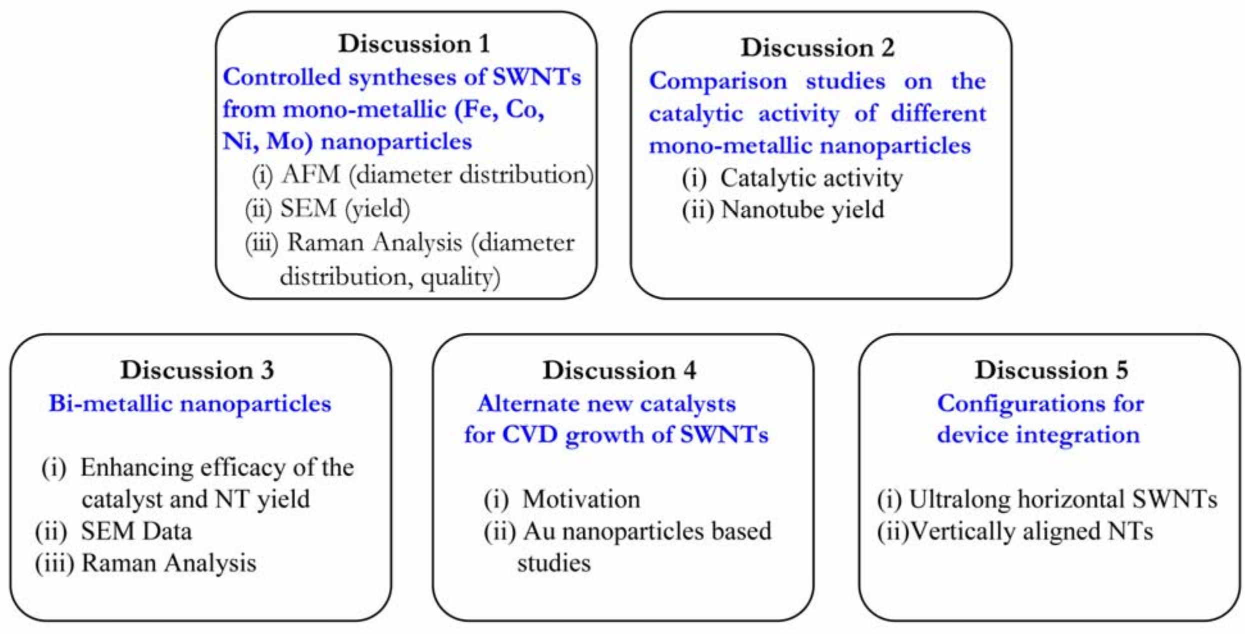

5.2 Experimental Methods and Details

Synthesis of CNTs using mono- and bi-metallic nanoparticles

Ethanol CVD: Nanotubes were grown using ethanol in a thermal CVD at ambient pressure in a 1 in. diameter quartz tube with a 15 in. heating zone. Substrates with nanoparticles were heated from room temperature to the growth temperature (900°C) in 12 minutes with a flow of argon (600 sccm) and hydrogen (440 sccm) gas mixture. Subsequently, nanotube growth was initiated by bubbling argon through ethanol and the growth was carried out for 10 minutes.

Methane+Ethylene CVD: The experimental setup remained the same as described above. The samples were heated from room temperature to the growth temperature (900°C) in 12 minutes in a flow of argon (1000 sccm) and hydrogen (500 sccm) gas mixture. Nanotube growth was initiated by replacing the argon flow with a gas mixture of methane (1000 sccm) and ethylene (10 sccm), and nanotube growth was carried out for 10 minutes.

Methane CVD: Growth conditions were similar to ethylene and methane CVD, except that the nanotube growth was initiated by replacing the argon flow with methane gas (1000 sccm) instead of the gas mixture.

SWNTs grown from Gold catalyst nanoparticles

The syntheses of SWNTs were carried out in a 2.5 cm diameter quartz tube furnace. Typically, substrates with Au nanoparticles (after O_2 plasma treatment) were loaded into the quartz tube and heated to growth temperature (800 or 900 °C) under Ar flow. At the growth temperature, the flow of Ar was replaced by a flow of 440 sccm H_2 and maintained for 15 min to reduce the nanoparticles. Subsequently, the synthesis was initiated by introducing a flow of 20 sccm C_2H_4, 30 sccm CH_4, and 440 sccm H_2 for 10 min. After growth, the hydrocarbon gases were turned off, the quartz tube was removed from the furnace, and a flow of 600 sccm Ar was activated as the tube cooled to room temperature.

Characterization of CNTs

Raman spectra were acquired on a custom-built optical microprobe using a laser excitation with ~4 mW power and E_{laser}= 1.92 eV (647 nm), which was obtained using a Krypton ion laser.

Lasers with excitation wavelengths of 685 nm and 488 nm were also used to collect Raman spectra. The laser spot size ranging between 0.25-1.0 um was employed in these investigations. Details for surface and chemical characterization techniques, including AFM, SEM, TEM and XPS were discussed in earlier in chapter 3.

5.3 Results and Discussion

5.3.1 Mono-metallic catalysts

Carbon nanotubes were grown from samples S5-S7, described in chapter 3, using ethanol CVD and CVD with a mixture of ethylene and methane gases in separate new quartz tubes to prevent any catalyst cross-contamination.[20] In the case of samples S6 and S7, it was observed that no nanotube growth would occur without reductive pre-treatment (using H_2 gas while pre-heating the samples to the reaction temperatures). However, this was not the case with the sample, S5. This indicated that Fe, and its oxide, $Fe_2O_3,$ as well as both Co and Ni in their native states catalyzed nanotube growth, but not their respective oxides, suggesting that oxidation state of the metal also plays an important role in the catalysis of nanotubes. AFM height images and corresponding cross-sectional images of nanotubes grown using ethanol CVD from samples S5, S6 and S7 are shown in Fig. 5.1b-d. All the AFM height images are 2.5×0.94 μm^2. These images clearly revealed the growth of nanotubes initiating from individual catalyst particles. The periodicity of nanoparticles was retained even after nanotube growth, which indicated that agglomeration of mono-metallic nanoparticles did not take place even when the growths lasted for 10-15 minutes at high temperatures (~900°C). Moreover, the retention in periodicity also indicated, first, the nanoparticles stayed firmly on the substrate even when heated to 900 °C, and second, the nanotube growth from these catalyst particles proceeded via the base-growth mechanism. The average diameters of the nanotubes grown from samples Fe (S5), Co (S6) and Ni (S7) using ethanol CVD are around 1.0 nm,

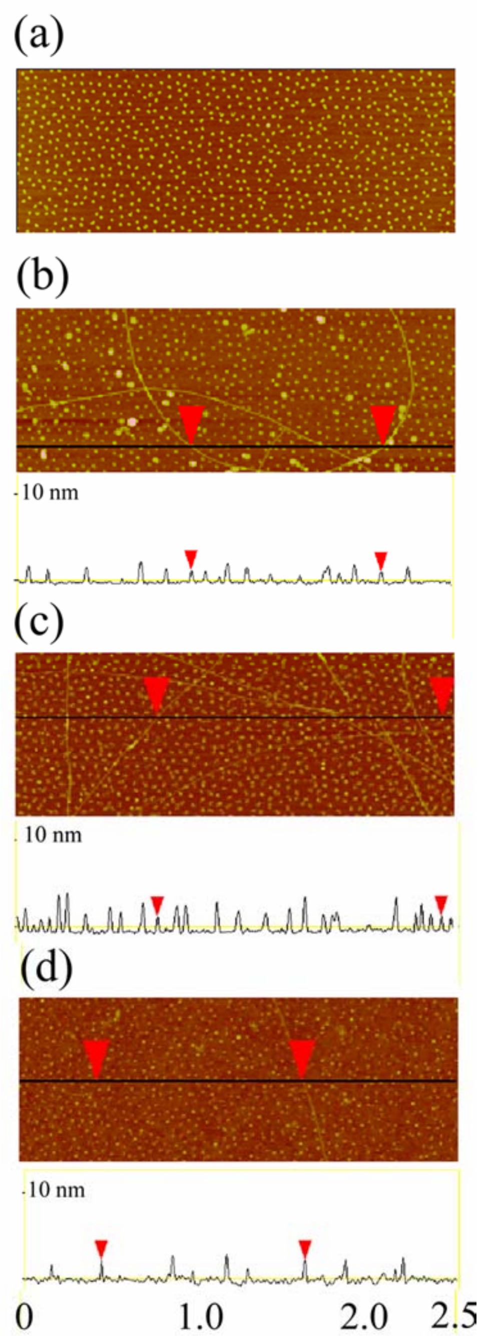

Figure 5.1: (a) A typical AFM height image (2.5 × 0.94 μm^2) of nickel oxide nanoparticles on a Si substrate. AFM height images and corresponding cross sectional images from samples Fe (S5)-(b), Co (S6)-(c), Ni (S7)-(d) after nanotube growth using ethanol CVD show the height of the nanotubes in correlation to the size of the nanoparticles.

1.9 nm and 1.8 nm respectively, which are a little smaller compared to the initial size of the catalyst. This is believed to have occurred due to the reduction of metal oxide nanoparticles to their metallic state while heating the samples in hydrogen gas.

Resonant Raman scattering had been employed to characterize SWNTs, both their quality as well as the diameter distributions. Brief introduction to Raman scattering of nanotubes is provided is appendix IIIb. Typical spectra of nanotubes grown from samples S5-S7 using ethanol CVD are shown in fig. 5.2, which revealed the quality of as grown nanotubes. The peaks in the low frequency region in the spectrum in the range of 100-400 cm^{-1} correspond to radial breathing modes (RBMs). The presence of RBM peaks indicated that the nanotubes either have a single wall or few walls. The peak centered around 1588 cm^{-1} corresponds to the G-band which is related to the in-plane vibrational modes of the graphite structures.[24] The presence of large G-band along with the absence of disorder induced band (D band) in the samples S5-S7 indicated a very high quality of as grown SWNTs from different metal catalysts.

Analysis of RBM peaks in the Raman spectra that were obtained from individual SWNTs was performed to further substantiate the AFM analysis of nanotube diameter distribution. Radial breathing modes in the Raman spectrum are a characteristic signature of SWNTs and are usually observed in the frequency range of 50-400 cm^{-1}. Importantly, the nanotube diameter is inversely related to this peak position (frequency) and is given by the following relation

$$\text{diameter}_{\text{nanotube}}\ (\text{nm}) = 233\ \text{cm}^{-1}/\omega_{\text{RBM}} \ \ldots.\ (1)\ ^{[24],\ 5*}$$

In these studies, a representative analysis of RBMs in the resonant Raman spectra were conducted using a large number of spectra collected from sample S8 (Fe-Mo) using multiple laser excitation wavelengths, including 488 nm and 685 nm. Figure 5.3a shows the RBM peaks in the low frequency

---

[5] The constant in the numerator depends on the type of the substrate.

regime of the Raman spectra obtained from individual isolated SWNTs from sample S8, using a laser excitation wavelength of 685 nm.

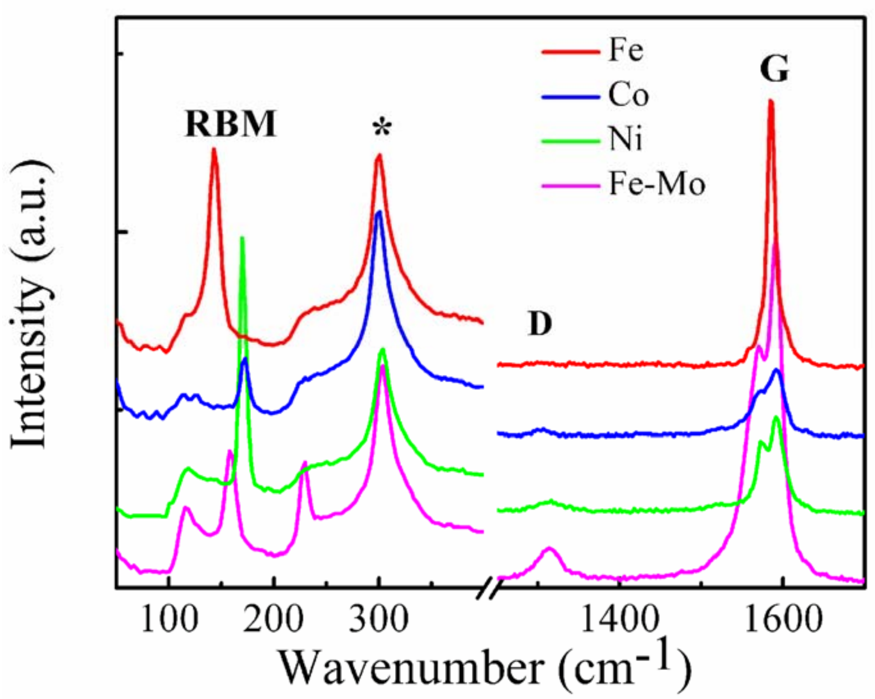

Figure 5.2: Raman spectrum of CNTs grown from S5-S8 using ethanol CVD showed the presence of RBM and G-bands. The peak marked by asterisk arises from SiO_2/Si. [22]

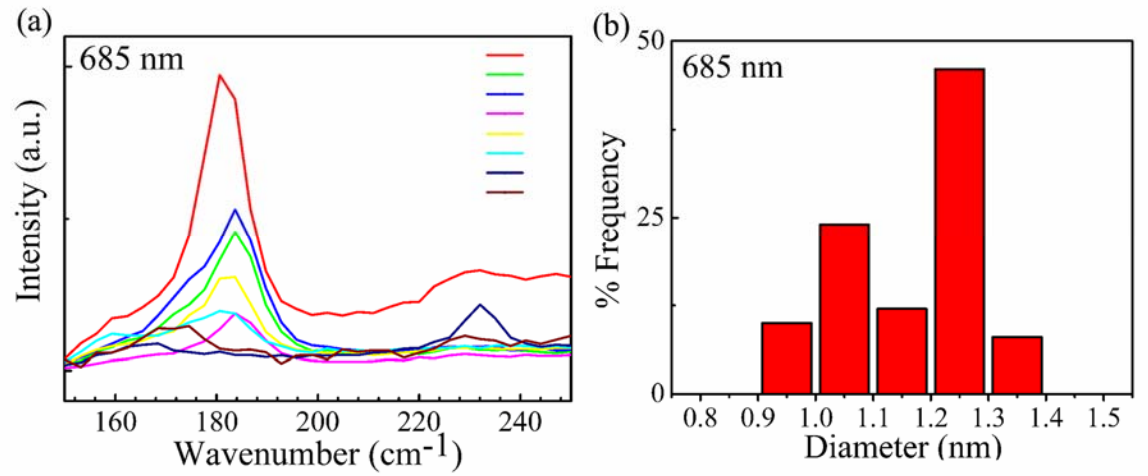

Figure 5.3: (a) Raman spectra of different individual nanotubes grown using ethanol CVD from sample S5 (Fe) (b) Diameter distribution analysis based on Raman analysis on RBM peaks performed on 60 nanotubes from the same sample.

The diameters of the nanotubes measured from 60 different resonant Raman spectra that were collected from different spots from the same sample were in the range 0.9-1.4 nm (histogram; fig. 5.3b), which are in the same range as the AFM height measurements, further corroborating the AFM results. Interestingly, not many tubes were in resonance with a laser with an excitation wavelength of 488 nm.

Collecting Raman spectra from nanotubes samples on substrates involved, aiming/shining a laser beam with 0.25-1.0 um spot size on the substrate surface and then collecting the resultant signal using a CCD camera. As most of the SWNTs obtained from different samples in these studies were present as isolated individual tubes, this often presented a technical challenge and complicated the ability to collect a significantly large number of spectra (n> 200). In contrast, all the previous analyses of nanotube diameter distribution with Raman spectra have involved bulk samples which ensure many nanotubes are simultaneously excited by the same laser spot and their Raman spectra can be collected at the same time. It is also emphasized that, to obtain accurate nanotubes diameter distribution based on Raman analysis, it is also necessary to use different laser excitation energies, as all the nanotubes in the sample may not resonate with a single excitation energy. In contrast to most previous reports, multiple excitation energies were employed in this work. In essence, the Raman analysis conducted in this study is more reliable and rigorous.

In summary, Raman analysis confirmed the synthesis of high quality SWNTs from different metal nanoparticles and the similarity in the diameter distributions of the nanoparticles (S8: 1.3 ± 0.2 nm) and the nanotubes (S8: 1.1 ± 0.3;) grown from them indicated very good diameter-controlled growth of SWNTs.

At times, instabilities during spin-casting micellar solution resulted in a non-uniformity in the thickness of the polymer film, which was thicker at the edges as compared to the centre of the substrate. The non-uniformities also depended on the size and shape of the substrates, and in some cases extended up to substantial range (500 um from the substrate edge towards the center, for substrate size of 6.25 cm^2). While the center of the substrates had a monolayer of nanoparticles, the edges had a higher density of nanoparticles. Figure 5.4 illustrates nanotubes grown from non-uniform arrays of Fe nanoparticles. It is emphasized that the nanotube growth in these experiments was performed using ethylene gas at 750-800 °C that resulted in a mixture of MWNTs and SWNTs. The edges had higher densities of nanoparticles that eventually led to vertically aligned growth of nanotubes.

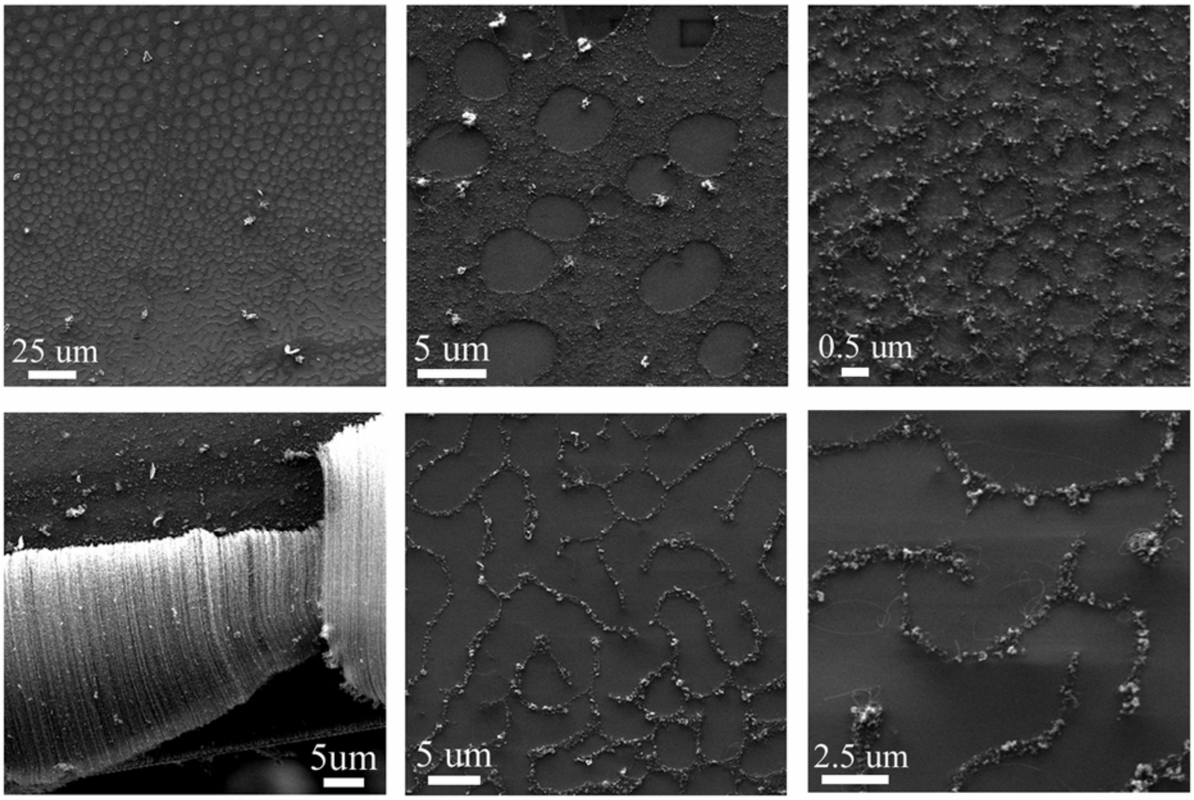

Figure 5.4: Non-uniformities in the spin-coated micellar films resulted in non-uniform growth of nanotubes. Higher densities of nanoparticles were observed along the edges of the substrates. Lower left image shows vertically aligned nanotubes at the edge of the substrate that were grown from Fe nanoparticles using ethylene gas at 750 °C. These discrepancies were avoided by first spin-casting on larger substrates whose edges were later trimmed before performing plasma treatment.

These non-uniformities in the spin-coated monolayers had a deleterious affect in which they render the nanoparticles at the center of the substrates inactive by depleting the carbon source at the edges of the substrate. Hence, it is critical to have uniformly spin-coated monolayers of polymer films for the uniform growth of SWNTs along the entire substrate. Thus, the discrepancy in the thickness of the polymer films was eliminated by spin-coating the micellar solutions on large substrates, say, 9 cm^2, and the edges were then trimmed to 6.25 cm^2, before performing plasma treatment.

5.3.2 Catalytic effect of mono-metallic nanoparticle catalysts

Although Fe, Co and Ni have all been widely used as catalysts, there haven't been any investigations comparing their catalytic effect, i. e., which elemental catalyst is more effective under certain set of synthesis conditions? This information is important for understanding the growth mechanism of SWNTs grown in a CVD process. To make reliable comparisons on the catalytic activity of different metal nanoparticles in a CVD process, it is not only necessary to have similar size distribution but also identical particle density on the substrate. The large uniform arrays of metal nanoparticles synthesized using the BCP template served as an excellent tool to perform such an investigation. The catalytic activities of mono-metallic nanoparticles for nanotube growth using different carbon feed stock (ethanol and ethylene+methane) were explored. In this section, results comparing the catalytic activity of Fe, Co and Ni nanoparticles using methane CVD and ethylene CVD are first discussed. In the next section, catalytic activities of Fe-Mo nanoparticles are presented.

Scanning electron microscopy images of nanotubes grown from samples S5-S7 using methane+ethylene CVD and ethanol CVD not only provide a clear comparison of the yield of nanotubes grown from different mono-metallic nanoparticles under identical growth conditions, but also revealed a difference in their catalytic activity while using different carbon feed stock. Figures

5.5 a, 5.5b and 5.5c are representative SEM images of nanotubes grown from samples Fe (S5), Co (S6) and Ni (S7) respectively using ethanol CVD. Corresponding images of nanotubes grown from methane+ethylene CVD are shown in figure 5.5d-f. Under identical growth conditions, the catalytic activities of both Co and Ni nanoparticles were higher than Fe nanoparticles, both in ethanol CVD as well in methane + ethylene CVD. This result is in contrast with that of a previous report [21] wherein the SWNT yield for Fe (Co) catalysts was much higher for ethylene (ethanol) CVD, implying a different growth mechanism based on the carbon source. However, in this case, consistently higher yields were observed for Fe, Co and Ni nanoparticles irrespective of the carbon source. In fact, a closer look at the results reported in the previous report revealed that the comparisons were performed between Fe and Co-Mo nanoparticles and erroneously reported for Fe and Co nanoparticles. Moreover, studies-to-date on the comparison studies have overlooked the primary criteria that were described previously and as such those results are questionable. The results on the catalytic activities of metal nanoparticles for nanotube growth are summarized in table 5.1 Moreover, as can be seen from the SEM images in fig. 5.5, under identical growth conditions and with a similar density of nanoparticles on the substrate, the yield of nanotubes grown from Co and Ni nanoparticles were higher compared to that of Fe nanoparticles. These results suggest that both Co and Ni serve as better catalysts for nanotube growth at 900 °C for nanotube growth. It is possible that these catalysts cause higher decomposition of carbonaceous source at 900 °C or probably the catalysts poisoning in their cases with hydrogen/carbon species is lower than that compared to Fe. It is emphasized that these comparison studies are based on experiments that were conducted under identical growth conditions at 900 °C. It may be possible that Fe may serve as a better catalyst at higher/lower temperatures as compared to Co and Ni at 900 C growth temperature.

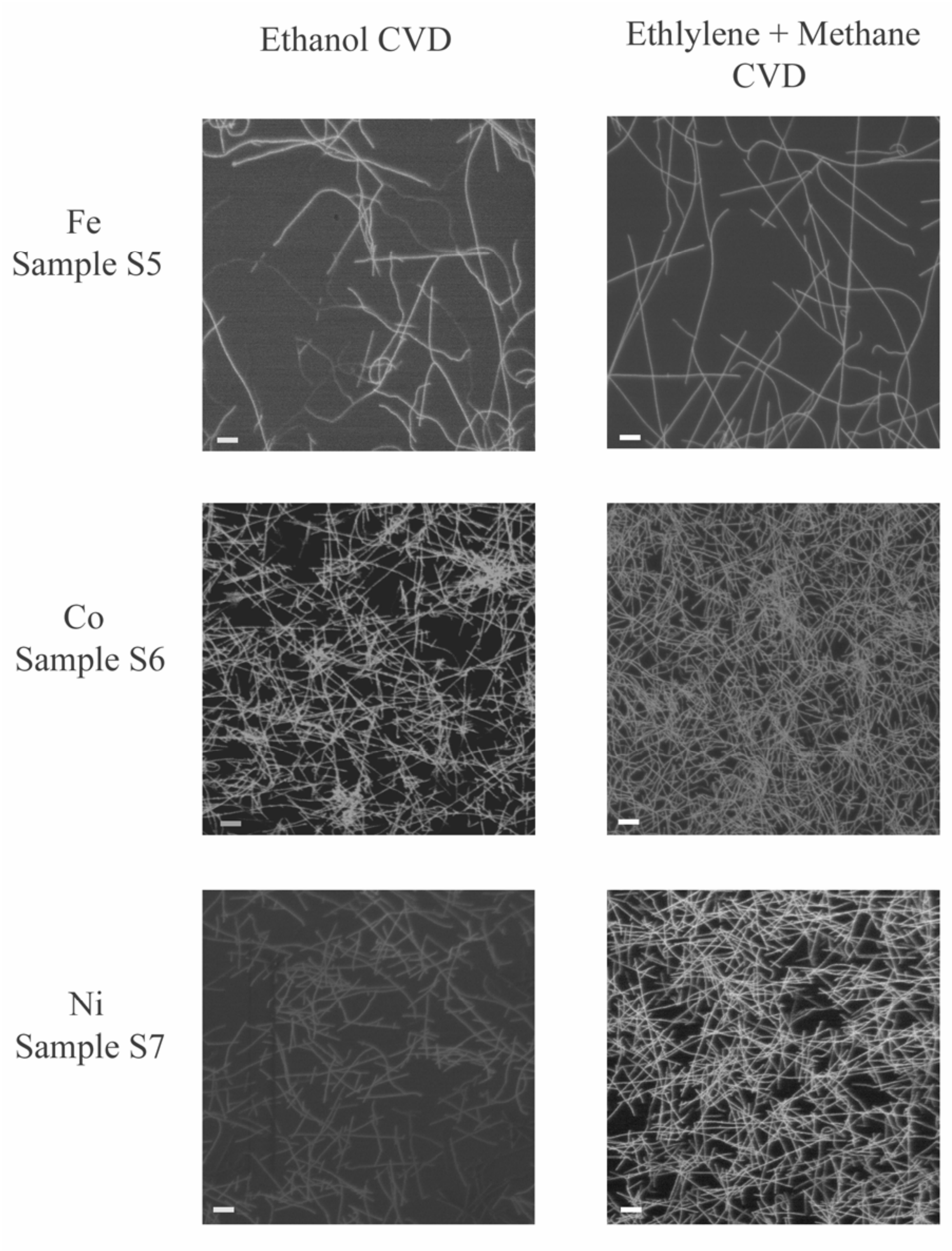

Figure 5.5: SEM images of nanotubes grown from different samples using ethanol CVD (methane+ethylene CVD) Fe (S5)-e (h), Co (S6)-f (i), Ni (S7)-g (j), all scale bars are 1 μm in size.

Table 5.1: Sample details of mono- and bi-metallic nanoparticles for CVD growth of nanotubes and conclusions on their catalytic activities based primarily on extensive SEM investigations.

Sample Details*	**Size **** (in nm)	**Ethanol CVD** Avg. size (yield: 1 lowest; 4 highest)	**Ethylene+Methane** Avg size (yield: 1 lowest; 4 highest)	**Comments on nanotube growth**
S1 (Fe_2O_3)	**2.5 ± 0.2**	-	-	
S2 (CoO_x)	**3.9 ± 0.3**	-	-	
S3 (NiO_x)	**3.8 ± 0.3**	-	-	
S4 (MoO_2)	-	No growth	No growth	
S5 (Fe_2O_3)	**1.1 ± 0.2**	1.1 nm **(4)**	**(4)**	**Ethanol CVD** Fe<Ni<Fe-Mo<Co **Ethylene+ Methane CVD** Fe<Ni<<Co
S6 (CoO_x)	**3.2 ± 0.3**	1.9 nm **(1)**	**(1)**	
S7 (NiO_x)	**1.9 ± 0.3**	1.8 nm **(3)**	**(2)**	
S8 (Fe-Mo)	**1.3 ± 0.2**	1.2 nm **(2)**	**(3)**	
S9 (AuO_x)	**3.1 ± 0.4**	No growth ?	1.0-2.0 nm	Different synthesis conditions as compared to S5-8
S10 (Au-Re)	-	-	-	
S11 (Re)	-	-	-	

* In this column, the oxidation state of mono-metallic nanoparticles prior to the nanotube growth is indicated.

** Size distribution analysis was performed based on TEM data.

5.3.3 Bi-metallic Catalysts

The densities of mono-metallic nanoparticles on the Si substrate that were synthesized using the BCP template were around $10^{11}/cm^2$. However, the densities of SWNTs grown from these samples were significantly lower (only <5% nanoparticles catalyzed SWNT growth). Improving the efficacy of the catalyst as well understanding the parameters that affect it are paramount to enable device fabrication. There are a couple of approaches to possibly improve the catalytic yield of the nanoparticles, including (1) by optimizing the current syntheses conditions; and (2) by synthesizing bi-metallic catalysts, where in the co-catalyst could assist the primary catalyst either by decomposing the carbonaceous source and or by removing the deleterious effects caused by surface adsorption of by-product species on the primary catalyst, which usually poison it.

One of the most commonly employed material as a support material is Molybdenum.[16, 19] It is well known that Mo is used as a catalyst for the conversion of methane to benzene as it helps in the decomposition of hydrocarbon molecules.[24, 25] Therefore, the presence of Mo as a co-catalyst may enhance the nanotube yield. The block copolymer micellar method provided a facile route for the synthesis of bi-metallic nanoparticles. Investigations in this work involved evaluation of Fe-Mo nanoparticles for enhancing the yield of nanotubes. The Fe-Mo nanoparticles (S8) were prepared by loading the corresponding metal precursors in the di-block copolymer micellar solution in a 5:1 ratio. Catalytic activity of samples S5 (Fe: 1.1 ± 0.2 nm) and S8 (Fe-Mo: 1.3 ± 0.2 nm) for nanotube growth were compared using ethanol CVD. A typical SEM image of the nanotubes grown from samples S5 (Fe) and S8 (Fe-Mo) are shown in figures 5.6c and 5.6d, respectively. Molybdenum nanoparticles by themselves did not catalyze any nanotube growth and the catalytic yield of bi-metallic Fe-Mo nanoparticles was at least an order of magnitude higher than Fe nanoparticles alone (see figure below), clearly indicating that the presence of Mo in the system increased the efficiency of the catalyst system.

Raman spectrum from sample S8 (fig. 5.2) revealed the presence of D band in addition to the peaks from the RBM and the G band. A high G-band to D-band intensity ratio in the Raman spectrum indicated a very high quality of as grown nanotubes form S8. The presence of small D-band in this spectrum indicated the presence of amorphous carbon, which could also be seen in the SEM image as small globules on the nanotubes. These results corroborated that relatively more carbon decomposition takes place in the case of Fe-Mo as compared to the Fe only sample, confirming the role of Mo co-catalyst!

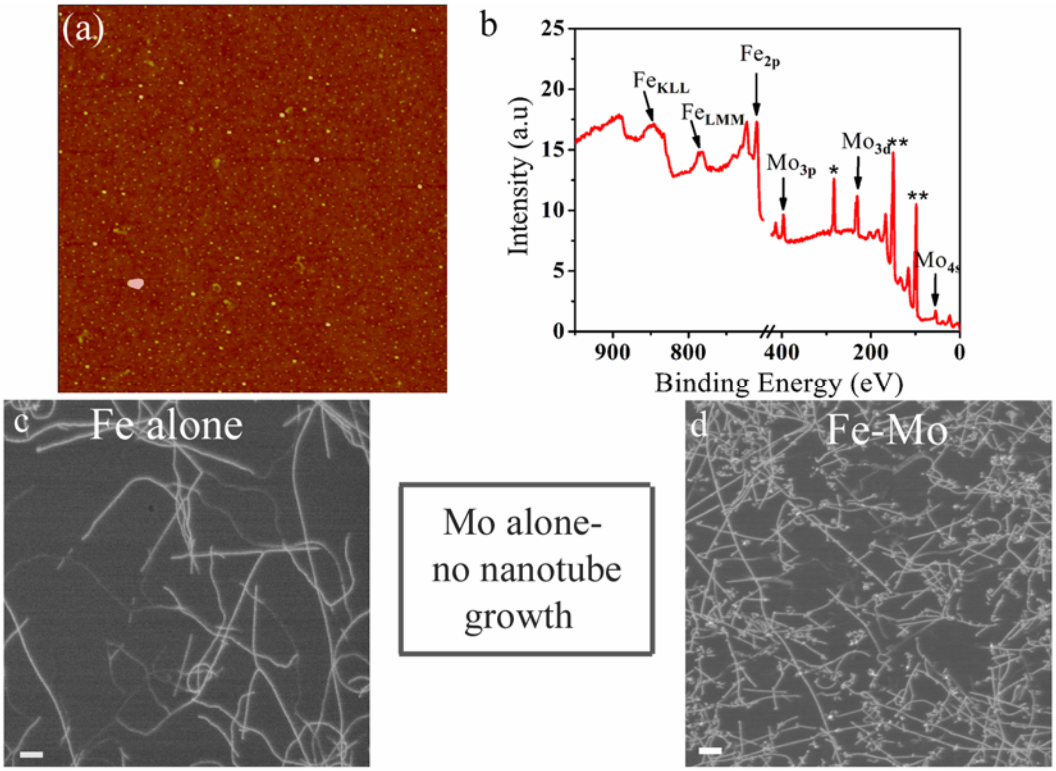

Figure 5.6: (a) An AFM image showing Fe-Mo (S8) bi-metallic nanoparticles (b) XPS spectrum revealing the presence of characteristic peaks from Fe and Mo (c & d) SEM images of nanotubes grown from Fe (S5) and Fe-Mo (S8), respectively, using ethanol CVD revealing their catalytic activities.

5.3.4 New Catalysts for CVD growth of SWNTs

By far, the majority of work reporting CVD synthesis of carbon nanotubes has focused on thin films and nanoparticle catalysts based on Fe, Co, and Ni. At the same time, there have been reports of SWNT and multi-walled nanotube (MWNTs) growth employing catalysts based on other metals.[26-28] Exploring alternative catalysts for nanotube growth is an interesting prospect for a number of reasons. For example, NMR experiments have indicated that the ratio of metallic to semiconducting SWNTs grown with Co/Ni-based catalysts is different than when Rh/Pd catalysts are used.[29] This suggests that it may be possible to change the ratio of metallic to semiconducting nanotubes by varying the catalyst composition. In addition, currently in the field of nanotube research, there is no clear understanding regarding the important factors that influence nanotube growth using metal nanoparticles as catalysts. Based on the evaluation of carbon solubility and carbide stability from the carbon-metal binary phase diagrams, it has been suggested that Fe, Co, and Ni are the only elements capable of catalyzing SWNT growth among 70 elements that include all of the transition metals.[30] However, this is contradicted by experimental results. Therefore, a detailed comparison between the similarities and differences of various metal catalysts might further help in elucidating the growth mechanism in greater depth, in addition to providing valuable insight.

Gold is one potentially interesting alternative to Fe, Co, and Ni. Bulk gold has historically been regarded as relatively inactive toward catalyzing chemical reactions due to its completely filled 5d shell and relative high first ionization energy.[31] Over the past decade, however, it has been shown that nanoscale gold particles possess enhanced catalytic activity over their bulk counterpart due to size effects.[27, 32] Additionally, bulk Au has a melting point of 1064 °C, and so, due to size effects, Au nanoparticles of diameters suitable for SWNT growth are expected to have melting points as low as 300 °C.[33] This low melting point may enable lower CVD growth temperatures than is possible with Fe, Co, and Ni under otherwise identical conditions, advantageous for the direct integration of nanotubes into different technologies with temperature limiting materials. In this paper, we present the first demonstration of SWNT growth by thermal CVD employing gold nanoparticles.

Characterization of Gold nanoparticles arrays

Nanotube growth was performed using highly monodisperse Au nanoparticles catalysts prepared by block copolymer templating technique. Figure 5.7a shows the Fourier transform infrared spectra (FT-IR) of the P4VP solution before, and, after the addition of Au precursor. The weakening in the intensity of the bands at 1415 and 1556 cm^{-1}, which are a characteristic of pyridine units, and the appearance of new bands at 1616 and 1634 cm^{-1}, a characteristic of protonated pyridine, confirmed binding between the pyridine unit and the Au precursor. Figure 5.7b is an AFM height image showing uniform arrays of Au nanoparticles after oxygen plasma treatment. The inset is a 2-D fast Fourier transform (FFT) of the AFM image revealing an ordered arrangement of Au nanoparticles along a quasi-hexagonal lattice. Figure 5.7c is a TEM image of the Au nanoparticles on silicon substrate. The average size of the nanoparticles as measured from the AFM height images after O_2 plasma treatment is 3.1 ± 0.4 nm (inset in fig. 5.7c). The lattice fringes from a gold nanocrystal are shown in fig 5.6d. XRD samples were prepared by vacuum-drying a droplet of the micellar solution on quartz substrates for few hours prior to oxygen plasma treatment. Figure 5.7e shows the XRD spectrum collected from Au nanoparticles on a quartz substrate after oxygen plasma treatment. Since the quantity of Au nanocrystals on the substrate is rather low ~ a monolayer, a majority of the signal arises from the underlying substrate (for comparison, the spectrum from a blank substrate is also provided in the same figure). The diffraction peaks at 38.2º, 44.5º, 64.9º and 77.8º indicated that Au is present in its metallic form consistent with the TEM data. The presence of higher binding chemistry as observed in the XPS spectra in conjunction with the XRD data suggested that the higher binding chemistry is very likely to be present as a shell on the Au nanoparticles.

SWNTs grown from Gold catalyst nanoparticles

Numerous trials were performed to evaluate the influence of various process parameters on nanotube yield using Au nanocatalyts. It was found that no growth would occur without a reductive pretreatment, and that a process temperature of 800 °C resulted in a higher yield than 900 °C. Figure 5.6f shows the high-resolution XPS spectra of Au nanoparticles after O_2 plasma, after reductive pretreatment, and finally after CVD. Two chemistries of gold are observed prior to the reductive pretreatment, with the higher binding energy possibly attributable to either a residual shell of gold chloride or gold oxide (as a result of plasma treatment) on the nanoparticles. These higher binding energy chemistries disappear after the reductive pretreatment, suggesting that the H_2 treatment successfully removes this residual material. Given the inability of unreduced particles to successfully catalyze nanotube growth, it can be concluded that the presence of these higher binding energy chemistries of gold somehow inhibited nanotube growth.

The presence of densely populated nanotubes on the surface of the substrate after CVD at 800 °C as shown in a representative SEM image (fig. 5.8a) indicated that Au serves as an efficient catalyst. AFM height images of nanotubes revealed that the growth of nanotubes occurred from individual catalyst nanoparticles with diameters ranging from 1 to 2 nm (fig. 5.8b). The presence of radial breathing modes (RBM) in the spectra at various spots on the surface verified that these structures are SWNTs (fig. 5.9). Using the relationship discussed earlier (equation 1) the diameters of the SWNTs were found to be between 1.2 and 1.8 nm, consistent with the AFM height measurements. In addition, the absence of disorder-induced Raman mode (D-band) at around 1300 cm^{-1} indicated the high quality of as-grown SWNTs (inset of fig. 5.9).

Interestingly, a decrease in the density of the gold nanoparticles on the substrate was observed after CVD. This could be due to either evaporation of gold from the substrate (as a result of the low melting point of the Au nanoparticles) or possibly the diffusion of gold into the substrate. In addition, the average diameter of the nanoparticles (as measured by AFM) appeared to decrease from 3.1 nm to ~2.0 nm. This could again be due to the evaporation of gold from the substrate or reduction of the oxide shell. At present, attempts to grow SWNTs at temperatures lower than 800 °C using thermal CVD have not been successful and it is believed that this is mainly due to the thermal energy required for cracking the carbon feedstock. A two-stage furnace or other means to

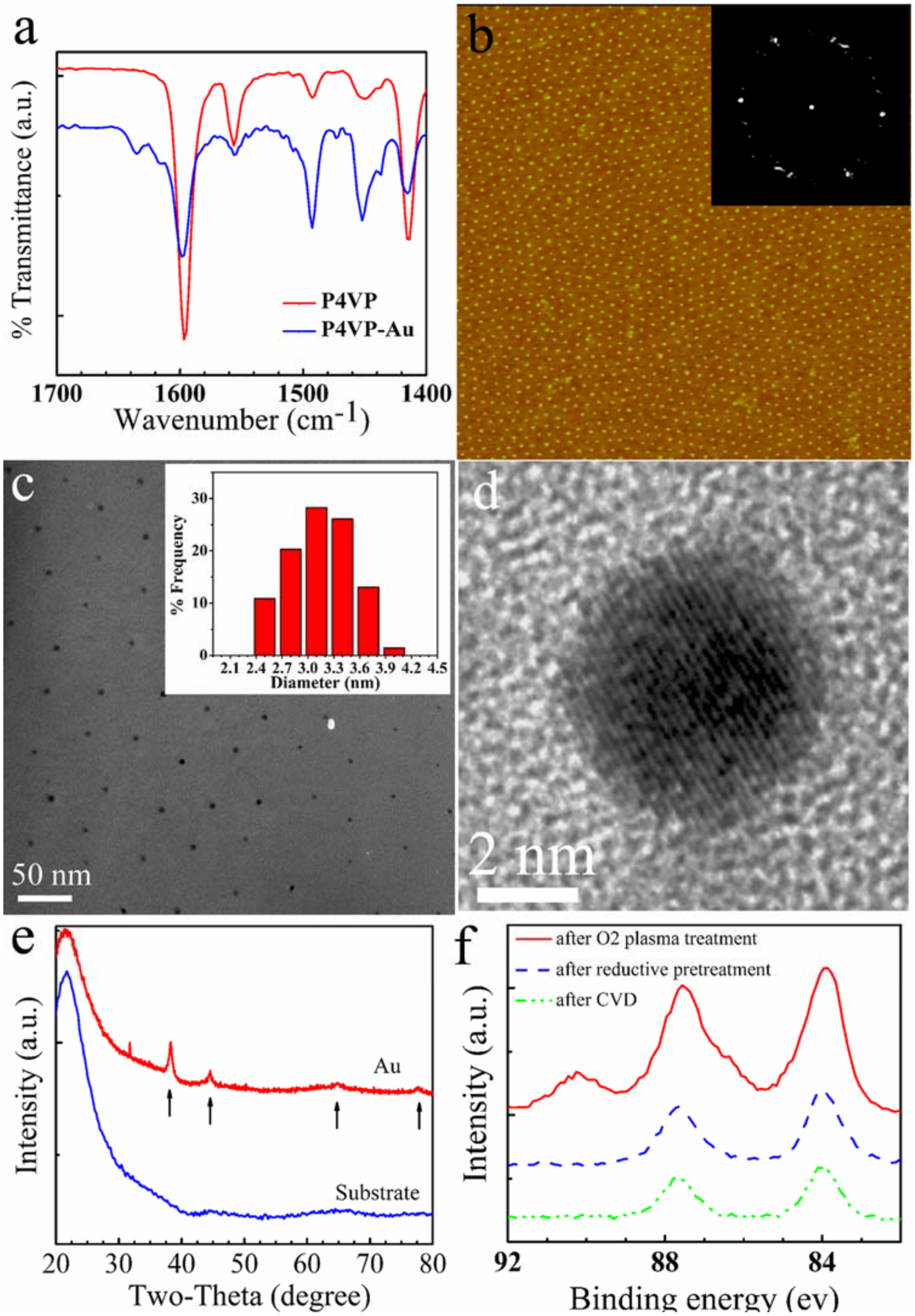

Figure 5.7: (a) FTIR spectra of P4VP with and without the Au precursor. (b) An AFM image showing uniform arrays of Au nanoparticles. Inset is a FFT image from the center of the AFM image (c) A TEM micrograph of Au nanocrystals on Si substrate. Inset showing a histogram of the size of Au nanocrystals. (d) A lattice resolved image of Au nanocrystals (e) XRD spectra of blank quartz substrate and Au nanocrystals (f) High-resolution XPS spectra of Au nanocrystals (4f peak) at various stages of treatment.

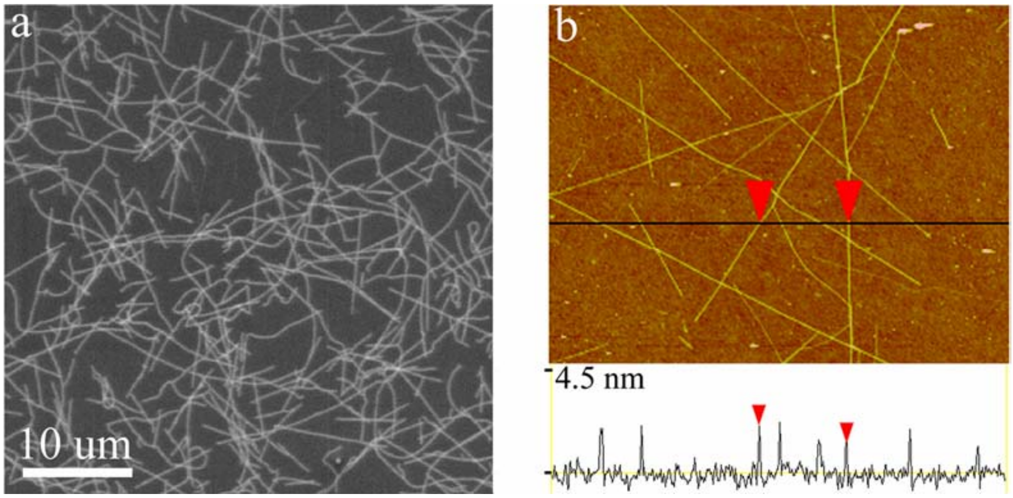

Figure 5.8: (a) SEM image of nanotubes grown from Au catalysts (b) A typical AFM height image and the corresponding cross sectional image showing the height of the nanotubes.

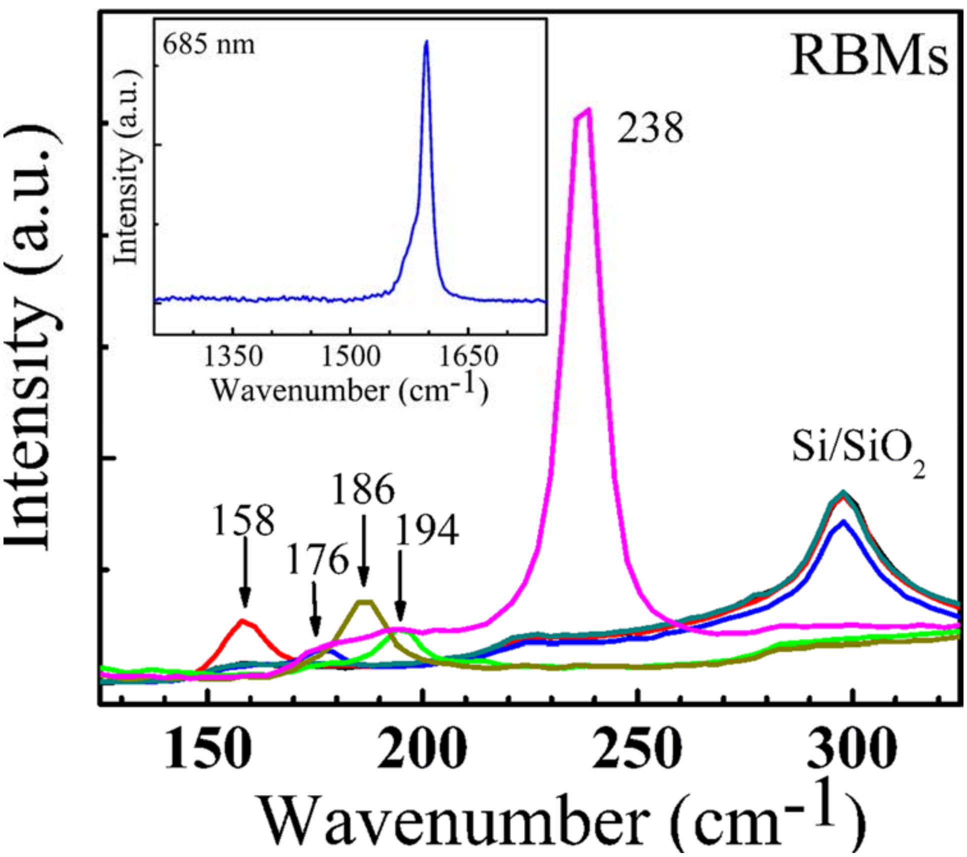

Figure 5.9: Raman spectra of the nanotubes grown from Au catalysts. The inset shows the presence of G-band (~1590 cm^{-1}) and the absence of D-band (~1350 cm^{-1}).

decompose the hydrocarbon gases, such as hot-filament CVD or plasma-enhanced CVD,[34] may eventually lead to a lower growth temperature with Au nanoparticles catalysts.

Investigations are currently underway to achieve low-temperature SWNT growth. Given the increased inter-atomic distance of Au over Fe, Co, or Ni, it is possible that the chirality distribution of SWNTs grown from the Au nanoparticles could be different from those of conventional catalysts. This success synthesis of SWNTs using Au nanocatalysts opens up the route for the investigation of chirality modification through parameter control during the CVD.

5.3.5 Device Integration -horizontal & vertical configurations

So far, controlled synthesis of SWNTs from different size-controlled metal nanocrystals has been demonstrated. To enable device fabrication, it is critical to control nanotube growth in either a horizontal (nanotube aligned parallel to the surface) or a vertical configuration (nanotubes perpendicular to the surface) from pre-defined locations. Experiments exploring such investigations were conducted in collaboration with Jing Kong group and Anastasios John Hart at MIT, and these experiments have met with considerable success.[6] Aligned growth of nanotubes parallel to the substrate surface are immensely useful for potential applications, including, CNT based field effect transistors (FETs), as components for interconnects, etc. On the other hand, vertically aligned nanotubes on the surface, exhibit significant potential for opto-electronic applications including, field emission displays, in vertical channel FETs. Lots of investigations on vertically aligned MWNTs and few investigations on vertically aligned SWNTs have been previously reported. However, almost all of these studies were conducted using catalyst nanoparticles with non-uniform size that provided no control over the as grown 1-D nanostructures. Here, monodisperse catalysts

---

[6] Experimental parameters for aligned growth of extra long SWNTs along the substrate surface were first developed by Alfonso Reina (Jing Kong Group, MIT) and have been recently reported. [36]

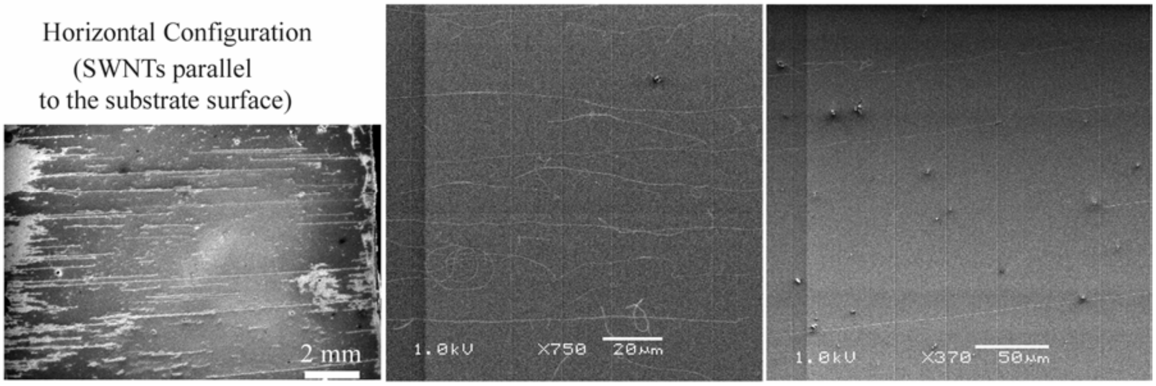

Figure 5.10: SEM micrographs showing ultralong SWNTs (~ 12 mm) grown using Co catalysts, along the length of the substrate, from methane CVD.

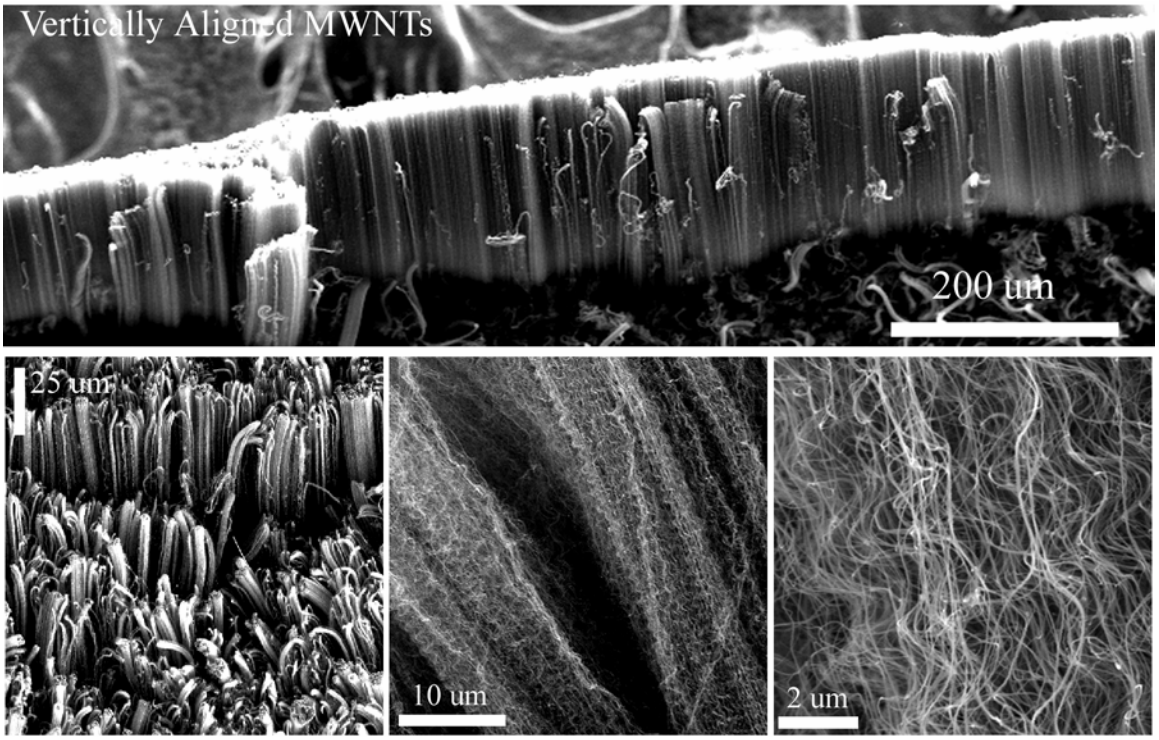

Figure 5.11: SEM micrographs showing vertically aligned MWNTs grown using Fe catalysts, from ethylene CVD.

synthesized using BCP templates were employed, that yielded close control over the diameters of the as grown nanotubes for both horizontal (fig. 5.10) and vertical configurations (fig. 5.11).

5.4 Summary

SWNTs possess an appealing array of electrical, optical and chemical properties. Importantly, the physical properties of a nanotube are dependent on its diameter and the chirality. In every variation of the catalyst assisted CVD method used for synthesizing SWNTs, the composition and morphology of the catalyst nanoparticles are critical in determining the structure, length, and yield of nanotubes which will result. A general method for synthesis of transition metal nanoparticles (Fe, Co and Ni) that served as catalysts for nanotube growth, with sizes less than 3 nm (standard deviation 9-12%) and uniform spacings between the nanoparticles has been developed. Diameter-controlled growth of SWNTs using wide variety of mono-metallic nanoparticles, including Fe, Co and Ni has been demonstrated in this work. While similar results demonstrating diameter-controlled growth of nanotubes have been published, one of the highlights of this work lays with the catalyst preparation method.

Comprehending the role of metal catalysts in CVD growth of SWNTs is crucial for understanding the nanotube growth mechanism. Even though Fe, Co and Ni nanoparticles have been widely employed as catalysts for nanotubes, investigations comparing their catalytic activities have been lacking, primarily due to the requirements for identical average sizes and identical areal densities on the substrates. Moreover, it has been claimed anecdotally that Fe serves as a better catalyst than both Co and Ni while using hydrocarbon feed stock in a catalyst assisted CVD process. To make reliable comparisons on the catalytic activities of different metal nanoparticles, it is not only necessary to have identical size distributions but also identical particle densities on the substrate. The PS-P4VP templates enabled syntheses of mono-metallic nanoparticles that satisfied the aforementioned criteria. The systematic and rigorous experiments that been reported for the first time have not only provided a clear comparison on the catalytic efficacies of the Fe, Co and Ni for SWNT growth, but also revealed a difference in their catalytic activity while employing different carbon feedstock (hydrocarbon as compared to alcohol based carbon feed stock). Interestingly, these experiments revealed that under identical growth conditions using both the carbon feed stock, Co and Ni serve as better catalysts than Fe and refuted the anecdotal claim.

The yield of SWNT growth while employing various mono-metallic nanoparticles varied between 0.5-5%. Alternate novel ways to improve the yield of nanotubes, including those employing Fe-Mo bi-metallic catalysts are also being reported for the first time as well. While Mo by itself did not catalyze nanotube growth, the yield of nanotubes increased by an order of magnitude while employing Fe-Mo as catalysts as compared to Fe nanoparticles.

By far, the majority of work reporting CVD synthesis of carbon nanotubes in the literature has focused on thin films and nanoparticles catalysts based on Fe, Co, and Ni. While transition metallic elements have good solid solubilities for carbon and may serve as catalysts for nanotube growth, the biggest obstacles have been associated with their synthesis in the form of thin films or nanoparticles (Re, Rh, etc). Exploring alternate new catalysts is an interesting prospect for reasons, including (1) lowering of nanotube synthesis temperature as compared to the current synthesis temperatures that range between 900-1100 °C and (2) for determining the correlation between the catalyst and the chirality of the resulting SWNTs. Based on the binary phase diagrams of metallic elements with carbon, few metals were chosen to explore if they catalyze SWNT growth. This work was performed in collaboration with Jing Kong group. Herein, metal nanoparticles, including those based on Au, Re and Au-Re were synthesized using PS-P4VP templates. While some of these studies are currently underway, the first demonstration of SWNT growth by thermal CVD employing Au nanoparticles was recently reported by us. Concurrent with this work, a couple of investigations have also reported synthesis of SWNTs employing thin films based on noble metals, including Au, Ag and Cu, corroborating our results.[31]

References

[1] Iijima S, *Nature* **1991**, *354,* 56

[2] Tans S J, Verschueren A R M and Dekker C *Nature* **1998**, *393,* 49

[3] Martel R, Schmidt T, Shea H R, Hertel T and Avouris P, *Appl. Phys. Lett.* **1998**, *73,* 2447

[4] Li H J, Lu W G, Li J J, Bai X D and Bai C Z, *Phy. Rev. Lett.* **2005**, *95* 086601

[5] Naeemi A, Sarvari R and Meindl J D *IEEE Electron Device Letters* **2005**, *26,* No. 2 84

[6] Rinzler A G, Hafner J H, Nikalaev P, Lou L, Kim S G, Tomanek D, Norlander P, Colbert D T and Smalley R E, *Science* **1995**, *269,* 1550

[7] Misewich J, Martel R, Avouris P, Tsang J C, Heinze S and Tersoff J *Science* **2003**, *300,* 783

[8] Saito R, Dresselhaus M S and Dresselhaus G *Physical Properties of Carbon Nanotubes* (Imperial College Press: London), **1998**

[9] Fuhrer M, Park H and McEuen PL *IEEE Trans. on Nanotech.* **2002**, *1,* 78

[10] Kong J, Soh H T, Casell A M, Quate C F and Dai H, *Nature* **1998**, *395,* 878

[11] Delzeit L, Chen B, Casell A, Stevens R, Nyugen C and Meyappan M *Chem. Phys. Lett.* **2001**, 348, 368

[12] Ren Z F, Huang Z P, Xu J W, Wang J H, Bush P, Siegal M P and Provencio P N *Science* **1998**, *282,* 1105

[13] Murakami Y, Miyauchi Y, Chiashi S and Maruyama S 2003 *Chem. Phys. Lett.* **2003**, *377,* 49

[14] Kong J, Casell A M and Dai H *Chem. Phys. Lett.* **1998**, *292,* 567

[15] Cheung C L, Kurtz A, Park H and Lieber C M *J. Phys. Chem. B* **2002**, *106,* 2429

[16] Li Y, Liu J, Wang Y and Wang Z L *Chem. Mater.* **2001***, 13,* 1008

[17] Choi H C, Kundaria S, Wang D W, Javey A, Wang Q, Rolandi M and Dai H J *Nanolett.* **2003**, *2*, 157

[18] M.S.Dresselhaus, G. Dresselhaus, A. Jorio, A.G. Souza Filho, R.Saito, *Carbon* **2002**, *40*, 2043

[19] Kitiyanan B, Alvarez W E, Harwell J H and Resasco D E 2000 *Chem. Phys. Lett.* **317** 497

[20] Franklin N R and Dai H *Adv. Mater.* **2000**, *12* No. 12, 890

[21] Mizuno K, Hata K, Saito T, Ohshima S, Yumura M and Iijima S 2005 *J. Phys. Chem. B* 2005, *109* 2632

[22] Temple P A and Hathaway C E *Phys. Rev.***1973***, B 7* 3685

[23] Dresselhaus M S, Dresselhaus G, Jorio A, Souza-Filho A G and Saito R, *Carbon* 2002, *40*, 2043

[24] Wang L, Tao L, Xie M, Xu G, Huang J and Xu Y *Catal. Lett.* **2003***, 21* 35

[25] Liu S, Wang L, Ohnishi R and Ichikawa M *J. Catal.* **1999,** *181* 175

[26] Lee C J, Lyu S C, Kim H-W, Park J W, Jung H M, Park J *Chem. Phys. Lett.* **2002** *361*, 469.

[27] Lee S Y, Yamada M, Miyake M *Carbon* **2005**, *43*, 2654

[28] Wal R LV, Ticich T M, Curtis V E. *Carbon* **2001**, *39*, 2277

[29] Tang X-P, Kleinhammes A, Shimoda H, Fleming L, Bennoune K Y, Sinha S, Bower C, Zhou O, Wu Y *Science* **2000**, *288*, 492

[30] Deck C P, Vecchio K *Carbon* **2006**, *44*, 267

[31] Bailar J C *Comprehensive Inorganic Chemistry*; Pergamon: New York, 1973; Vol. 1,129

[32] Schmidt G *Chem. Rev*. **1992**, *92*, 1709

[33] Buffat P, Borel J-P *Phys. Rev. A* **1976**, *13*, 2287

[34] Kurti J, Zolyomi V, Kertesz M, Sun G *New J. Phys.* **2003**, *5*, 125.1

[35] Li Y, Mann D, Rolandi M, Kim W, Ural A, Hung S, Javey A, Cao, J, Wang D, Yenilmez E, Wang Q, Gibbons J F, Nishi Y, Dai H *Nano Lett.* **2004**, *4*, 317

[36] Reina A, Hofmann M, Zhu D, Kong J *J. Phys. Chem. C* **2007***111,* 7292

Chapter 6

Electrochemical Synthesis of Metal Nanocrystals

Abstract

An alternate simple, yet a large scale robust technique, based on electrochemical technique to synthesize metal nanocrystals on substrates is presented. The investigations in this chapter focus primarily on Au nanocrystals and their catalysis for the growth of Si nanowires. Au nanocrystals were synthesized with mean diameters ranging from 10-50 nm and standard deviations varying between 6-11%. Cross-sectional TEM data in conjunction with plan view TEM data revealed their crystalline nature, confirmed their size and shape monodispersity, and provided clear insight about the 3-D shape of the Au nanocrystals and the Au-Si interface. Additionally, the use of size-controlled Au nanocrystals as catalysts in a CVD process resulted in the diameter-controlled growth of silicon nanowires. Given the widespread acceptance of the electrochemical processes for fabricating Cu interconnects, it may be easier to integrate the process with the microelectronics industry for the hierarchical growth of diameter-controlled semiconducting nanowires and carbon nanotubes from size-controlled metal nanocrystals on Si substrates.

6.1 Introduction

Carbon nanotubes and semiconducting nanowires are being considered as important components for next generation devices due to their excellent physical properties.[1-5] The physical properties of 1-D materials such as semiconducting nanowires are largely dependent on their diameter. Moreover, the diameter of these 1-D systems depends largely on the size of the catalysts from which they are grown in a vapor-liquid-solid (VLS) growth mechanism[6-8] in a chemical vapor deposition (CVD) process. Thus, achieving uniform physical properties for these systems entails using a narrow size distribution of catalyst particles grown on substrates.

Most of the technologically important 1-D materials such as nanotubes and inorganic semiconducting nanowires are based on C, Si and III-V compounds. In addition, these materials have reasonable solubility in transition metals (Fe, Co, Ni, Mn, Au, Cu, etc), and, hence the latter could be employed as catalysts[9] for their growth in a CVD process. Currently, metal colloids synthesized using wet chemistry methods are employed as catalysts. The electronic properties of the transition metals, and metals in general, have motivated us to explore an electrochemical method for the synthesis of metal nanoparticles directly on n-Si substrates. In addition to being a simple, cheap, efficient room temperature process, this method is versatile in its ability to deposit a wide variety of metals. The unique ability of this electrochemical process to synthesize nanocrystals of different metals at room temperature without the need to considerably alter the synthesis conditions may facilitate their integration into current microelectronics fabrication. Moreover, electrodeposition on n-Si involves conduction electrons and the nucleation and growth are dependent on applied potential, which can be controlled externally.[12] Thus, applied voltage may be used to control the size and density of nanocrystals on Si. Many device applications require the alignment of the nanoparticles on substrates, and, to date, there is no simple technique to achieve this during growth.

The presented electrochemical method offers great promise in addressing the issue. Given the widespread acceptance of the electrochemical processes for fabricating Cu interconnects, it may be easier to integrate the process with the microelectronics industry for the hierarchical growth of diameter-controlled semiconducting nanowires and carbon nanotubes from size-controlled metal nanocrystals on Si substrates. Gold has been a candidate material,[9] for the growth of a wide variety of 1-D materials, and, hence, the investigations in this work have focused primarily on the synthesis of Au nanocrystals.

The two commonly known low energy surfaces are the basal plane of graphite and hydrogen terminated (100) silicon substrate [H-Si (100)]. Electrochemical growth of metallic powders,[13-14] electrochemical synthesis of many metal microparticles on the basal plane of graphite,[15-17] and thin film growth of metals on semiconductors such as Si and GaAs from non aqueous solutions have been previously reported.[18-21] The latter has been of particular interest because of the type of potential barrier formed at the metal- semiconductor interface. Few investigations have been reported on the growth of metal and semiconductor nanoparticles on graphite from both aqueous and non-aqueous solutions using electrochemical methods,[14-16] and fewer reports are available on the growth of metal nanoparticles on Si substrates in non-aqueous solutions using a similar method.[20] Though electrochemical methods have been widely explored, there are no reports on using this method for the controlled synthesis of metal nanoparticles on semiconducting substrates from aqueous solutions.

6.2 Experimental Details

Electrochemical synthesis of Au nanocrystals: Gold nanocrystals were synthesized on low energy H-Si (100) (n-type) substrates from dilute hydrogen tetrachloroaurate ($HAuCl_4{\cdot}3H_2O$, Alfa

Aesar, 99.99%) precurosor solutions (10-100 μM). The electrochemical method involved a two-electrode setup in a teflon assembly (custom built in our laboratory) with 20-25 cm^3 electrolyte solutions. The sacrificial anode was a gold coated glass substrate and the cathode was H-Si (100). Deposition potentials from 100-600 mV were applied at the anode metal (relative to the cathode) using a model 366A Bi-potentiostat (Princeton Applied Research) for durations ranging from a few seconds to few tens of seconds.

Preparation of H-Si (100) and electrical contacts: n-type Si (100) substrates (antimony doped, Wafernet, Inc.) with resistivity of 0.1- 1.0 **Ω**-cm were washed in acetone, ethanol, and deionized water. Subsequently, HF treatment using a 1:5 (v/v) ratio of HF (48% EMD) and ethanol (95%, Sigma) was used to remove the oxide layer. A very thin layer of either Ti/Al (Ti 50 nm, Al 100 nm) or Cr/Au (Cr 15 nm, Au 100 nm) was then deposited using E-beam evaporation on the unpolished side, for making the electrical contact. The wafer was then cut using a die-saw into pieces of required size. Colloidal silver paint was used to make a contact between the E-beam evaporated metal on the backside and a thin platinum foil. As described previously, just prior to the electrochemical synthesis of Au nanocrystals, the native oxide layer on the polished side was again treated in HF. In the initial experiments, we used 5×10 mm^2 H-Si (100) substrates. After the electrochemical synthesis, the E-beam evaporated metal contacts were dissolved either in HF (same concentration as described earlier) for Ti/Al contact or aquaregia (1:3, HNO_3: HCl) for Au contact.

Synthesis of Si nanowires: Au nanocrystals with different mean diameters were used as catalysts for the growth of silicon nanowires. The nanowires were grown under conditions similar to those previously reported.[8,23] Nanowires containing samples were briefly sonicated in ethanol for about 30 seconds, and a droplet of this solution was dried on a carbon coated copper grid (Ladd Research) for TEM analysis.

Patterning of Si substrates

Oxide Patterning on Si: Low temperature silicon-dioxide (300 nm thick) grown on Si wafers in a CVD was received as a gift from Fitzgerald group (MIT). The wafers were cleaned in acetone, ethanol, and de-ionized (DI) water before being patterned. A very thin layer of hexamethyldisilane (HMDS) (MicroSi Inc.) was spin-coated on the polished side of the wafer just prior to spin-coating 500nm of Shipley S1805 photoresist (Rohm and Haas Electronic Materials LLC). The photoresist coated wafers were then exposed using a photoaligner (ABI, Inc.). Subsequently, the patterns were developed in MF 319 for 60 seconds and later etched using buffered HF (Transene Company, Inc.) until the Si surface could be clearly seen on the backside of the wafer. Just prior to the electrochemical synthesis of the Au nanocrystals, the native oxide was stripped again using HF (1:5 v/v in DI water for either 5 or 10 seconds).

Photoresist patterning on Si: The native oxide on Si was stripped using HF (1:5 v/v in DI water for 10 seconds) and the same procedure to that of oxide patterning was followed, except that after HF etching was not carried out after developing in MF319.

Gold nanocrystals were electrochemically synthesized on SiO_2 patterned Si substrates and photoresist patterned Si substrates and nanowires were grown from them under conditions similar to those of sample S3.

6.3 Results and Discussion

Au, Fe, Zn and Al nanocrystals on low surface energy n-type [H-Si (100)] substrates were synthesized from corresponding metal precursor solutions, usually dilute nitrate salts, except in the case of Au. The synthesis involved the electrochemical deposition of metal nanocrystals from dilute salt solutions at low deposition potentials under potentiostat conditions for durations ranging from a few seconds to a few tens of seconds. The overall process involved bulk metal oxidation at the anode and reduction of metal ions at the cathode to form metal clusters. Electrochemical growth of most metals on low energy substrates proceeds via the Volmer-Weber mechanism,[22] which is also commonly referred to as island type of growth. This kind of growth mechanism is encountered when the surface energy/unit area of the substrate (γ_s) is lower than the sum total of the interfacial energy/unit area between the substrate and the material being electrodeposited (γ_i) and the surface energy/unit area of the material being electrodeposited (γ_d), fig. 6.1a. n-type Si is likely to be the optimum choice, since electrodeposition on n-Si involves conduction electrons and the nucleation and growth are dependent on applied potential[12] and could be controlled externally. The goal of this work was to nucleate and grow these islands (3-D) with uniform size and shape, which are largely dictated by the deposition potential and the energetics of the system.

6.3.1 Electrochemical Synthesis and characterization of Metal nanocrystals on n-Si (100)

The process parameters that most greatly affect the nanoparticle size and density are the deposition potential, concentration of the electrolyte, deposition time and the temperature. Interparticle coupling has been cited as one of the primary reasons for the broadening of particle size distribution on low energy substrates such as graphite while employing an electrochemical method.[16] Therefore, the process parameters were optimized to achieve low nucleation density (to minimize interparticle coupling) and slow growth (to ultimately achieve low nucleation density with high crystallinity). Low deposition potentials (100-600 mV) and relatively low concentrations (10-100 μM) of electrolyte were, thus, used to mitigate the negative effects of interparticle coupling on the particle size distribution.

To understand the effect of deposition potential and electrolyte concentration, Au nanocrystals were synthesized at three different deposition potentials 200 mV (S1), 400 mV (S2) and 600 mV (S3) under otherwise identical conditions [20 sec and 50 μM] and at three different metal salt concentrations 50 μM (S2), 100 μM (S4) and 20 μM (S5) under otherwise similar conditions [20 sec and 400 mV]. Structural characterizations of the nanocrystals were conducted using AFM and TEM, and their chemical nature was confirmed using EDS. Representative AFM height images of various metal nanocrystals, including Au, Fe and Al, are shown in fig. 6.1. These results confirmed the Volmer-Weber growth of metal nanocrystals on the Si substrate. Extensive particle size distribution analysis was performed from the AFM height images, and the mean diameters of the Au nanocrystals were 19.3 ± 1.6 nm, 28.7 ± 2.0 nm, 48.7 ± 5.4 nm and 18.6 ± 1.4 nm for samples S1, S2, S3 and S5 respectively. Percent abundance in fig. 6.1 and elsewhere in this chapter is defined as the number of nanocrystals or nanowires with diameter in a particular range divided by the total number of nanocrystals or nanowires. In the case of sample S4, full coverage of nanocrystals on the substrate was observed. The distributions of nanocrystal diameters for samples S1 and S2 are presented in fig. 6.1. Particle size distribution analysis carried out on a large number of samples revealed that the standard deviation of the diameters of the nanocrystals varied from 6%-11%, which demonstrated good control over their size.

EDS spectra from sample S2 confirmed the chemical nature of the metal nanocrystals, fig. 6.2 a. The copper and silicon signals in the EDS spectra arose from the TEM grid and the substrate respectively. Antimony, the dopant in n-Si, was also observed in the spectra. The Au peaks arose from the nanocrystals.

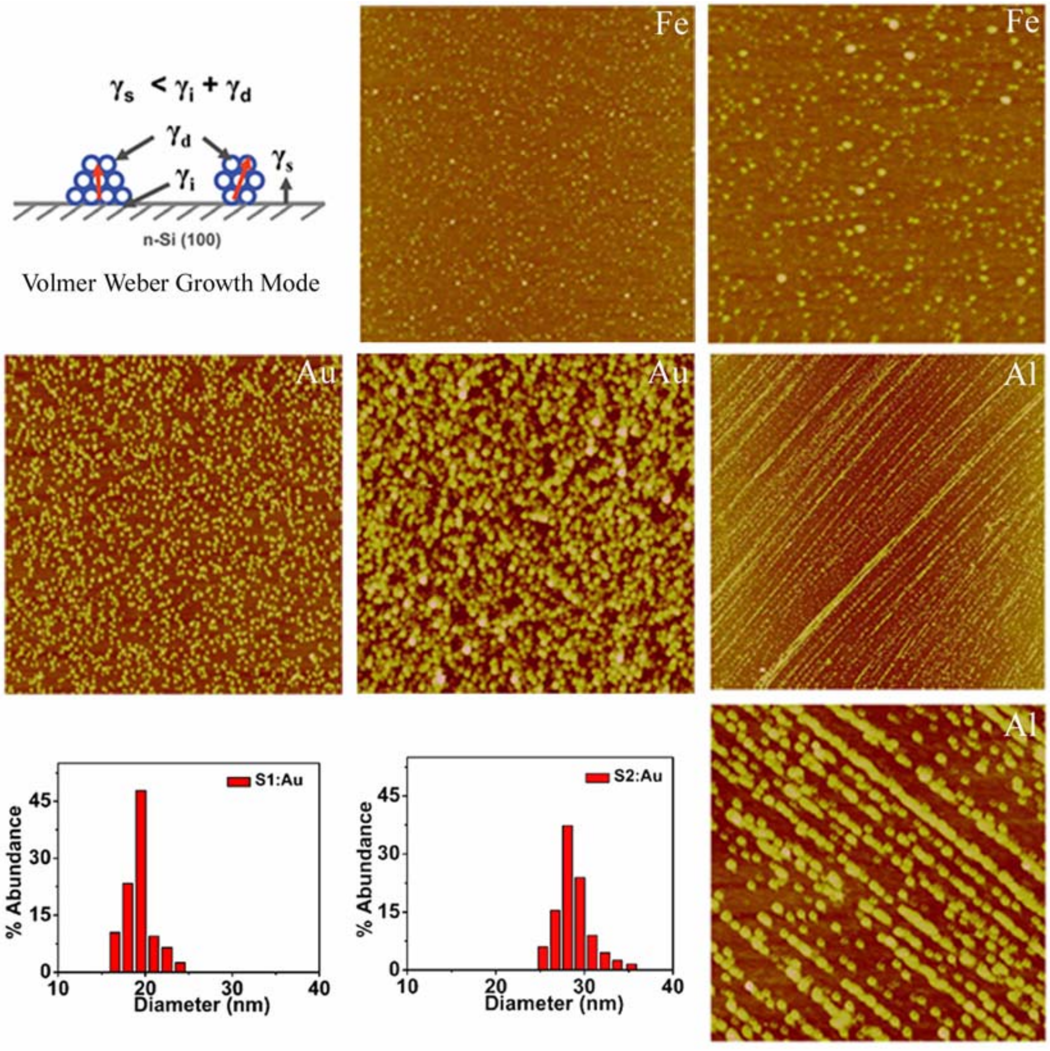

Figure 6.1: Electrochemical synthesis of metal nanocrystals on n-Si substrate. a. Schematic representation of Volmer-Weber growth mode b. AFM height images of Fe (each 9 μm^2), Au (each 6.25 μm^2) and Al nanocrystals (100 μm^2; 9 μm^2) on Si substrate c. Particle diameter distribution plots of the mean diameter of Au nanocrystals for samples S1 (19.3 ± 1.6 nm) and S2 (28.7 ± 2.0 nm) for samples sizes of over 200 particles.

Table 6.1: Electrochemical deposition process parameters and average diameters of resulting Au nanocrystals*

Sample	Deposition Potential (mV)	Concentration of $HAuCl_4.3H_2O$ (μM)	Deposition Time (seconds)	Average diameter of Au nanocrystals (nm)
S1	200	50	20	19.3 ± 1.6
S2	400	50	20	28.7 ± 2.0
S3	600	50	20	48.7 ± 5.4
S4	400	100	20	-
S5	400	20	20	18.6 ± 1.4

* the distance between the electrodes was maintained the same for all the samples (1 cm)

TEM analysis was carried out to examine the Au nanostructures on the Si substrates. In addition, cross-sectional TEM was carried out to understand the Au nanocrystal-Si interface and the 3-D shape of the nanocrystals. Plan (top) view and cross-sectional TEM images of Au nanocrystals at low magnification are presented in fig. 6.2. Figure 6.2 b (left) shows the plan view TEM image of Au nanocrystals synthesized at 100 mV for 20s using 20 μM salt concentration. The observed non-uniformity in the thickness of the underlying silicon substrate seen in the image is a result of ion milling that was performed during the TEM sample preparation. A higher magnification image of the Au nanocrystals from the same sample demonstrated the monodispersity in their size and shape, (fig. 6.2 b, right). A cross-sectional TEM image (XTEM) confirmed the Volmer-Weber type of growth and provided clear details of the Au–Si interface as well as the shape of the Au nanocrystals, fig. 6.2 c. Growth of Au nanocrystals directly on the Si substrate was confirmed by the absence of an oxide layer between the two. A thin oxide (SiO_x) layer seen in the image was a result of the oxidation of silicon upon exposure to air after the electrochemcial synthesis. Additional XTEM images revealing the crystallinity of the nanoparticles and the underlying substrate are shown in fig. 6.3

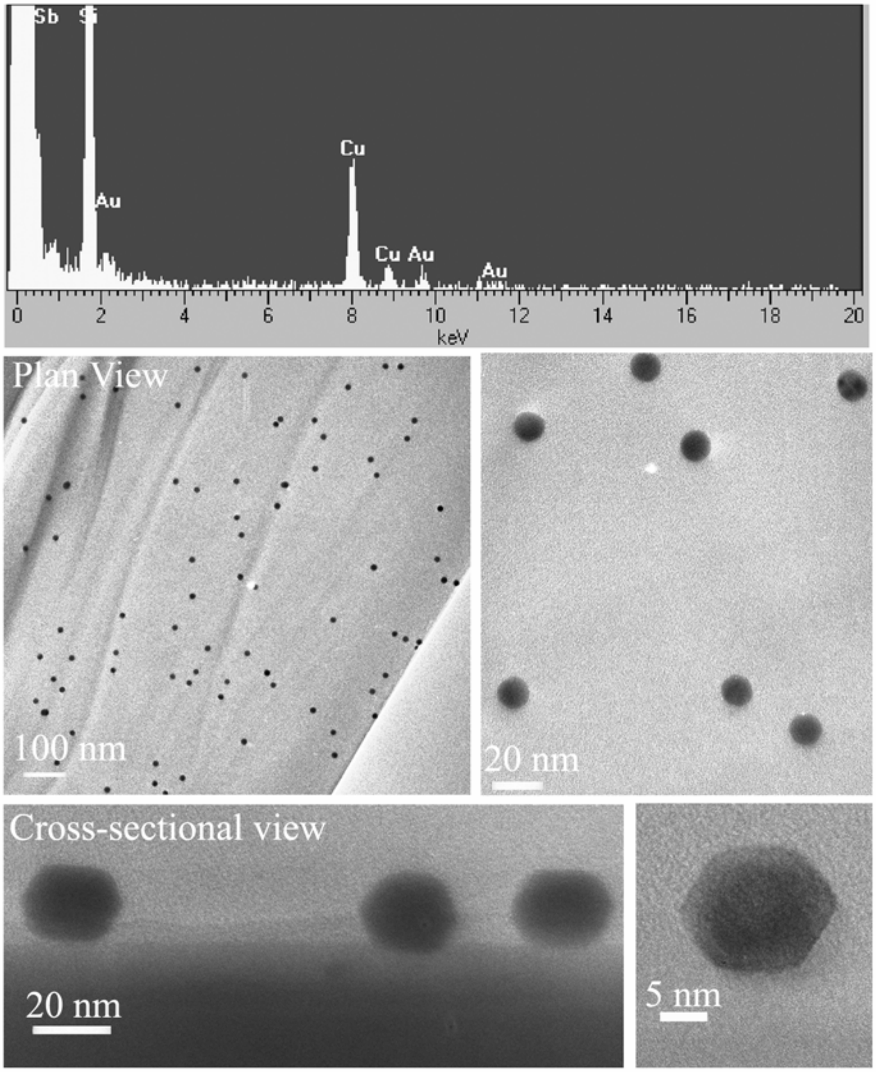

Figure 6.2: (a) EDS spectra from sample S2, obtained on a JEOL 2010 using a fine electron probe of 25 nm. The Cu peaks come from the TEM grid and the Si and Sb (n type dopant in Si) peaks come from the underlying substrate respectively. The Au peaks arise from the nanocrystal (b) Low magnification plan view TEM image (left) showing monodisperse 12.5 nm Au nanocrystals on Si substrate. A higher magnification plan view TEM image (right) from the same sample confirmed the size and shape monodispersity. (c) Cross-sectional TEM images of ~ 20 nm Au nanocrystals on Si substrate (not from the same sample shown above), confirmed the Volmer-Weber growth of Au nanocrystals directly on Si substrate.

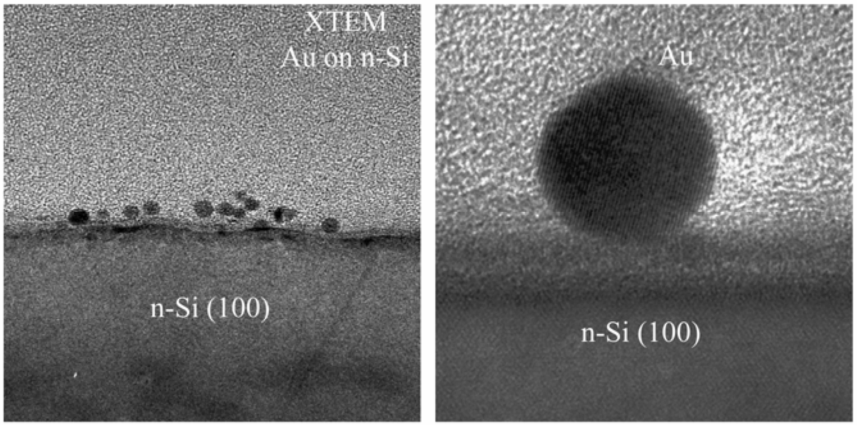

Figure 6.3: Additional cross-sectional (XTEM) images of Au nanocrystals on Si (100). Lattice fringes of the nanocrystal as well the lattice of the underlying Si are clearly seen in the XTEM image (above, right).

High resolution plan view TEM images of the nanoparticles revealed their crystalline nature as well as their shape. The lattice fringes of the nanocrystal and the underlying Si substrate are clearly seen in these images, fig. 6.4 a and b. Fast Fourier transform images from the center of the nanocrystal and Si substrate in fig. 6.4 b are also shown (fig. 6. 4c and d). The measured d-spacing of 2.33 Å for the Au nanocrystal agrees closely with that of the {111} plane (actual value 2.35 Å). The equilibrium shape of the Au nanocrystal is a truncated octahedron with the (111) and (100) facets, which is roughly the Wulff[24] construction shape of a free particle in two dimensions for the $[\bar{1}10]$ orientation of a face centered cubic (FCC) single crystal. The 2D equilibrium Wulff plot of a 'free particle' for a <110> section of a FCC single crystal and the reconstructed shape of the Au nanocrystal on Si (100) based on the cross-sectional TEM observations are shown in fig. 6.4 e and 6.4 f, respectively. From these results, it was inferred that the minimization of surface energy plays a dominant role in influencing the shape of the nanocrystal on n-Si (100).

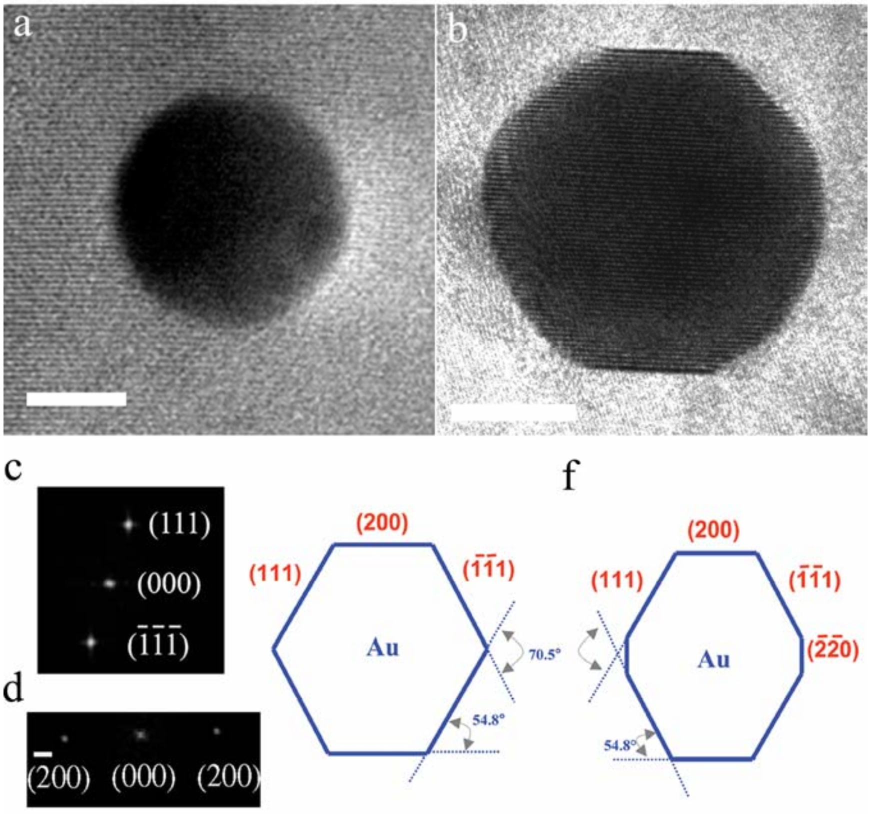

Figure 6.4: High resolution plan (top) view TEM data provided insight about the orientation and 3D shape of Au nanocrystals. (a) HRTEM image of a 12.5 nm Au nanoparticle (scale bar 5nm) (b) HRTEM of a nanocrystal imaged at 800,000X clearly showing the (111) and (100) facets (scale bar 5nm); (c and d) are the FFT images from the centre of the nanocrystal and Si substrate, respectively (e) 2D equilibrium Wulff construction plot of a free particle for the <110> orientation of a FCC single crystal (f) Truncated octahedron shape for the Au nanocrystal showing the additional <110> facets (shape of nanocrystals had been reconstructed, based on the TEM observations).

Different Au nanocrystals on the Si substrate can have different orientations (shown by red arrows, fig. 6.1 a). However, the orientations are not random, but are dictated by the energetics of the system, which are size dependent. The process is governed by the minimization of one or more of the following energies: interfacial energy between the nanocrystal and the Si substrate; surface and strain energies of the Au nanocrystal; surface energy of the Si substrate; and the associated strain energy at the interface (see fig. 6.1 a). For small nanocrystals, the surface area to volume ratio is higher, and the minimization of surface energy plays a crucial role. The equilibrium shape is not necessarily that of a minimum surface area. It may be a complex polyhedron, with the necessary condition for minimum surface energy given by the equation $\int_A \gamma(hkl)dA =$ **minimum;** where γ (hkl) refers to the surface energy of the nanocrystal as a function (hkl) plane and *dA* is the associated surface area. For face centered cubic metals such as Au, {111} planes have the lowest surface energy and interfacial energy due to dense packing and are likely to be the preferred planes. Moreover, for Au, $\gamma(111) < \gamma(100) < \gamma(110)$. The TEM analysis of our 10-30 nm nanocrystals reveals the presence of (111) and (100) facets, suggesting that the surface energy minimization of the nanocrystals plays a dominant role. As the nanocrystal size increases, the strain effects associated with a lattice mismatch between Au and Si increase and are likely to play a critical role and an orientation that results in minimization of strain energy may be observed.

Interesting observations were made during the TEM investigations. Figure 6.5 shows of coalescence of two discrete Au nanocrystals which were present in close vicinity, various stages of the process. The coalescence is presumably due to high incident energy of the electron beam that resulted in solid state diffusion of Au atoms on the surface of the Si substrate. It is also interesting to note that the crystallinity of the nanoparticles was conserved during the whole process that lasted few minutes.

6.3.2 Catalyst-assisted VLS growth of Si nanowires

To understand the size-dependent growth of inorganic semiconducting nanowires from the above size controlled Au nanocrystals, different sizes of Au nanocrystals (S1: 19.3 ± 1.6 nm, S2: 28.7 ± 2.0 nm) were employed as catalysts. The investigations in this work have focused primarily on the synthesis of Si nanowires.

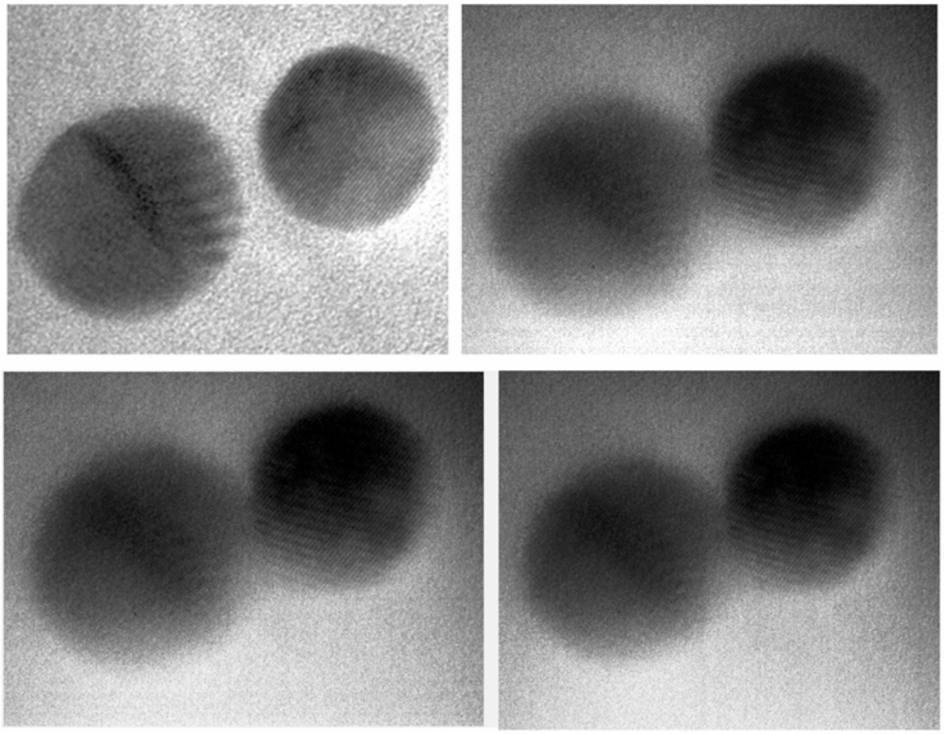

Figure 6.5: Coalescence of two Au nanocrystals by diffusion due to high energy electron beams during TEM observations was noticed.

SEM data of nanowires grown from samples S1 revealed the high catalytic yield of Au nanocrystals, figs. 6.6 a and b. The nanowires observed in these images were straight that indicated their crystallinity which were further corroborated by high resolution TEM data. TEM data from samples S1 and S2, revealed the highly crystalline nature of the wires (figs. 6. 6 c and d). The lower inset in fig. 6.6 d shows the complete nanowire along its diameter. A thin oxide shell encapsulating the single crystalline cores can be seen in these images.

Catalyst assisted growth of Si NWs from Au nanocrystals proceeds via vapor-liquid-solid (VLS) method which was originally developed by Wagner in 1960.[6] A typical growth via VLS involves, first, dissolution of gaseous reactants, for example SiH_4 in this case, in metal nanoparticles/clusters (Au) which usually form a eutectic alloy (Au-Si in this case) that serves as a seed for nucleation. As the concentration of Si in the Au nanoparticle increases and supersedes the supersaturation limit, Si precipitates in the form of a crystalline nanowire or rod. The diameter of the nanowire is dependent on the initial size of the metal nanoparticle which remains roughly the same during the entire growth process.

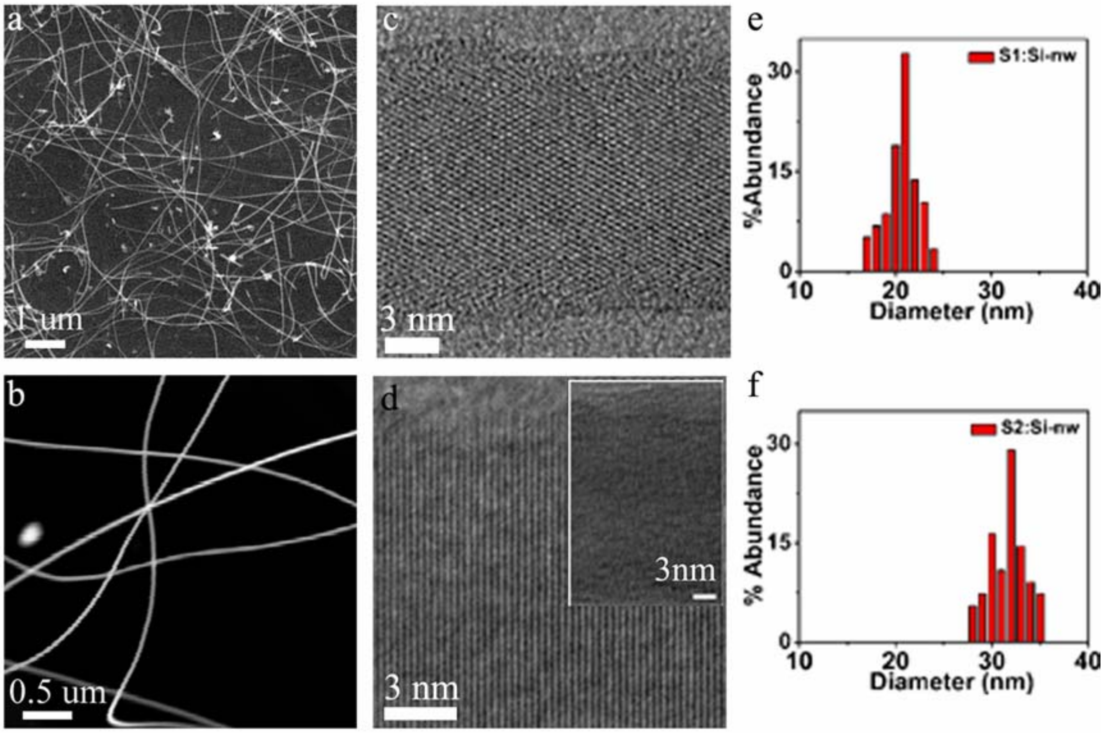

Figure 6.6: Diameter-controlled growth of Si nanowires from size controlled Au nanocrystals on n-Si substrate. (a and b) SEM images of Si nanowires grown from Au nanocrystals. HRTEM images of nanowires from samples S1-(c) and S2-(d). The inset in (d) shows the complete nanowire along its diameter. Diameter distributions of the Si nanowires grown from Au nanocrystals in samples S1 (e: 20.7 ± 1.9 nm) and S2 (f: 31.4 ± 2.3 nm).

Extensive TEM analysis was carried out to estimate the diameters of the nanowires. The diameter distributions of nanowires from samples S1 and S2 are presented figs. 6.6 e and f. As measured, the diameters of the nanowires also included the thin amorphous oxide shell covering the single crystalline silicon core. The mean diameters of the nanowires for samples S1 and S2 were 20.7 ± 1.9 nm and 31.4 ± 2.3 nm, respectively. The differences between the diameters of the nanowires and the nanocrystals from which they were grown could be attributed to: (1) the alloy (Au-Si) that forms during nucleation prior to growth is slightly larger than the catalyst particle (actually depends on the supersaturation level of Si in the Au catalyst particle); and (2) post growth oxidation of Si upon exposure to air results in the formation of a thicker oxide layer.[8,25,26] The percent standard deviation of the mean diameters of the nanocrystals and nanowires were relatively small (8.3% and 9.2%, respectively for sample S1; 6.9% and 7.3%, respectively for sample S2). The similarity in the diameter distributions of the Au nanocrystals and the Si nanowires grown from them confirmed the diameter-controlled growth of the nanowires.

6.3.3 Synthesis of Si nanowires from patterned Au catalysts on Si (100)

The ability to pattern the nanocrystals during growth or otherwise is important for many device applications, and this synthesis route presented here offered great promise. Gold nanocrystals were electrochemically synthesized on SiO_2 patterned Si substrates and nanowires were grown from them under conditions similar to those of sample S3. The sizes of the patterned features ranged between 1-250 μm. Nanowires grown from Au nanocrystals on oxide patterned Si substrates are presented in fig. 6.7 a and d. Figures 6.7 a and b show the bare oxide pattern on Si and the corresponding region after the electrochemical synthesis of Au nanocrystals and growth of Si nanowires. The white regions in fig 6.7a correspond to the thick silicon oxide layer and the dark regions correspond to Si only regions. Synthesis of Au nanocrystals on these substrates is restricted to Si regions alone, due to its conductivity, unlike the oxide regions that serve as insulators. Employing these patterned Au catalysts yielded pre-defined growth of Si nanowires along these patterns.

Electrochemical synthesis of Au nanocrystals was also performed on photoresist patterned Si substrates. The photoresist was unaffected under the electrochemical synthesis conditions neither by the electrolyte nor by the applied potential. The photoresist was stripped using acetone after the synthesis of Au nanocrystals. Au nanocrystals and Si nanowires were grown under conditions similar to those of sample S3. There was no noticeable difference between the nanowires grown on these patterned substrates (figs. 6.7 e and f) and those grown on the oxide-patterned Si substrates. These results demonstrated that Au nanocrystals grow only on the Si region, enabling synthesis of nanocrystals on pre-defined patterns on the substrates.

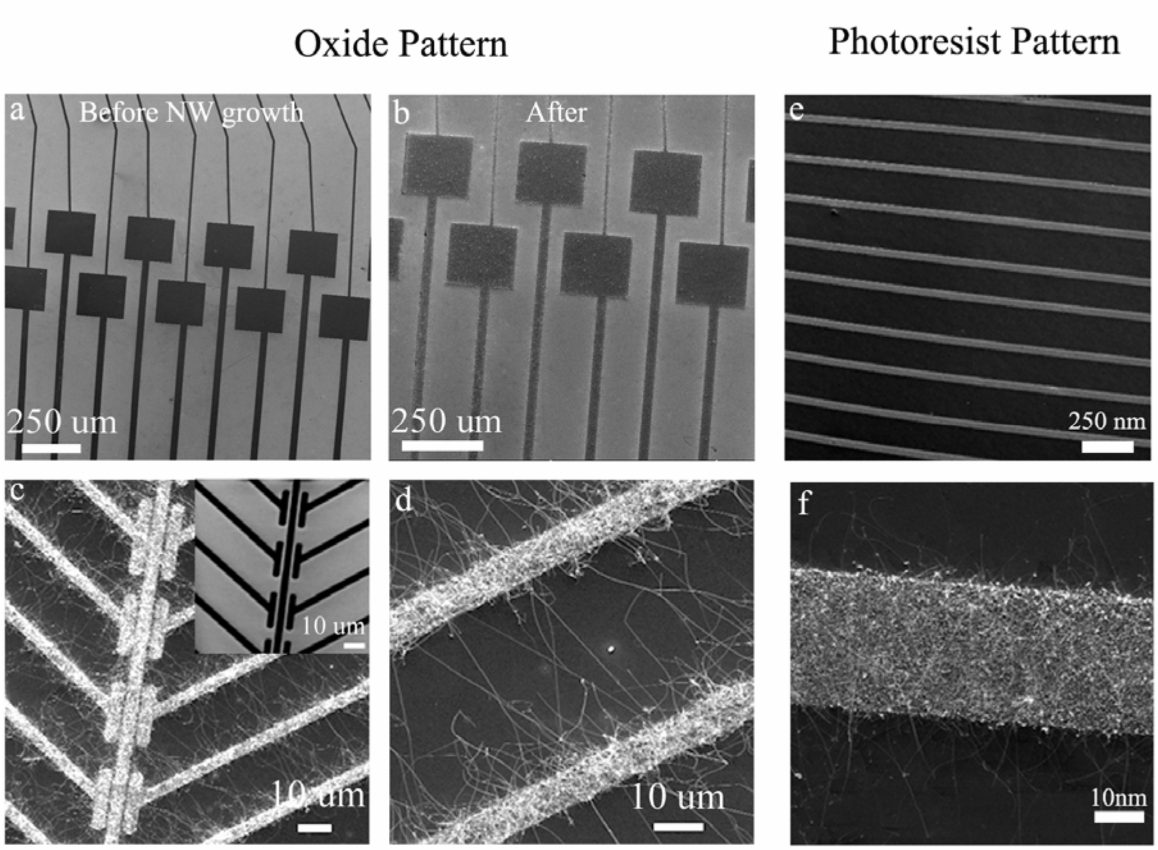

Figure 6.7: SEM images showing growth of Si nanowires from Au nanocrystals synthesized on patterned substrates. Electrochemical synthesis of Au nanocrystals takes place only on Si and thus the nanowires appear on these regions alone (d) Higher magnification image, shows the absence of nanowires on oxide regions and further confirms Au nanocrystal growth on the Si region alone. Electrochemical synthesis of Au nanocrystals on photoresist patterned Si substrates and subsequent growth of silicon nanowires grown from them

6.4 Summary

In summary, size- and shape- controlled synthesis of Au nanocrystals on n-Si (100) substrate by an electrochemical method is demonstrated. The most salient feature of the method, as demonstrated in this work, is the ability to control the nanocrystal growth by one or more of the process parameters. Using size-controlled Au nanocrystals as catalysts resulted in the diameter-controlled growth of silicon nanowires. TEM analysis indicated orientation preference for the as grown Au nanocrystals on Si (100) that can be explained in terms of the surface, interfacial and strain energetics of the system. The synthesis of nanocrystals with same orientation on the substrate might enable control over the orientation of as grown nanowires and the chirality of the carbon nanotubes. Controlled growth of Au nanocrystals on pre-defined patterns on the substrates further demonstrated the versatility of the electrochemical technique. Given the widespread acceptance of the electrochemical processes for fabricating Cu interconnects, it may be easier to integrate the process with the microelectronics industry for the hierarchical growth of diameter-controlled semiconducting nanowires and carbon nanotubes from size-controlled metal nanocrystals on Si substrates.

References

1. M. Fuhrer, H. Park, P.L. McEuen *IEEE Trans. on Nanotech.* **2002** ***1***, 78

2. R. Martel, T. Schmidt, H. R. Shea, T. Hertel, P. Avouris *Appl. Phys. Lett.* **1998** *73*, 2447

3. S-W. Chung, J.Y. Yu, J.R. Heath *Appl. Phys. Lett.* **2000** *76*, 2068

4. Y. Cui, X. Duan,; C.M. Leiber *J. Phys. Chem. B* **2000** *104*, 5213

5. Y. Xia, P. Yang, Y. Sun, Y. Wu, B. Mayers, B. Gates, Y. Yin, F. Kim, H. Yan *Adv. Mater.* **2003** *15* (5), 353

6. R. S. Wagner, W. C. Ellis *Appl. Phys. Lett.* **1964** *4*, 89

7. E. I. Givargozov *J. Cryst. Growth* **1975** *31*, 20

8. Y. Cui, L. J. Lauhon,; M.S. Gudiksen, J. Wang, C. M. Lieber *App. Phys. Lett.* **2001** *78*, 2214

9. X. Duan, C. M. Lieber *Adv. Mater.* **2000** *12*, No.4, 298

10. C. B. Murray, C. R. Kagan, M. G. Bawendi *Annu. Rev. Mater. Sci.* **2000** *30*, 545

11 M. C. Daniel, D. Astruc *Chem. Rev.* **2004** *104*, 293

12 J. OM. Bockris, A. K.N. Reddy, *Modern Electrochemistry*, Vol. 2, Plenum Press, New York **1970**

13. M. T. Reetz, W. Helbig *J. Am. Chem. Soc.* **1994** *116*, 7401

14. L. Rodriguez-Sanchez, M. C. Blanco, M. A. Lopez-Quintela *J. Phys. Chem. B* **2000** *104*, 9683

15. J. V. Zoval, R. M. Stiger, P. R. Biernacki, R. M. Penner *J. Phys. Chem.* **1996** *100*, 837

16. J.V. Zoval, J. Lee, S. Gorer, R. M. Penner. *J. Phys. Chem. B* **1998** *102*, 1166

17. H. Liu, R. M. Penner *J. Phys. Chem. B* **2000** *104*, 9131

18. G. Oskam, P. C. Searson *Surf. Sci.* **2000** *446*, 103

19. P. Allongue, E. Souteyrand *J. Vac. Sci. Techonol. B* **1997** *5*, 1644

20. G. Oskam, D. V. Heerden, P. C. Searson *Appl. Phys. Lett.* **1998** *73*, 3241

21. R. Stiger, B. Craft, R. M. Penner *Langmuir* **1999** *15*, 790

22. M. Volmer, A. Weber *Z. Physik. Chem.* **1926** *119*, 277

23. G. Zheng, W. Lu, S. Jin, C. M. Lieber *Adv. Mater.* **2004** *16*, 1890

24. G. Wulff *Zeitschrift feur Kristallographie und Mineralogie.* **1901** 34, 449

25. A. I. Hochbaum, R. Fan, R. He, P. Yang *Nano Lett.* **2005** *5*, 457

26. T.Y. Tan, N. Li, U. Gosele *App. Phys. Lett.* **2003** *83*, 1199

Chapter 7

On-going work and Future Directions

In this chapter, suggested directions for future work related to experiments discussed in chapter 3 are presented. Directions for future work based on experiments related to III-nitrides are presented in section 4.5

1. Syntheses of metal nanoparticles (mono-metallic and bi-metallic) using block-copolymer templates in this study were restricted to those metals which could potentially be employed as catalysts for the growth of 1-D nanoscale materials, including carbon nanotubes and silicon nanowires. The BCP method could be further extended to the synthesis of other transition metals, in particular, f-block metallic elements such as Gd, Eu, etc., which possess interesting magnetic properties. In addition, investigations on the syntheses of bi-metallic nanoparticles of f-block elements as well as doping in the nanoparticles may further unravel their fundamental physical properties (associated with the nanoparticles).

   Challenges- even though, in principle, it may be relatively easier to synthesize these different metal nanoparticles on substrates using the BCP method, one has to keep in mind the deleterious effects that arise as a result of the oxidation of metal nanoparticles upon exposure to air or O_2 plasma during their synthesis that eventually influence their physical properties. These challenges are also associated with most other synthesis methods, nonetheless, it should be noted for this method as well.

2. A linear chain of noble metal nanoparticles exhibits interesting optical properties, namely,

effects related to the surface plasmon.[1-2] To date, there have been few investigations on the fabrication of 1-D arrays of metal nanoparticles, most of which are either based on e-beam lithography or reactive-ion milling and these techniques are relatively difficult and expensive.[3-4] In summary, synthesis of linear chain of metal nanoparticles have been limited by the absence of reliable, inexpensive and large scale fabrication techniques. A method based on block-copolymers may provide a facile route for the synthesis of chains of metal nanoparticles. As described earlier, the block-copolymer micelles in solution consist of polar vinyl pyridine core encapsulated in non-polar PS domains/shells. A polymer with two reactive ends that polymerizes with PS could be used as a linker to connect two polymer micelles (see figure below) eventually resulting in the formation of a chain of polymer micelles that could be further used as a template for the fabrication of chains of metal nanoparticles. The chain length of the intermediate polymer may also be used varied to manipulate the distance between the two adjacent polymer micelles.

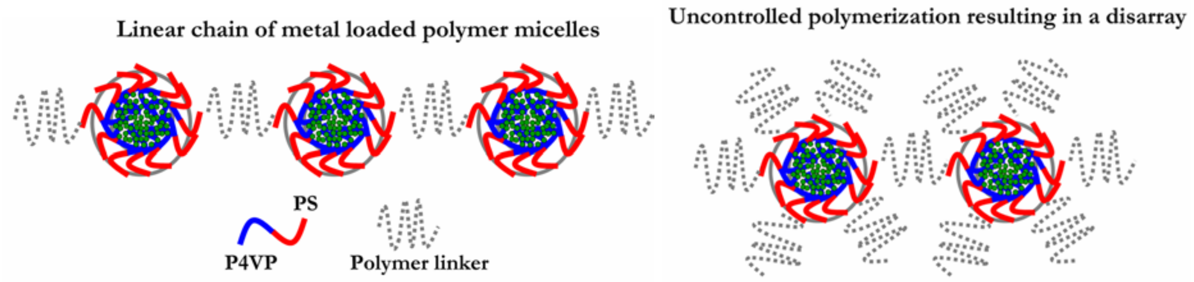
Linear chain of metal loaded polymer micelles

Uncontrolled polymerization resulting in a disarray

Figure 7.1: Schematic showing linear arrays of nanoparticles synthesized using (a) controlled polymerization between PS and linker polymer (b) uncontrolled polymerization resulting in a disarray.

Challenges: While the method described is appealing, one has to optimize the process conditions to avoid uncontrolled polymerization that could result in the formation complex nanostructures, see figure above (right).

3. Many investigations on the physical properties, including, magnetic and optical properties, based on the size and shape of metal nanocrystals have already been extensively reported. But most of these investigations are based on a statistically large numbers of nanoparticles in disordered arrays.[5-6] It would be interesting to examine the physical properties of ordered arrays (both 1-D and 2-D arrays) of monodisperse nanoparticles for the following reasons. For example, in the presence of an external electromagnetic field, the local electromagnetic response associated with individual nanoparticles in ordered arrays can either interfere constructively or destructively, giving rise to attractive new effects. More importantly, properties of such nanoparticles with sizes in the range of 1-5 nm have not been extensively reported. Magnetic properties of arrays of monodisperse metal nanoparticles, especially, with 1-5 nm sizes, provide an exciting prospect to study the size effects on their magnetic properties, for example, super paramagnetic effects on these nanoparticles. An interesting way to synthesize linear arrays of metal nanoparticles based on functionalization of the polar singularities of ordered monolayers has been recently reported.[7]
4. Applications: Plasmon effects of arrays of metal nanoparticles could be utilized for improved detection (in terms of sensitivity) of fluorescently labeled biomolecules.

Understanding molecular structure, function and dynamics of biological molecules is imperative for gaining further knowledge about molecular biology. In addition to refining methods that are currently available, this further entails the need for new detection tools as well as new strategies. High-resolution methods, such as NMR and X-ray crystallography, have provided a vast array of structural details for biological molecules, yet, these detection methods are limited by static molecular view and ensemble averaging. Single molecule methods provide alternate set of approaches to a more direct view of the action of individual molecules without the need to infer processes or functions from static structures. Quantum dot based detection methods have led to significant advances, yet are not free from drawbacks, some of which include low quantum yield and toxicity. Single-molecule detection methods may not only lead to advances in furthering the understanding, but also may play a significant role in furthering molecular diagnostics. A proposal for single molecule detection based on localized surface plasmon resonance of noble metal nanoparticles (2 nm< diameter < 30 nm) is discussed here. Arrays of noble metal nanoparticles with sizes greater than 2 nm might enable single molecule detection and may also enable in improving the current detection limits of single molecules based on Raman spectroscopy.[8] Few theoretical investigations[1-2] have been reported on the optical properties of 1-D arrays of noble metal nanoparticles and fewer experimental investigations have been reported thus far.[3-4] Following is a brief summary of the important properties that will be utilized for single molecule detection (see fig. 7.2)

(i) Property A- metal nanoparticles in close vicinity interact through their electromagnetic field which results in the electric field enhancement that is at least higher by four orders of magnitude (10^4-10^9), see fig. 7.2b. In other words, this means that the number of photons available for fluorescence is higher as compared to any other conventional systems, including quantum dots.

(ii) Property B- the linear chain of nanoparticles essentially behaves as a plasmon waveguide where in the electromagnetic energy transfer takes place from one nanoparticle to another below the diffraction limit, see fig. 7.2c.

Principle of Detection: The proposed system consists of 1-D arrays of noble metal nanoparticles on substrates and single molecules that are labeled using dyes or fluorescent molecules in a solution. One end of the chain of the nanoparticles is excited using a near-field scanning optical microscope (NSOM) tip which excites the plasmon waveguide.

The waveguide transports the electromagnetic energy (property B) to a fluorescent nanosphere (which is in between or near any two nanoparticles), and the fluorescence intensity is detected in the far field using NSOM or other detection techniques which are already available for measuring fluorescence, see fig. 7.2d. The observed intensity would be higher in this case because of the local enhancement in electric field (property A) between or near any two nanoparticles, which increases the efficiency of the fluorescence by making available a large number of photons to the whole process and making single molecule detection possible. It may also be possible to detect optically detect the fluorescence event during the excitation using an optical microscope.

One of the limitations of the above method in its current form is that solution based detection is difficult because the chain of nanoparticles must be laid on the substrate for exciting one end of the chain using NSOM tip. However, this limitation can be overcome by using the above proposed method in conjunction with Raman spectroscopy. (Surfaced enhanced Raman spectroscopy has been extensively investigated on thin metal surfaces in the past two decades- the advantage being that the presence of metal surface increases the detection limits as well as the intensity of the signal by a couple of orders of magnitude.)

5. The BCP templates might also enable regular patterning of peptides/proteins on various substrates. Interactions between the active sites of the biomolecules with the pyridine units may be used to sequester them into the core of the micelles. It need not necessarily be PS-PVP based di-block copolymer system, but could involve polymers that are more compatible with biomolecules, such as PMMA, etc.
6. Use these metal nanoparticles as catalysts for the growth of semi-conducting nanowires (for example, III-nitrides nanowires). There have not been many reports on III-N nanowires in the size range of 1-5 nm! For a matter of fact, initial experiment had already been

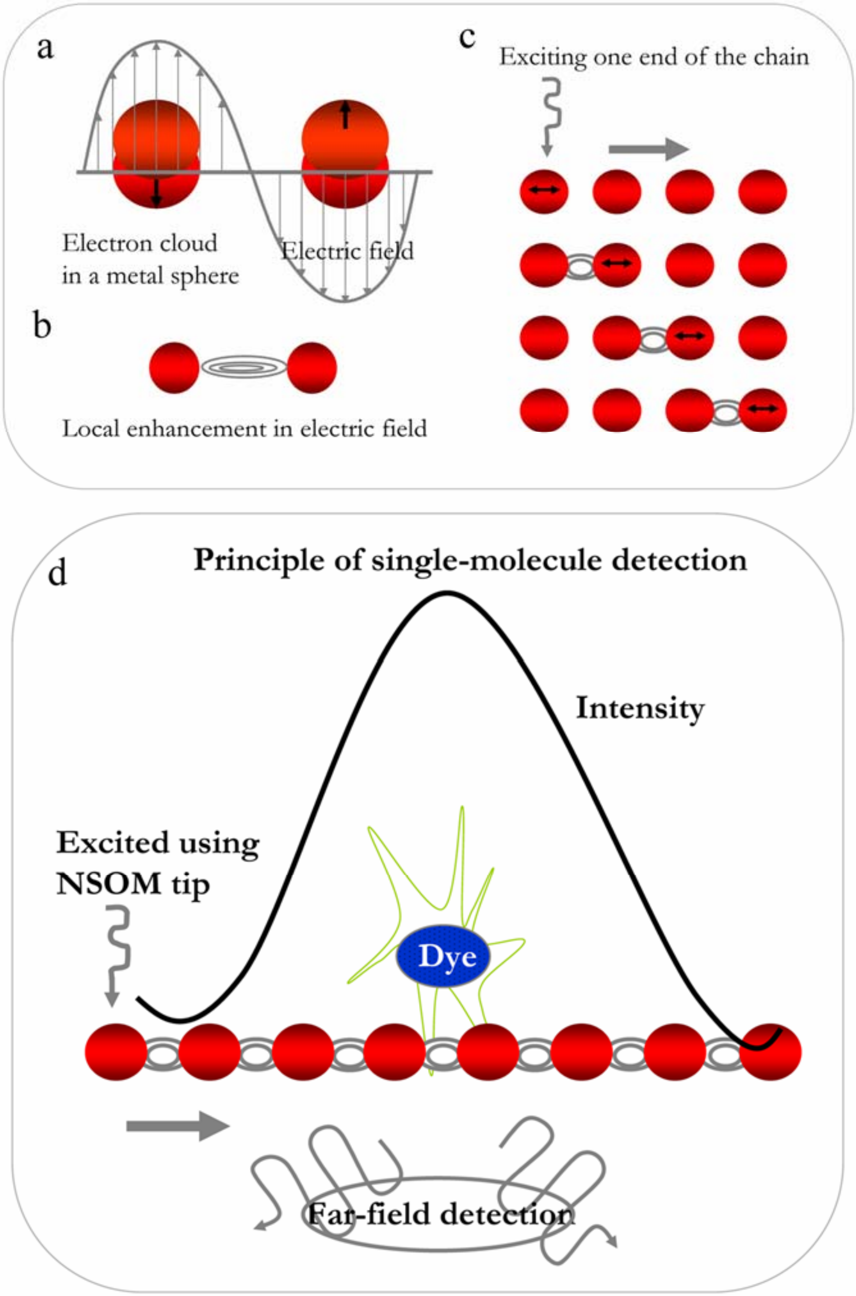

Figure 7.2: Optical properties of noble metal nanoparticles and principle of single molecule detection. (a) Displacement of electron cloud relative to the nuclei gives rise to surface plasmon (b) Interaction between two metal nanoparticles in close proximity resulting in the enhancement of local electromagnetic field (property A) (c) Transfer of electromagnetic energy from one particle to another below the diffraction limit (property B) (d) Light emanating form the NSOM tip locally excites the Plasmon waveguide, which transports the electromagnetic energy to a fluorescent molecule attached to a single molecule, and the fluorescent intensity is detected in the far field.

successfully conducted and the results are mentioned in Chapter 4 - 'GaN nanowires' section.

7. To date, there aren't any reliable investigations directly comparing the efficacy as well as the catalytic activity of different metal nanoparticles for the growth of either nanowires or nanotubes. To make reliable comparisons on the catalytic activity of nanoparticles, it is not only important to have identical size distributions, but also identical densities of nanoparticles on the substrate. The biggest impediment so far has been the lack of synthesis method that enables simultaneous control over their size as well as the density of the nanoparticles on the substrate. Metal nanoparticles synthesized using the BCP technique offer a perfect foundation for implementing such examinations.

References

[1] Brongersma M, Hartman J H, Atwater H A *Phys. Rev. B* **2000** Vol *62* No. 24, R16356-R16359.

[2] Maier S A, Kik P G, Atwater H A *Phys. Rev. B* **2003** *67*, 205402

[3] Sweatlock L A, Maier S A, Atwater H A *Phys. Rev. B* **2005** *71* 235408

[4] Rechberger W, Hohenau A, Leitner A, Krenn J R, Lamprecht B, Aussenegg F R *Opt. Comm.* **2003** *220*, 137 (two Au particles Austria paper)

[5] Kelly K L, Coronado E, Zhao L L, Schatz G C *J. Phys. Chem. B* **2003** *107*, 668

[6] El-Sayed M *Accts. Chem. Res.* **2001** *34* No. 4, 257

[7] DeVries G A, Brunnbauer M, Hu Y, Jackson A M, Long B, Neltner B T, Uzun O, Wunsch B H, Stellacci F *Science* **2007** *315,* 358

[8] Moerner W E, Fromm D P, *Rev. of Sci. Instr.* **2003** *74* (8) 3597

Appendix-I

Crystal Structures and Lattice Constants Of Metallic Elements and Compounds

Table: Crystal Structure of elements and few compounds

Element/Compound	**Crystal Structure**	**Lattice Constants**	
		a (°A)	**c (°A)**
Si	**Diamond Cubic**	**5.430**	
Fe	**BCC (T< 727 °C)**	**2.87**	
Co	**HCP**	**2.51**	**4.07**
Ni	**FCC**	**3.52**	
Mo	**BCC**	**3.15**	
Au	**FCC**	**4.08**	
Re	**HCP**	**2.76**	**4.46**
Eu	**BCC**	**4.58**	
GaN	**Wurtzite**	**3.189**	**3.548**
InN	**Wurtzite**	**5.185**	**5.760**

References

[1] Kettle C, Solid State Physics, Wiley & Sons Publishers.

[2] Maruska H P; Tietjen J J, *Appl. Phys. Lett* **1969** *15*, 327

[3] Zetterstrom R B, *J. Mater. Sci.* **1970** *5*, 1102

Appendix-II

Opto-electronic properties of bulk GaN

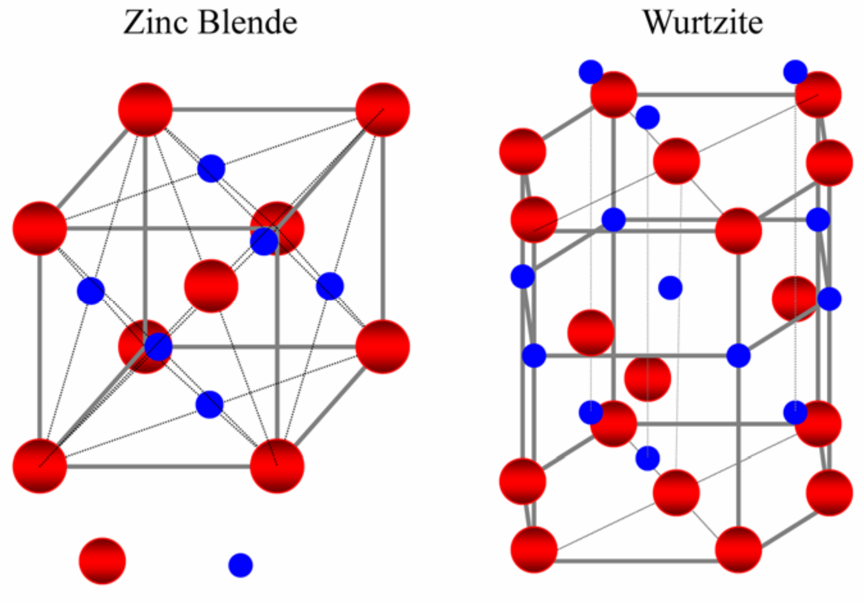

Figure: Illustration showing the Zinc Blende and Wurtzite crystal structures. The dashed lines do not represent coordination.

Table: Bandgap of bulk GaN with Zinc Blende and Wurtzite crystal structures

Type of Crystal Structure	Band gap at 0 K (E_{g0}) (in eV)	Band gap at 300 K (E_g) (in eV)	Band gap at any temperature (in eV)
Zinc Blende	3.28	3.2	$E_g = E_{g0} - 7.74\times10^{-4}\times T^2/(T+600)$
Wurtzite	3.4751	3.44	

Table: Properties of wurtzite and zinc blende III-nitrides

	GaN		**InN**	
	Wurtzite	**Zinc Blende**	**Wurtzite**	**Zinc Blende**
Band gap (E_g) (300 K)	**3.39 eV** [ref 2]	**3.2 - 3.45 eV** [ref 2]	**1.89 eV** [ref 3]	**2.2 eV** [ref 6] **1.8-2.1 eV** [ref 7] **0.7-1.1 eV** [ref 8]
dE_g/dT	**-6×10^{-4} eV/K** (T> 180); [ref 2]	–	**-1.8×10^{-4} eV/K** [ref 1]	–
Lattice constant	**a = 3.189 ºA** **c = 5.185 ºA** [ref 2]	**a = 4.5 ºA** [ref 4]	**a = 3.548 ºA** **c = 5.760 ºA** [ref 3]	**a = 4.98 ºA** [ref 5]

References

[1] Slack G A; McNelly T F, *J. Crystal Growth* **1976** *34*, 263

[2] Maruska H P; Tietjen J J, *Appl. Phys. Lett* **1969** *15*, 327

[3] Zetterstrom R B, *J. Mater. Sci.* **1970** *5*, 1102

[4] Strite S; Ruan J; Li Z; Manning N; Salvador A; Chen H; Smith D J; Choyke W J; Morkoc H, *J. Vac. Sci. Technol. B* **1991** *B 9*, 1924

[5] Strite S; Ruan J; Smith D J; Sariel J; Manning N; Choyke W J; Morkoc H, *Bull. APS* **1992** *37*, 346

[6] Jenkins D W; Hong R D; Dow J D, *Superlatt. Microstruc.* **1987** *3*, 365

[7] Yodo T; Yona H, Ando H, Nosei D, Harada H, *Appl. Phys. Lett.* **2002** *80*, 968

[8] Xu K; Yoshikawa A, *Appl. Phys. Lett.* **2003** *83*, 252

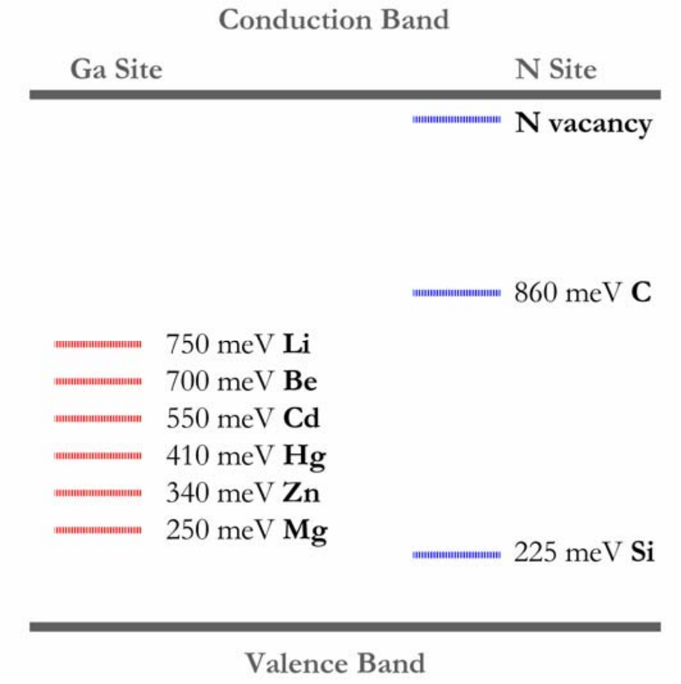

Figure: Estimated binding energies of some substitutional acceptors in GaN. A shallow donor, which is generally thought to be a nitrogen vacancy, is also shown.

Appendix-IIIa

Brief Introduction to SWNTs

Basics of Carbon Nanotubes (CNTs): The remarkable opto-electronic properties of SWNTs arise from the unusual electronic structure of the 2-D material, graphene, which is considered to be its parent material. It is conventional in solid state physics, or for that mater in materials science, to understand the physical properties of nanoscale materials starting from their parent material. A single atomic layer of graphite is referred to as graphene; it consists of sp^2 bonded carbon atoms in a 2D honeycomb structure. The band structure of graphene is, in and itself very interesting, and is characterized by conducting states at E_f only at the corners of first Brillouin zone (FBZ) in the momentum space but has a finite band gap elsewhere in the momentum space. As a consequence, metallic character is observed at the corners of the FBZ and semiconducting character at all other regions in the momentum space. Hence, graphene is also occasionally referred to as a semi-metal.

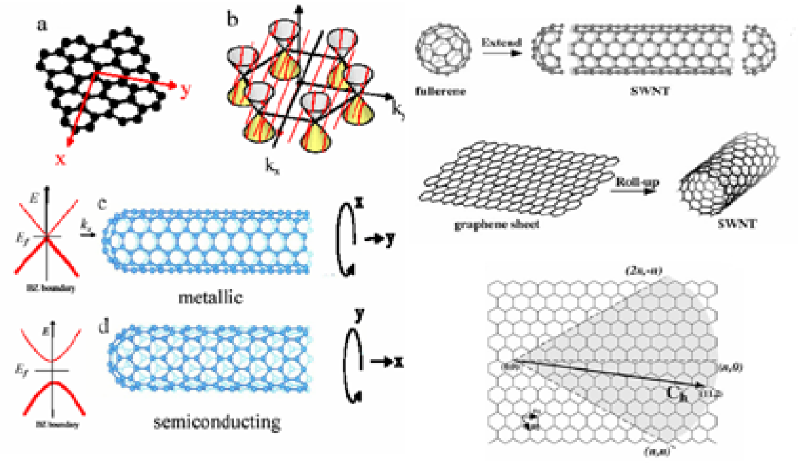

Paul McEuen et.al, IEEE on Nanotech, 1 (2002), 78

T.W.Odem et al J of Phys: Condens Matter 14(2002)

Figure: Band structure of nanotubes and their parent material, graphene. [3]

A nanotube can be described as a sheet of graphene coaxially rolled to create a cylindrical surface.

The 2-D hexagonal lattice of graphene is mapped onto a cylinder of radius R, and the mapping can be realized in different helicities resulting in different nanotubes. If there is a single wall- it is referred to single-wall nanotube (SWNTs), and if it has multiple concentric walls- it is referred to as a multi-wall nanotube (MWNTs). The diameter of SWNT ranges between 0.4 - 3.0 nm. Each nanotube is characterized by a set of integers (n,m) indicating the components of the chiral vector, $C = na_1 + ma_2$, in terms of the Bravais vectors of the graphene lattice, a_1 and a_2. The chiral vector defined as a circumferential vector and the tube is obtained by following the graphene such that the two ends of the vector C are coincident.

Physical Properties of CNTs and parameters on which they depend: Rolling the graphene sheet to form a cylindrical structure results in the quantization of electron's momentum in the circumferential direction, thus reducing the number of available states to planes along the 2-D band structure of graphene. This quantization results in nanotubes being metallic or semiconducting depending on whether or not the planes cut through the corners of the FBZ of the graphene band structure. The tubes are metallic or semiconducting whether or not (n-m) is perfectly divisible by 3. The electronic properties of metallic and semiconducting tubes have been investigated theoretically in rigor.[1a] The important points to note with to regard these properties are

(1) band gap of the semiconducting CNTs is inversely proportional to the diameter of the tube

(2) chirality determines whether the nanotubes are metallic or SC.

The metallic tubes have electronic conductivities and current densities that meet or exceed the best metals, and semiconducting tubes have mobilities and transconductances that meet or exceed the best semiconductors.

References

[1] Iijima S, *Nature* **1991**, *354,* 56

[2] Saito R, Dresselhaus M S and Dresselhaus G *Physical Properties of Carbon Nanotubes* (Imperial College Press: London), **1998**

[3] Fuhrer M, Park H and McEuen PL *IEEE Trans. on Nanotech.* **2002**, *1,* 78

Appendix-IIIb

Raman Spectroscopy of SWNTs

Resonant Raman scattering has been widely employed to characterize SWNTs. This technique has unique advantages for characterizing 1-D nanostructures, and carbon nanotubes in particular, and hence merits a brief introduction. Phonons provide a sensitive probe of the electronic structure through coupling between electrons and phonons in a 1-D nanostructure. When the photon involved in the Raman process is in resonance with an electronic state in the 1- D structure, the coupling gives rise to unusual Raman spectra. Since the electronic states are sensitive to the diameter of the nanotube, the resonance Raman effect is likewise sensitive to the nanotube's diameter. [1]

A typical Raman spectrum obtained from an individual SWNT using λ_{laser}=685 nm showing the radial breathing mode (RBM), the disorder induced band (D-band), and the G band are shown in the figure. The peaks marked by asterisks at 303, 521 and 963 cm^{-1} arise from the underlying Si/SiO_2 substrate. Following is a brief description of the various features observed in a typical Raman spectrum. [1]

Radial Breathing modes (50-100 cm^{-1}): Peaks corresponding to RBM are characteristic signatures of nanotubes with a single wall as well of nanotubes with few walls (the diameter of innermost tube should be less than 2 nm). Radial breathing modes in the Raman spectrum are a characteristic signature of SWNTs and are usually observed in the frequency range of 50-400 cm^{-1}. Importantly, the nanotube diameter is inversely related to this peak position (frequency) and is given by the following relation

$$\text{diameter}_{\text{nanotube}}\ (\text{nm}) = 233\ \text{cm}^{-1}/\omega_{\text{RBM}}\ \ldots.\ (1)$$ [1], 7*

D-band (~1350 cm^{-1}): is a disorder-induced Raman mode and the intensity of this peak correlates to the either to the defect density in the nanotube or the presence of amorphous carbon on the nanotube.

---

[7] The constant in the numerator depends on the type of the substrate.

G-band (1550-1605 cm^{-1}): is related to the in-plane vibrational modes of the graphite structures. This band is an intrinsic feature of nanotubes that is related to vibrations in all sp^2 carbon materials.

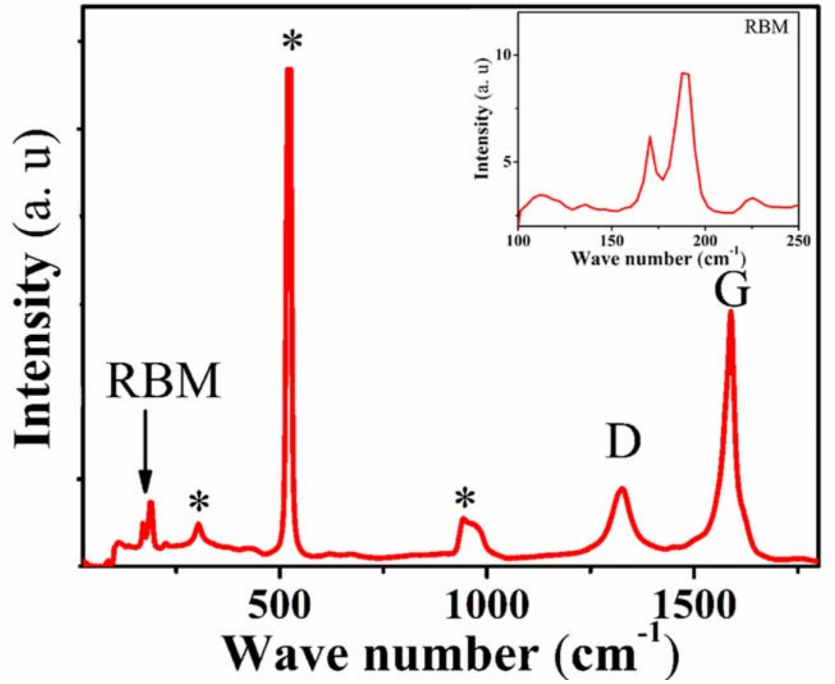

Figure: A typical Raman spectrum of a SWNT on Si/SiO$_2$ substrate. Peaks marked by asterisks arise from Si/SiO$_2$ substrate. [2] Inset shows the radial breathing modes (RBM) peaks. (This data was collected from one of the samples in this study.)

References

[1] M.S.Dresselhaus, G. Dresselhaus, A. Jorio, A.G. Souza Filho, R.Saito, *Carbon* **2002**, *40*, 2043

[2] Temple P A and Hathaway C E *Phys. Rev.***1973***, B 7* 3685

Biographical Note

EDUCATION

MASSACHUSSETTS INSTITUTE OF TECHNOLOGY **2002-2007**

Ph.D., Materials Science and Engineering
Minor in Business Administration at the Sloan School of Management

INDIAN INSTITUTE OF TECHNOLOGY, BOMBAY **1998-2002**

B.Tech, Metallurgical Engineering and Materials Science

TEACHING EXPERIENCE

Solid State Chemistry (3.091)	Spring 2003

AWARDS and HONORS

John F. Elliot Fellowship (MIT)	2002-2003
IIT Bombay Institute Silver Medal	2002
Walchand Hirachand Gold Medal	2002
Manjula Parikh Foundation Trust Prize	2002
IIT Bombay Merit Scholarship	1999-2002
Indian National Mathematics Olympiad	1996
Silver Medalist in State Mathematics Olympiad	1995

PUBLICATIONS

- S. Bhaviripudi, A. Reina, J. Qi, J. Kong and A. M. Belcher *Block-copolymer Assisted Synthesis of Arrays of Metal Nanoparticles and their Catalytic Activities for the Growth of SWNTs*, **Nanotechnology,** 2006 17, 5080-5086.
- S. Bhaviripudi, E. Mile, S. S. Steiner, A. Zare, M. S. Dresselhaus, A. M. Belcher and J. Kong *CVD Synthesis of Single- walled Carbon Nanotubes from Gold Nanoparticle Catalysts,* **J. of Amer. Chem. Soc.** 2007, 129 (6), 1516-1517.
- S. Bhaviripudi, J. Qi, E. L. Hu and A. M. Belcher, *Synthesis, Characterization and Optical Properties of arrays of GaN nanocrystals*, Submitted to **NanoLetters,** 2007.
- S. Bhaviripudi, J. Qi, E. L. Hu and A. M. Belcher, Photoluminescence of InN nanocrystals, In preparation.
- S. Bhaviripudi, J. Qi, G. Zheng, D. S. Yun and A. M. Belcher *Electrochemical Synthesis of Size- and Shape-Controlled Au Nanocrystals as Catalysts for the Growth of 1-D Nanoscale Materials,* Unpublished.

CONFERENCE PRESENTATIONS

- S. Bhaviripudi, A. Reina, J. Qi, J. Kong and A. M. Belcher *Block-Copolymer Templated Synthesis of Patterned Nanoscale Materials*, MRS-Fall 2006 Conference, Boston (November 27-December 1, 2006).
- S. Bhaviripudi, J. Qi, and A. M. Belcher *Synthesis of Large Uniform Arrays of III-oxide and III-Nitride Nanocrystals,* MRS-Fall 2006 Conference, Boston (November 27-December 1, 2006).
- S. Bhaviripudi, J. Qi and A. M. Belcher *Metal Nanocrystals Arrays: Controlled Synthesis and their Physical Properties*, European-MRS Spring 2006 Conference, Nice, France (May 29-June 02, 2006) (accepted).
- S. Bhaviripudi, J. Qi and A. M. Belcher *Size-, Shape- and Position Controlled Synthesis of Metal Nanocrystals as Catalysts for 1-DMaterials*, MRS-Spring 2006 Conference, San Francisco (April 11-17, 2006).
- S. Bhaviripudi, J. Qi and A. M. Belcher *Electrochemical Synthesis of Metal Nanocrystals*, MRS-Spring 2005 conference, San Francisco (March 28-April 1, 2005)

The author invites correspondence to: sreenix@gmail.com